NORTHWESTERN UNIVERSITY

Parallel Processing By Retinal Ganglion Cell Types

A DISSERTATION

SUBMITTED TO THE GRADUATE SCHOOL

IN PARTIAL FULFILLMENT OF THE REQUIREMENTS

for the degree

DOCTOR OF PHILOSOPHY

Field of Neuroscience

By

David Swygart

EVANSTON, ILLINOIS

March 2023

Abstract

The retina detects light, processes the visual signal, and sends a complex set of parallel information channels to the brain via a functionally diverse set of retinal ganglion cells types. This manuscript examines these retinal ganglion cell types, the visual features they encode, and the computational mechanisms leading to their unique feature encoding. Using single-cell electrophysiology, we find that expression of specific genes labels unique sets of functionally identified retinal ganglion cell types. When examining selectivity for the visual feature of object motion across all retinal ganglion cell types, we find a spectrum of selectivity which can be predicted by their degree of nonlinear surround suppression. Finally, using single-cell electrophysiology, serial block-face scanning electron microscopy, pharmacological manipulation, and computational modeling, we show that two retinal ganglion cell types exhibit very different levels of surround suppression even though they receive input from the same set of bipolar cell types. This divergence of the bipolar cell signal occurs through synapse-specific regulation by amacrine cells at the scale of tens of microns. These findings highlight new methods of studying parallel processing in the retina and uncover novel mechanisms of visual processing that enable the high degree of parallel processing observed in the retina.

Acknowledgments

I would like to thank Greg and everyone in the lab for their scientific support. This project had many difficulties and failed experiments. I have never met someone as optimistic and uncrushable as Greg. I would like to thank my wife Sarah for her constant emotional support. Every time I came home in a despairing mood because of a failed experiment, she was there for me. The uncertainties of the PhD have put her through a lot; not knowing when I might finish or where we will live after this. However, she is a shining example of finding contentment regardless of life circumstances. She consistently cares far more about my happiness than her own. I would like to thank my friends and family for not caring much about scientific prestige. It is comforting to know that I could go back to being a small engine mechanic and they wouldn’t think any less of me. Finally, I would like to thank you, the reader. Since there are likely less than five of you, each of you make up a large proportion of the readership of this document.

Abbreviations

RGC	Retinal Ganglion Cell
BC	Bipolar Cell
AC	Amacrine Cell
SMS	Spots of Multiple Sizes
UV	Ultraviolet
AAV	Adeno-Associated Virus
OMS	Object Motion Sensitivity
RF	Receptive Field
TTX	Tetrodotoxin
TH	Tyrosine Hydroxylase
VGAT	Vesicular GABA Transporter
VGluT3	Type 3 Vesicular Glutamate Transporter
DS	Direction-Selective
DSI	Direction Selectivity Index
OMSI	Object Motion Sensitivity Index
SI	Suppression Index
IPL	Inner Plexiform Layer

GCL	Ganglion Cell Layer
ChAT	Choline Acetyltransferase
Kyn	Kynurenic Acid
CSR	Center-To-Surround Ratio
σ_s	Receptive Field Surround Size
s.e.m.	Standard Error of the Mean
SBFSEM	Serial Block-Face Scanning Electron Microscopy
INL	Inner Nuclear Layer

Table of Contents

Table List

Figure List

	depend on glutamate receptor saturation or desensitization.
Fig. 4.4	Pix_{ON} and ON alpha RGCs receive excitatory input from the same bipolar cells.
Fig. 4.5	Wide-field amacrine cell regulation at the bipolar cell terminal contributes to stronger surround suppression in Pix_{ON} RGCs.
Fig. 4.6	Cable model of the bipolar cell terminal.
Fig. 4.7	Modeling suppression of RGC excitation through electrical isolation of inhibition on the bipolar axonal arbor.
Supplementary Fig. 4.1	Pix_{ON} and ON alpha RGCs exhibit unique morphology and correspond to M5 and M4 RGCs.
Supplementary Fig. 4.2	Pix_{ON} and ON alpha RGCs have differing levels of surround suppression in both scotopic and photopic conditions.
Supplementary Fig. 4.3	Pix_{ON} RGCs have stronger surround suppression than ON alpha RGCs across retinal locations.
Supplementary Fig. 4.4	Verification of voltage-clamp isolation of excitatory and inhibitory currents in a Pix_{ON} RGC.
Supplementary Fig. 4.5	Pix_{ON} and ON alpha RGCs exhibit similar contrast response functions in their excitatory conductances.
Supplementary Fig. 4.6	A bipolar subunit model of RGC excitation suggests differing bipolar receptive fields are necessary to evoke the differing level of surround suppression observed.
Supplementary Fig. 4.7	PSD95 puncta apposed to type 6 bipolar cell terminals throughout the

	dendritic arbors of Pix_{ON} and ON alpha RGCs.
Supplementary Fig. 4.8	ON alpha surround suppression of excitation remains weak in pharmacological block of $GABA_C$ receptors and Na_V channels.
Supplementary Fig. 4.9	Cable model consistency over a range of parameter values.
Supplementary Fig. 4.10	Fitting length constants to inhibitory synapses.

Chapter 1: Introduction

Parallel processing in the retina through many cell types

The retina is far more than the brain's camera. Although less than 200 um thick and consisting of only three layers of cells, the retina performs complex processing of the visual signal and conveys many parallel streams of visual information to the brain. Splitting the visual signal into many parallel channels of processed visual information allows for the efficient transfer of salient visual features to the brain while also reducing the number of computations required during downstream visual processing.

These parallel channels of information are encoded by unique neuronal cell types, with each cell type encoding a different set of visual features. In the first layer of the mouse retina, 3 different cell types (photoreceptors) detect light. These photoreceptor types differ in their encoding of color sensitivity, luminance sensitivity, and kinetics. The photoreceptors then pass these visual signals to the next layer of the retina, stimulating 15 bipolar cell types[11,12]. These bipolar cell types encode the visual world with even greater heterogeneity and specificity, selective for increments vs. decrements of light, color-opponent response, and an even broader range of kinetics. The bipolar cells then pass these visual signals to the final layer of the retina, which contains >40 different retinal ganglion cell types[13–15]. The ganglion cells encode a wide variety of visual features, including complex spatial profiles, objection motion sensitivity, direction selectivity, orientation selectivity, and much more. In this manuscript, I will examine these output neurons of the retina, the computations leading to their parallel channels of information, and how they distribute the encoding of visual features.

Identifying retinal ganglion cell types

To understand how parallel processing occurs in the retina, one must first identify the cell types that carry these parallel channels of visual information. Although the important distinction between retinal ganglion cell types is the functionally distinct signals they send to the brain, genetic expression patterns and morphology can also be used to identify RGC types. Indeed, their unique gene expression patterns and morphology often underlie the mechanisms that generate their unique functional signals[1,2]. Recent

advances in sequencing techniques, particularly in single-cell RNAseq, have made transcriptomics more feasible[3,4]. Finding a specific gene that is expressed by one type of retinal ganglion cell (RGC) opens up that type for further study[2,5,6]. By genetically labeling cells, circuit dissection, cellular manipulations, and axon tracing are all more readily accessible. However, it is rare to find a gene that labels a single type (Chapter 2,[7,8]). Large-scale transcriptomics studies can classify the transcriptomes into different clusters, but then the identity of those clusters with respect to light responses is unknown[1,3,9]. Recently, Goetz et. al.[10] have aligned light response data with morphology[11] and transcriptomics data[2]. As a result, we can begin to relate the expression profiles of different RGCs with their light responses and better understand how the diversity of RGC responses is achieved. In Chapter 2, I will explore how we can functionally type RGCs that are labeled with specific molecular markers. This chapter contains pieces of published work from two publications to which I significantly contributed[7,8].

Visual feature encoding across cell types

Although retinal physiologists often desire to assign a single distinct visual feature to each retinal ganglion cell type, feature encoding is often far more complex. A cell type is considered feature selective if it spikes strongly to a stimulus of interest. For instance, orientation-selective cells will fire for either horizontal or vertical bars[12,13], or direction-selective cells spike for one particular direction of motion[14,15]. However, each of these “feature selective” cell types respond to many other stimuli, and many other cell types will respond to these same visual features with varying degrees of specificity. Ultimately, how we define visual features is somewhat arbitrary, with good definitions depending on how visual features are actually used downstream for real behavior. In Chapter 3, I review the visual feature of object motion for which many publications have identified cell types selective for this feature. I then show unpublished work examining selectivity for this feature across a broad range of retinal ganglion cell types.

Mechanisms of signal divergence

To achieve this ever-increasing number of parallel streams of visual information, the visual signal must diverge. The neuronal computations underlying this signal divergence occur through different mechanisms at multiple locations in the retina. In Chapter 3, I examine two retinal ganglion cells which

share similar network connectivity but exhibit differing functional signals. I examine the sources of the signal divergence that leads to these parallel streams of visual information. This chapter contains work under review for publication and is available in preprint form[16].

Chapter 2: Functionally Typing Molecularly Identified RGCs

Introduction

Each of the ~40 mouse RGC types encodes a unique channel of visual information. These distinct functional signals motivate their existence. However, unique gene expression patterns and morphology often underlie the mechanisms that generate their unique functional signals and allow further properties by which one can classify RGC types[1,2]. While identification and classification of RGC subtypes is an important first step to understanding the function of the retina, much more work is required to understand the circuitry and computational mechanisms that give rise to each RGC subtype's unique encoding of the visual world. Mouse lines that show subtype-specific labeling can greatly aid in studying the function of these RGC types and enable to use of a myriad of genetic tools.

In these works, we examined two such mouse lines that label cells that express the genes for Brn3c and Opn5. If a single RGC type was labeled by expression of either protein, it could allow further study of that type. In addition, it would implicate that type with a specific role in retinal development in the case of Brn3c and in response to ultraviolet light in the case of Opn5. Furthermore, typing RGCs in these two transgenic lines allows for the examination of their downstream projection patterns.

The first mouse line that we examined was one that labeled cells expressing the transcription factor Brn3c. Transcription factors regulate a wide variety of gene expressions and contribute to the cell's development and differentiation. Labeling this transcription factor allows us to track how the RGCs develop and potentially give clues to their function[17]. Brn3c is a subset of the Brn3 transcription factor family that all have POU domains. POU domains are a family of proteins containing homeodomains of DNA binding sites. The Brn3 family consists of three transcription factors: Brn3a, Brn3b, and Brn3c. Over or under-expression of any of these proteins can have large changes in the retinal ganglion cell population[18] in mice and chicks. Here, we focus on Brn3c. Understanding the types of RGCs that express Brn3c would provide insight into retinal development. If one cell type were labeled, there we would be able to trace that cell through development, and that cell type might then have a specific function in the

adult mouse. Here, we functionally type RGCs expressing Brn3c using light stimuli to measure receptive field size and other stimuli to determine which RGC types express Brn3c. We find that multiple cell types are labeled and that Brn3c-expressing RGCs are localized to the central region of the retina.

The second mouse line that we examined labeled cells that expressed the Opn5 gene. Opsin (Opn) proteins are responsible for the transduction of light to an electrical signal[19]. The classical opsin, rhodopsin (Opn2), is expressed in rods and has been extensively studied over the last 50 years. The opsin protein family consists of 5 main subtypes, Opn1 through Opn5. Opn1 and Opn2 are expressed in rods and cones and are responsible for the classical image-forming vision. Opn4 is known as melanopsin and is expressed in intrinsically photosensitive RGCs, contributing strongly to non-image-forming vision[20]. The role of Opn5 in the retina is still unknown. Opn5 has spectral absorption in the ultraviolet (UV) wavelength of 380 nm when reconstituted with 11-cis-retinal[21]. Here, we aim to identify the subsets of RGCs that express Opn5 under two different gene expression systems. If there were one cell type labeled, that type might have a unique role in mouse vision and, in particular, response to UV light. By identifying the types of RGCs involved and understanding their receptive field structure, we can then investigate how Opn5 might contribute to responses to UV light in the mouse.

Results

A wide distribution of cell types is labeled in the Brn3c-Cre line.

To identify the RGC types labeled in the Brn3c-Cre line, we performed functional typology using a wide variety of light stimuli (**Fig. 2.1A**, black). We found that at least 27 cell types are labeled in this Brn3c-Cre mouse line. This reporter line expresses Cre development, leading to fluorescently labeled cells even if they no longer express Brn3c at the time of recording. To assess if a more specific subset of cells expresses Brn3c in the adult animal, we injected a floxed-AAV (Adeno-Associated Virus) into the eyes of Brn3c-Cre mice. Using this AAV method, we found a similar subset of RGC types to be labeled as was observed in the mouse reporter line (**Fig. 2.1A**, green). Although a wide range of cell types were labeled through either method, some cell types were much more common (ON OS, OFF OS, ON-OFF DS, ON transient MeRF). However, it should be noted that these cell types tile the retina more densely than other

RGC types. After normalizing our raw cell counts by the density of each cell type, many of these effects disappeared ([11]; **Fig. 2.1A**, bottom plot). Thus, we find that a large distribution of RGC types is labeled in the Brn3c-Cre line, with no specific subset expressing the Brn3c transcription factor in either development or adulthood.

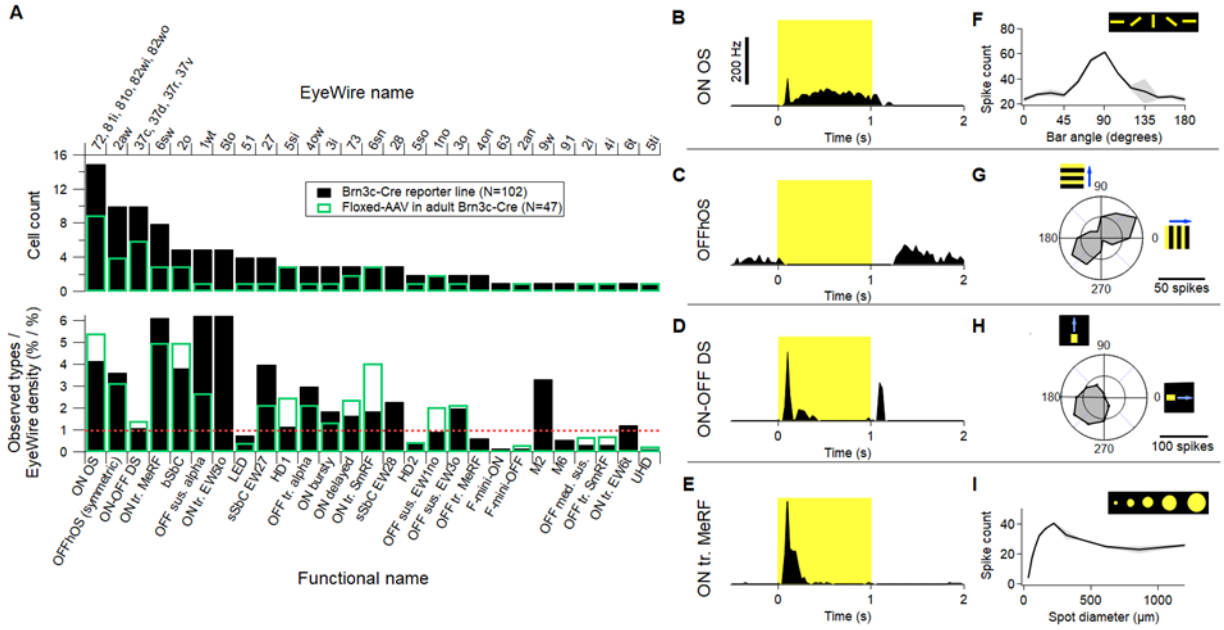

Fig. 2.1 | A broad set of RGC types are labeled with Brn3c.

(**A**) Histogram of cell counts labeled in the Brn3c line (black) and in AAV-injected mice (green). The upper histogram shows the raw cell counts, while the lower histogram normalizes the cell counts by type density in Eyewire. (**B-F**) Examples of types identified: ON OS (**B**), with its accompanying flashed bar response (**F**); OFFhOS (**C**), with its drifting gratings response (**G**); ON-OFF DS (**D**), with its moving bar response (**H**); and ON tr. MeRF (**E**) with its spots multiple size response (**I**).

Small receptive field, ON-OFF cells are primarily labeled by Opn5.

We sought to more comprehensively assess *Opn5*-RGC types and their visual response properties through electrophysiological profiling and mapping responses to known functional types[2,7]. To this end, we virally labeled *Opn5*-RGCs in *Opn5cre*; *Ai9* mice (using either AAV2-Flex-eGFP or AAV9-BbTagBY) and recorded from Ai9+ eGFP+ (active cre-expressing) or Ai9+ eGFP- (lineage) cells (**Fig. 2.2A**). In

cell-attached recording mode, we recorded spike trains in response to spots of varying sizes, moving bars, etc. (see **Methods**), and based on cellular responses, we assigned these cells to known functional RGC types (**Fig. 2.2B**). Recordings and assignments from both virally traced and lineage cells were largely consistent, with F-mini-ON[22] and HD2[23] being overrepresented in each group. Additionally, of the RGC types that represent >5% frequency (average of Ai9+ GFP+ and Ai9+ GFP- groups), we find that four of five types are ON-OFF RGCs that respond optimally to edges, small spots, and motion (F-mini-ON, HD2, HD1, Local Edge Detector/LED, and ON-OFF DSRGC). As edge or spot detector RGC types (F-mini-ON, HD2) are found at high densities in the retina, an apparent enrichment of these cells could be an artificial inflation[24,25]. To rule out this possibility, we compared the frequency of each RGC type in our recording dataset to their frequencies in the Eyewire museum (**Fig. 2.2C**)[11]. Consistent with the notion that F-mini-ON and HD2 RGCs were enriched in our electrophysiological survey of *Opn5*-RGCs, we found these RGC types at rates well above their expected frequencies (**Fig. 2.2C**).

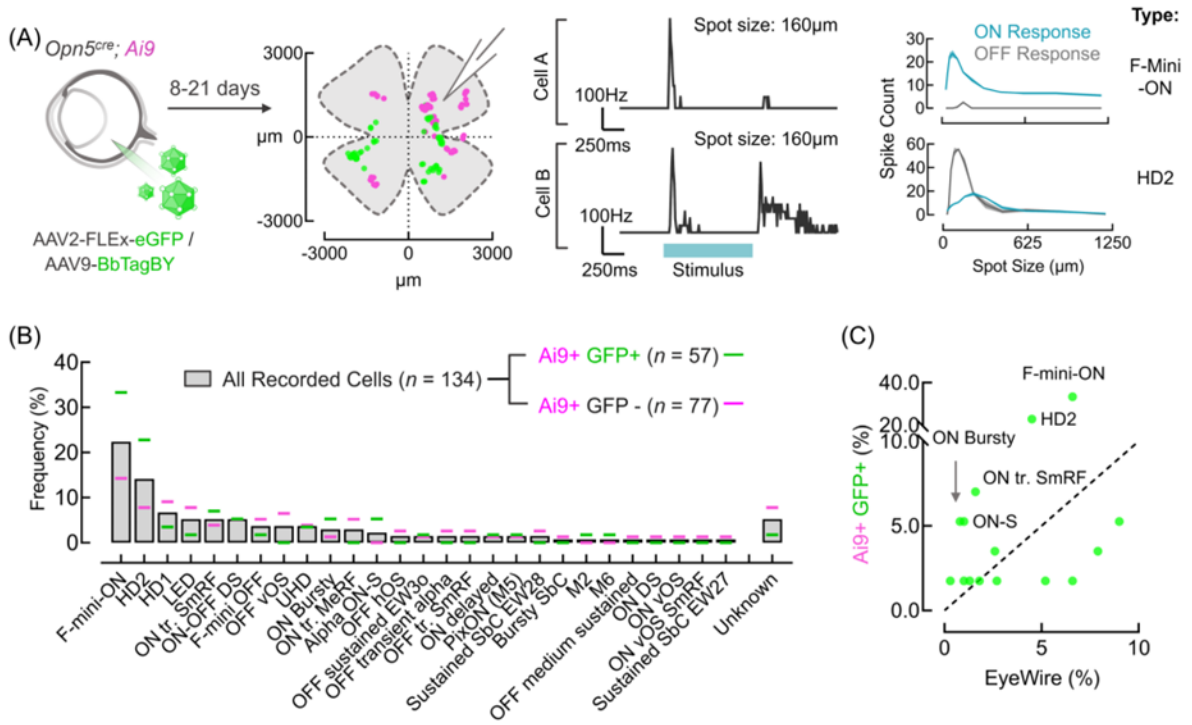

Fig. 2.2 | Primarily small receptive field, ON-OFF RGCs express Opn5.

(**A**) Typological assessment of Opn5-RGCs using natively labeled (magenta) or virally labeled (green) cells following intravitreal injection of AAV2-FLEX-eGFP or AAV9-BbTagBY, with spatial locations of each recorded cell. (A, Right) Examples firing rates from two cells in whole-cell mode when exposed to a 160 µm spot of light over their receptive fields and spatial tuning curves to spots of varying sizes. (**B**) Typological classification of RGC types encountered in the *Opn5cre* that were virally labeled (Ai9+ GFP+ or green, n = 57 cells) or natively fluorescent (Ai9+ GFP- or magenta, n = 77). RGC types were normalized as a proportion of each fluorescent category (virally labeled or native). (**C**) Correlation of RGC type frequency (%) of virally labeled cells compared to expected frequencies based on the Eyewire dataset[11](****p < 0.0001; One-way ANOVA with Tukey's post-hoc analysis). Scale bar = 25 µm (F)

Discussion

Here, I have presented work where we looked at the functional RGC types that express two different proteins. While we were not able to identify single cell lines, labeling subpopulations still provided more insight into how multiple RGC types may develop or function. And perhaps, these RGC populations act in concert to encode information downstream, and we do not yet have the tools to examine their population dynamics. Understanding RGC typology allows us to contextualize the information encoding of the retina and how that information is processed downstream in the brain.

Brn3c is a transcription factor that contributes to retinal development[7,17]. In this work, the authors developed a Brn3c^{CKOCre} conditional allele to study the expression of Brn3c in both developing and adult mice[7]. This specific genetic strategy revealed that only RGCs were labeled by the Brn3 transcription factor family and that Brn3c-positive cells were also labeled Brn3a^{+} or Brn3a^{+}Brn3b^{+}. Thus, very few RGCs were solely Brn3c positive. The population of Brn3c-positive cells was heterogeneous, with both monostratified and bistratified cells, suggesting that multiple types were labeled. Whole retina staining revealed that the central area of the retina was more densely labeled. Therefore, the cell types that we typed above (**Fig. 2.1**) likely were cells in the center of the retina as opposed to those on the periphery.

Given that each RGC type is thought to form a mosaic that tiles the entire retina in the mouse[26], it provides further evidence that the cells labeled by Brn3c have some other role in the development or function of the visual system as opposed to contributing to the development of a single type. The authors then investigated the projection patterns of these Brn3c-positive RGCs. These RGCs project to many different brain regions. In addition, there are several midbrain structures that have Brn3c-positive nuclei labeled as well. Therefore, Brn3c doesn't seem to have a role in the development of specific RGC types but rather plays a role in setting up RGC projections and other circuits involved in sensory processing as well.

Opn5 encodes a UV-sensitive opsin protein. The role and function of this opsin are not yet known. The authors found that only RGCs were labeled in the Opn5^{Cre} retinas[8]. The labeling in whole-mount retinas was enriched in the dorsal-temporal quadrant, where other RGCs are known to be enriched[27]. To investigate the potential role of Opn5-positive RGCs, the authors then studied the projection patterns into the brain. They found projections to image forming and image stabilization regions such as the lateral geniculate nucleus and the accessory optic system. To begin to understand if Opn5 RGCs represented a single type, they performed analyses to determine if Opn5-positive cells formed a mosaic in the retina. However, the analyses suggested that multiple cell types were labeled. This aligned with my work showing that multiple functional types of RGCs were present in Opn5-positive cells (**Fig. 2.2**). They then examined RGC single-cell RNAseq data and found that two distinct clusters contained more than one cell with Opn5 expression. While expression was limited to F-mini ON, HD1, and HD2 RGCs, attempts to record an intrinsic photocurrent failed to identify an intrinsic photocurrent (data not shown). Therefore Opn5 is expressed in multiple RGC types, and the role of Opn5 in visual processing is still unknown.

Methods

Ex vivo retina preparation

Mice of either sex aged 6 - 36 weeks were used for recordings and imaging. Brn3c: Brn3c-Cre were crossed with Ai14 mice. Thus all cells that express Brn3c are labeled with tdTomato fluorescence under 2-Photon imaging.

Opn5: Opn5-Cre mice were crossed with Ai9 mice. We then injected them with either an AAV9 BbTagBY under an eF1a promoter or an AAV2 Flex-eGFP under a CAG promoter. Cells that expressed Opn5 at any time point during development were labeled with TdTomato from the Ai9 reporter, and cells that expressed Opn5 in the adult animal were labeled with the virus.

Whole mount retinas were prepared in a similar manner to previous publications[12,13,23,28–31]. In short, dark-adapted mice were sacrificed, and retinas were dissected under infrared illumination (940 nm). The intact retina was flat-mounted photoreceptor side down on a poly-D-lysine-coated glass coverslip and placed in a recording chamber. Retinas were perfused with oxygenated Ames medium at 32°C at a rate of 10 mL/min throughout the experiment. Animals were sacrificed following animal protocols approved by the Center for Comparative Medicine at Northwestern University.

Visual stimulation

Visual stimuli were generated with a 912 x 1140 pixel DLP projector (1.3 μm/pixel) at a 60 Hz frame rate using a blue LED (450 nm) focused on the photoreceptor outer segments. Light intensities are reported in rhodopsin isomerizations per rod per second (R*/rod/s). Visual stimuli had intensity values of 200-300 R*/rod/s and background intensity values of ~0.3 R*/rod/s unless otherwise noted. Each cell's receptive field center was determined by flashing horizontal and vertical bars at different locations, and all subsequent stimuli were centered on the location that elicited maximal responses. Receptive field size and surround suppression was probed using a pseudorandom sequence of 12 spot sizes (diameters logarithmically spaced from 30-1200 μm) each presented for 1 second.

Flash responses and spots of multiple sizes responses were compared to population data on rgctypes.org to confirm typology. Contrast responses to 200 and 2000 μm spots at a mean level of 1000 R*/rod/s were used to identify suppressed by contrast RGCs. Moving bars sized 200 x 600 μm were presented in 12 different directions of movement to identify direction-selective RGCs. Bars sized 50 x 800 μm flashed at 12 different orientations were used to identify ON Orientation Selective RGCs[12]. Drifting gratings with a

mean luminance of 1000 R*/rod/s were shown at 12 different directions to identify OFF Orientation Selective RGCs[13].

Cell-attached and whole-cell recordings.

Fluorescently labeled RGCs were targeted via two-photon microscopy. All recordings were obtained using a 2-channel patch-clamp amplifier (Multiclamp 700B, Molecular Devices) sampling at 10 kHz. Spike trains were recorded using glass pipettes (2–3MΩ) filled with AMES solution in cell-attached configuration. Voltage-clamp recordings were performed using glass pipettes (4–6MΩ) filled with a cesium-based intracellular solution (105 mM Cs methanesulfonate, 10 mM TEA-Cl, 20 mM HEPES, 10 mM EGTA, 2 mM QX-314, 5 mM Mg-ATP, and 0.5 mM Tris-GTP; ~277 mOsm; pH ~7.32 with CsOH). Voltage was corrected for the liquid junction potential (−8.6 mV) and the cell was clamped to the reversal potential of chloride (−60 mV) to measure excitatory conductances or the reversal potential of glutamate-induced cation currents (+20 mV) to measure inhibitory conductances. Current clamp recordings and cell fills of neurobiotin were performed using glass pipettes (4–6MΩ) filled with a potassium-based intracellular solution (125 mM K-aspartate, 10 mM KCl, 1 mM MgCl2, 10 mM HEPES, 1 mM CaCl2, 2 mM EGTA, 4 mM Mg-ATP and 0.5 mM Tris-GTP; 77 mOsm; pH ~7.15 with KOH).

Viral labeling

Cre-expressing RGCs were labeled by intravitreal injection of Cre-dependent AAV2 which induced expression of eGFP. As this was performed in Ai14 mice which exhibit Cre-dependent expression of TdTomato, all eGFP RGCs were also found to coexpress TdTomato.

Chapter 3: Object Motion Sensitivity across retinal ganglion cell types

Introduction

Motion is ubiquitous in vision, but there is a fundamental dichotomy in its source with important behavioral implications. Some motion on the retina is caused by self-motion of the eyes, head, or body, and other motion on the retina represents the actual movement of objects in the visual scene. Distinguishing between self and object motion is required for visually guided navigation through the world, recognizing the movements of predators and prey, and segmentation of objects.

The brain has its own set of circuits for distinguishing self-motion from object motion across all sensory modalities. These circuits route copies of self-generated efferent commands from the motor system to sensory systems to be incorporated into ongoing predictions of sensory input. The visual system certainly contains efferent copies of motor commands, most studied in the context of saccades[32], but these postretinal computations are beyond the scope of this book. Instead, this chapter focuses on a retinal computation that may play a role in disambiguating self-motion from object motion.

Retinal circuits do not have direct access to the motor commands that drive eye, head, or body movements. The fixational drift eye movements that jitter the retinal image between saccades are independent in the two eyes and are unlikely to be represented in the efferent system. Therefore, the retina must rely on a simpler (albeit imperfect) visual proxy for self-motion vs. object motion: global vs. local motion. Self-generated movements create global motion across the retina, whereas objects move differently from their surroundings. Importantly, the background need not be static in the case of object motion. If, for example, your eyes are panning horizontally, causing a global leftward motion on the retina, and an animal suddenly runs in the opposite direction, causing a rightward motion on the retina, this “differential” motion should be recognized as that of an object. Recognizing global versus object motion may also be important in contexts beyond self motion. For example, one can more easily spot a fish swimming opposite the direction of a stream than a fish swimming with the current. Such motion pop-out effects are well documented in human psychophysics [33].

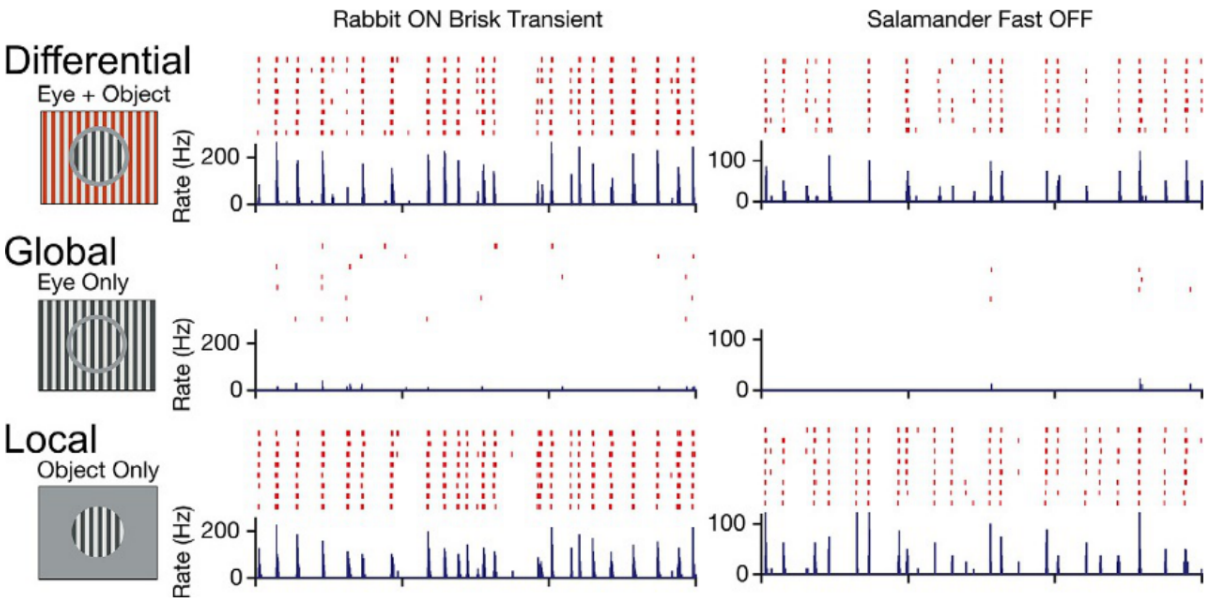

Fig. 3.1 | OMS retinal ganglion cells.

Responses of example RGCs from rabbit and salamander to differential, global, and local motion[34].

Discovery of object motion sensitivity in the retina

Olveczky et al.[34] first described object motion sensitivity (OMS) as a retinal computation. They studied how retinal ganglion cells (RGCs) in salamander and rabbit responded to the motion of grating stimuli in the context of simulated fixational eye movements (**Fig. 3.1**). In their “eye only” (global motion) condition, both a central spot and the surrounding regions moved in the same random walk, simulating global motion due to fixational eye movements. In their “eye + object” (differential motion) condition, the center and surround again moved in a random walk but differed in their random seed. Hence, the motion followed a different pattern in the two regions. This stimulus was meant to simulate the movement of a central object and the ongoing motion of the surround due to fixational eye movements. Subsets of RGCs in both species responded robustly in the eye + object condition and were almost silent in the eye-only condition. Also, cells under the object responded synchronously, a property likely to facilitate the segmentation of object from background. The authors labeled these RGCs as OMS cells.

Circuit mechanism

Olveczky et al.[34] proposed a model for the OMS circuit that was elaborated and tested in a subsequent paper by the same group[35]. The model has two core components: nonlinear subunits in the receptive field (RF) center and rapid inhibition from a population of nonlinear amacrine cells (ACs) in the ganglion cell RF surround (**Fig. 3.2**).

The RF center of OMS RGCs is provided by bipolar cells (BCs) with strong rectification at their output. As discussed in Chapter 7, this results in nonlinear spatial subunits. In the context of motion, the nonlinear subunits make the OMS RGC invariant to the phase or precise pattern of motion. For example, any movement of the many dark bars within the RF center of a fast OFF OMS RGC in salamander will activate some of the BC subunits with their much smaller and overlapping RFs. Consequently, shifting the starting phase of the grating or the direction or other statistics of the motion has little effect on the summed response at the level of the RF center of the RGC. For OMS RGCs to respond to rapid motion, as is the case at least in salamander, the BC inputs in their RF center must also respond at high temporal frequencies[35].

Nonlinear subunits (also presumably BCs) provide input to wide-field amacrine cells (ACs) whose influence covers a vast region of visual space. To affect such wide-field inhibition, ACs must either have a large RF or, in the case of polyaxonal amacrine cells, a small RF coincident with their dendritic arbor and a large output region, or projective field, covered by long axons. For ACs with a large RF, the RF is not necessarily defined by the dendritic extent of individual ACs because strong electrical coupling can spread activation laterally within the population, similar to the coupling among horizontal cells in the outer retina (**Fig. 3.2,** see **Chapter 8**). Widefield ACs provide fast and temporally precise inhibition to the RF center circuit, either onto the BC terminals, the OMS RGC dendrites, or both.

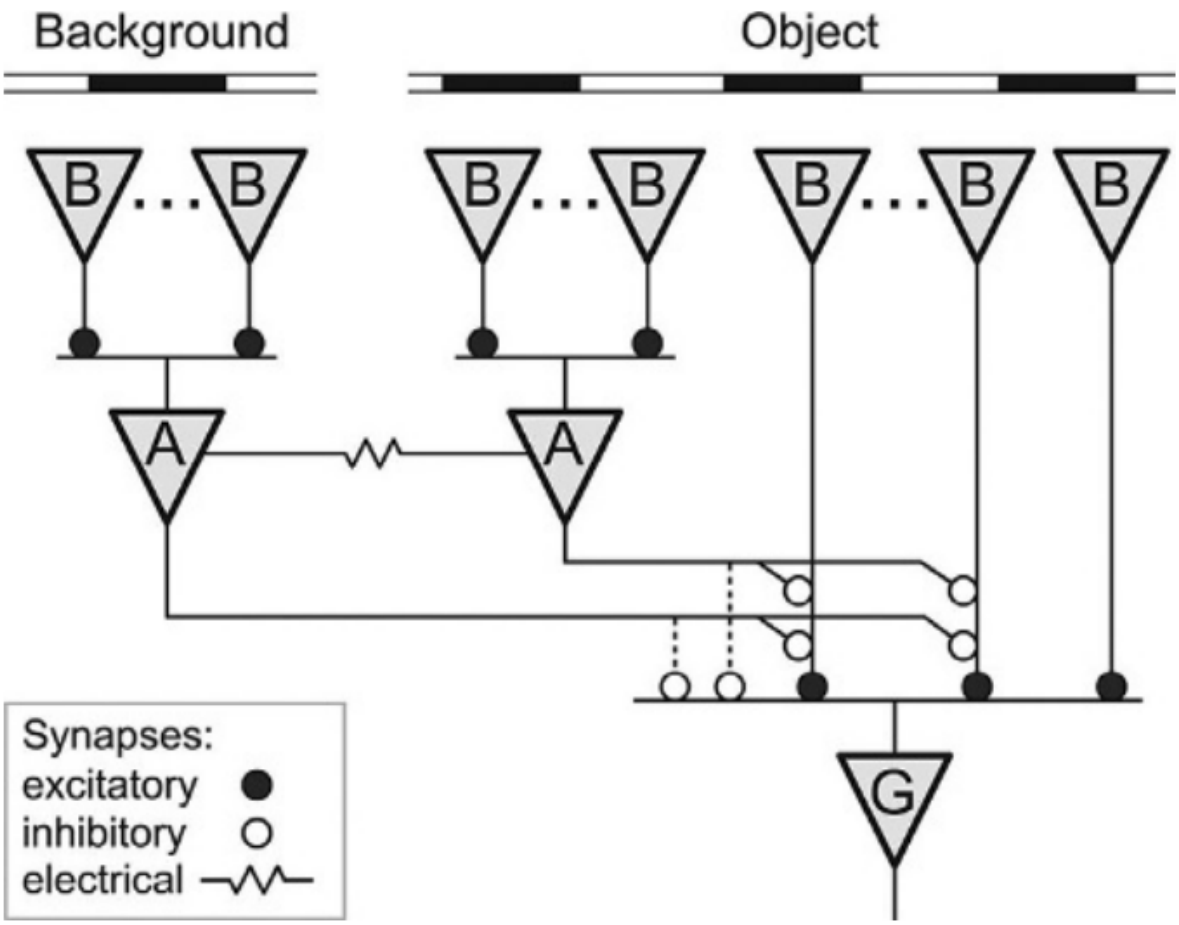

Fig. 3.2 | Circuit model for OMS.

Schematic of a circuit motif that can account for OMS. All BC synapses are rectified, leading to nonlinear spatial integration in the RF center and surround. Wide-field ACs provide inhibition presynaptically onto BCs, postsynaptically onto RGCs, or both. (From Baccus et al.[35])

Baccus et al. (2008) tested this model by recording responses of various retinal interneurons to global and differential motion (**Fig. 3.3**). Several aspects of their data were consistent with the model. First, while somatic voltage responses of BCs were well described by a linear spatiotemporal filter, the postsynaptic responses in OMS RGCs showed nonlinear spatial integration, suggesting rectification at the BC output synapse. Second, they identified a class of polyaxonal ACs with long axons and the appropriate response properties: invariance to grating phase and rapid and temporally precise depolarization that were

coincident with those of OMS RGCs. Finally, they performed technically challenging experiments in which they injected current into the polyaxonal ACs while simultaneously recording OMS RGCs on a multi-electrode array. These experiments demonstrated functional connectivity between the ACs and the RGCs, though the location of inhibitory synapses (onto BC terminals versus RGC dendrites) could not be definitively identified.

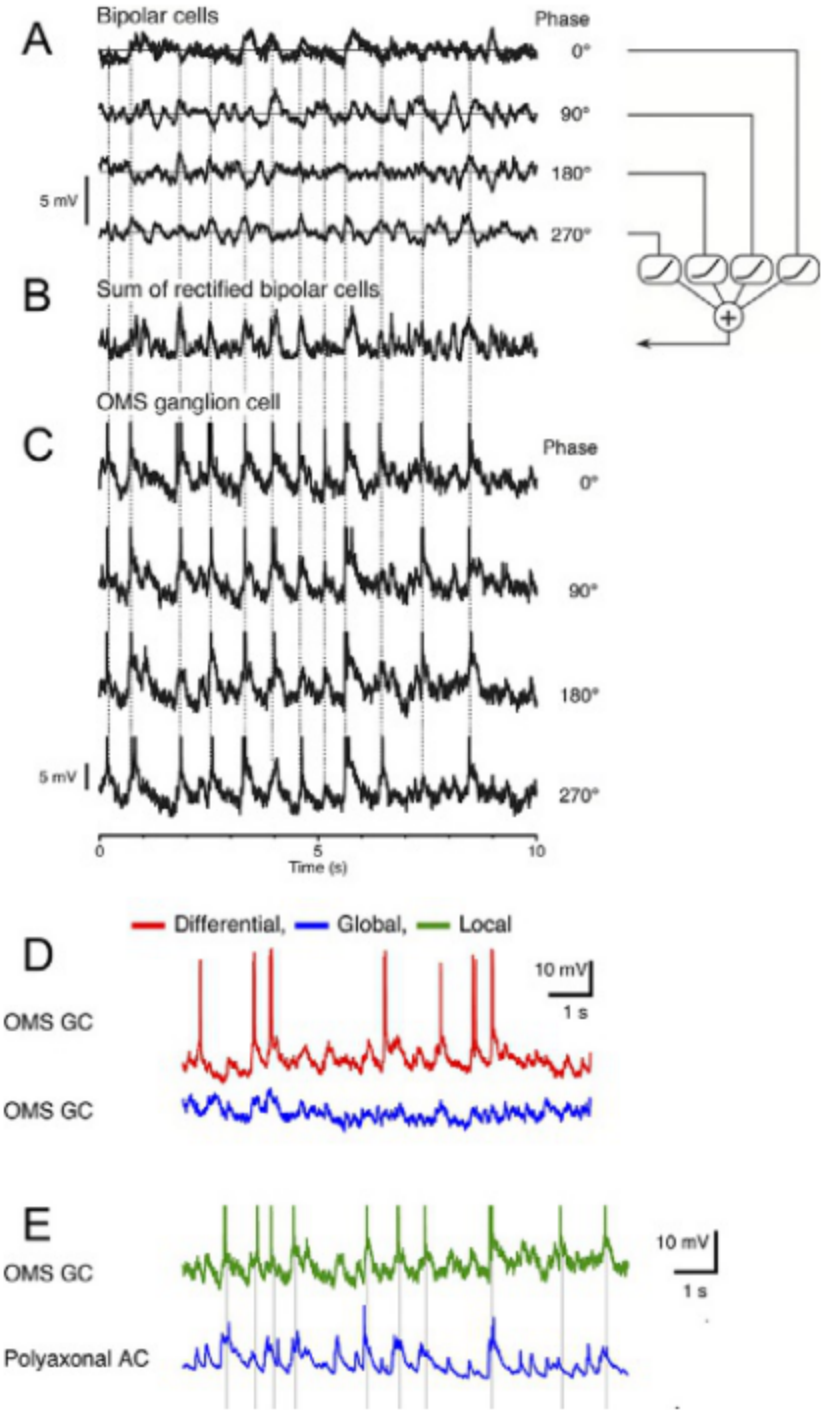

Fig. 3.3 | Responses of retinal neurons to different types of motion stimuli.

(**A**) Intracellular recordings of BCs show dependence on the spatial phase of the motion stimulus. (**B**) Sum of the traces in **A** after rectification to retain only depolarizations. (**C**) Intracellular responses of an

OMS RGC to the same four stimuli at different phases (spikes truncated). The RGC's response is independent of stimulus phase. (**D**) Intracellular recording of an OMS RGC to the same RF center motion pattern in differential (red) or global (blue) mode. (**E**) Intracellular recording of an OMS RGC to a local motion stimulus (green) and a polyaxonal AC to the same stimulus pattern in global mode (blue). (Modified from Baccus et al.[35])

Identifying specific components of OMS circuits in mouse retina

The W3 mouse line labels an OMS retinal ganglion cell

More recent work on OMS circuits has largely been performed in the mouse, where knowledge of cell types and genetic tools have made detailed circuit-dissection experiments possible. Zhang et al.[36] described an OMS RGC type that was fluorescently labeled in the W3 mouse line. Although the W3 line labeled multiple retinal ganglion cell types, the authors recorded from the brightest cells and described them as a single cell type called W3b ("bright"). Similar to the OMS mechanism described in salamander, the W3b RGC pooled ON and OFF rectified excitation from the center of its RF while receiving strong pre- and postsynaptic nonlinear surround suppression. This strong nonlinear surround suppression caused the cell to stay silent for wide-field visual stimuli but respond robustly to local contrast-reversing gratings and motion of small objects (**Fig. 3.4**). Notably, the authors compared local motion with global motion in this study, but they did not explicitly test the differential motion stimuli used in previous reports of OMS RGCs. Subsequent work on the OMS mechanism mouse has focused on the cells identified as "W3" or "W3b" and local vs. global motion. We will return to consider whether these RGCs represent a single type and the generality of the results for differential motion.

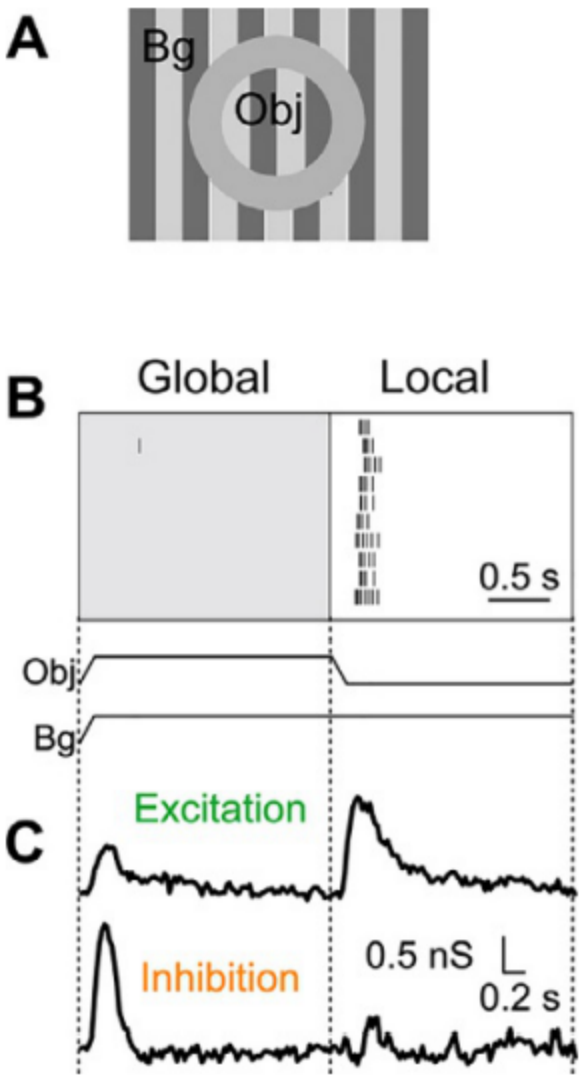

Fig. 3.4 | Global and local motion responses of W3b RGCs in mouse retina.

(**A**) Spatial configuration dividing the stimulus into center (Obj) and surround (Bg) regions. (**B**) Spike raster of an RGC across the global and local motion phases of the stimulus. (**C**) Excitatory and inhibitory conductances for the cell in **B**. (Modified from Zhang et al.[36])

TH-2 ACs provide inhibition to some OMS RGCs

Pharmacology experiments by Zhang et al.[36] showed that the ACs providing both presynaptic and postsynaptic inhibition in the W3b circuit were spiking since their effects were largely eliminated by the

voltage-gated sodium channel antagonist, tetrodotoxin (TTX). Kim and Kerschensteiner[37] used a different mouse line (TH-Cre) in which a subset of ACs was labeled to study OMS circuits. This line inserted Cre into the promoter for tyrosine hydroxylase (TH), a necessary enzyme for dopamine production. While dopaminergic ACs were labeled in this line[38], Kim and Kerschensteiner[37] reported that another AC, called TH-2, which is actually TH-negative, provided direct inhibition to OMS RGCs. Importantly, TH-2 ACs are nonspiking, and the authors reported no significant changes in their light responses with TTX. They also identified RGCs as OMS (called “W3” in their paper) by morphology and light responses, but they did not use the W3 line. Thus, it is possible that largely nonoverlapping populations of OMS RGCs were investigated in these two studies with potentially different upstream circuit elements.

Nonetheless, Kim and Kerschensteine[37] demonstrated direct connectivity between TH-2 ACs and OMS RGCs using optogenetics. They also showed that knocking out the vesicular gamma-aminobutyric acid (GABA) transporter, VGAT, specifically in Cre-expressing cells in this line, largely eliminated OMS in the recorded RGCs (**Fig. 3.5**). The efficacy of TH-2 ACs in this circuit for suppressing responses to global motion depended more on response timing than it did on amplitude. Although the amplitude of the response for the two forms of motion was similar in the TH-2 AC, global motion elicited much faster responses than local motion. This timing difference was essential to the computation because, while the fast inhibition from global motion was well aligned to cancel excitation, the slow inhibition from local motion was not. Thus, rapid GABA release from TH-2 ACs onto at least a subpopulation of OMS RGCs represents an important component of some OMS circuits in the mouse retina.

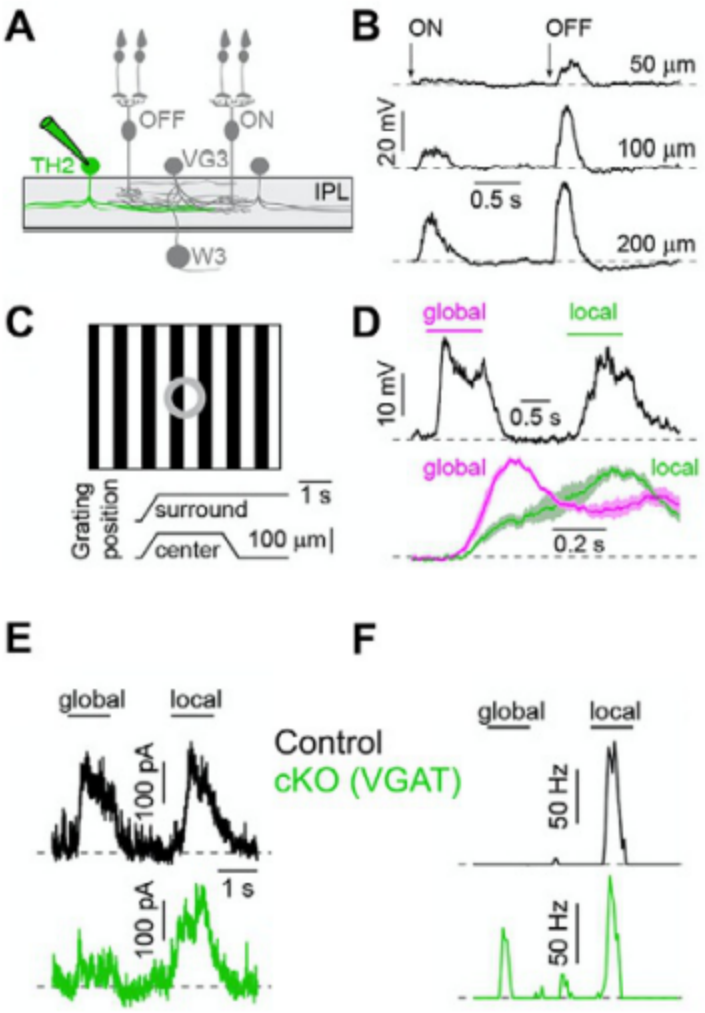

Fig. 3.5 | Inhibition from TH-2 ACs is part of the OMS circuit.

(**A**) Schematic of recording configuration for **B** and **D**. (**B**) Current-clamp responses of a TH-2 AC for spots of different sizes. (**C**) Stimulus configuration for global and local motion similar to that in **Fig. 3.4**. (**D**) Responses of TH-2 ACs to global and local motion separately (top) and superimposed at a magnified scale (bottom). (**E**) Inhibitory currents in an OMS RGC in control (black) and in a mouse line in which GABA release from TH ACs is disrupted (green). (**F**) Spike responses in an OMS RGC for the same conditions as in **E**. (Modified from Kim and Kerschensteiner[37])

Delayed and OMS excitation from a glutamatergic AC

The most surprising element discovered in OMS circuits has been the type 3 vesicular glutamate transporter (VGluT3) AC. We encountered this cell in Chapter 6, for its role in providing glycinergic inhibition to suppressed-by-contrast RGCs. Here, its role is completely different. These ACs are unique in their expression of the VGluT3, and in this circuit, they actually release glutamate to excite OMS RGCs. Studies from three different groups demonstrated this noncanonical excitatory pathway from VGluT3 ACs in which they release glutamate onto the dendrites of OMS/ W3 RGCs at both light ON and OFF (**Fig. 3.6**; [39–41]. Two of these studies, as well as one previous paper [42], reported the RF properties of the VGluT3 ACs themselves. VGluT3 ACs receive excitation from ON and OFF BCs and strong surround suppression both presynaptically and postsynaptically from other ACs[41,42]. This is the same circuit motif described earlier for OMS, and indeed VGluT3 ACs are themselves OMS, with inhibition provided by spiking ACs[39].

But why does the W3b retinal ganglion cell require this unusual circuit element, since simply having a nonlinear center and surround can be enough to generate OMS? One possible explanation is that the delay of the excitatory signal to the W3b by the addition of the VGluT3 AC allows for a more complete silencing by the distant lateral inhibition during global motion, thus allowing for even better OMS. Indeed, Zhang et al.[36] showed that W3b RGCs tend to have slower excitatory input filters than other mouse RGCs. Additionally, if VGluT3 ACs are already OMS, then this could provide a substrate on which the computation is further enhanced at the level of RGCs.

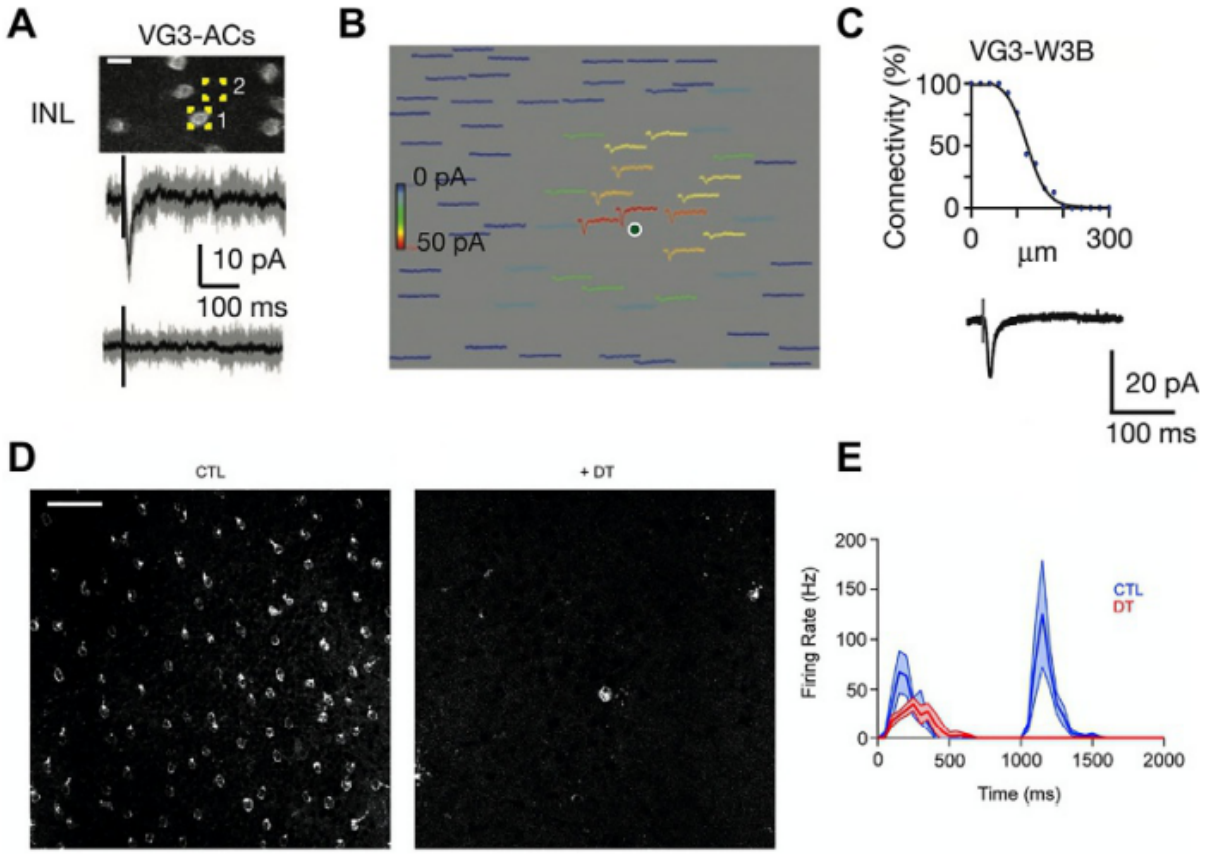

Fig. 3.6 | OMS RGCs receive excitatory input from VGluT3 ACs.

(**A**) Two-photon stimulation of channelrhodopsin in VGluT3 ACs while recording a postsynaptic OMS RGC. Laser stimulation location 1 on a VGluT3 AC elicits an excitatory current in the RGC (top trace), but nearby location 2 does not (bottom trace). Scale bar ¼ is 10 µm. (**B**) Map of postsynaptic responses elicited by stimulation of VGluT3 ACs at different locations relative to the RGC soma (black spot). (**C**) Fraction of VGluT3 ACs eliciting a response in the RGC as a function of their distance from the RGC soma. Example response shown below. (**D**) Image of a region of retina in a VGluT3 AC reporter line expressing the diphtheria toxin receptor in these ACs (left) and the same line following diphtheria toxin administration. Scale bar ¼ 40 µm. (**E**) Average spike responses from OMS RGCs responding to a light step (ON at 0 s, OFF at 1 s) in control conditions and with VGluT3 ACs ablated by diphtheria toxin. (Modified from Krishnaswamy et al.[40]).

How many RGC types are OMS?

Although we have nearly complete knowledge of RGC types in the mouse retina, no comprehensive survey has been completed to determine which of them are OMS. At first glance, the ability to detect object motion seems like a fairly complicated computation and thus might be limited to one or two dedicated cell types. However, we have seen that OMS can arise simply by canceling the nonlinear receptive field center with nonlinear surround suppression. Nonlinear surround suppression is widespread among RGCs (see **Chapter 8**) and perhaps also among ACs[39], raising the possibility that OMS could be a common functional feature of retinal circuits.

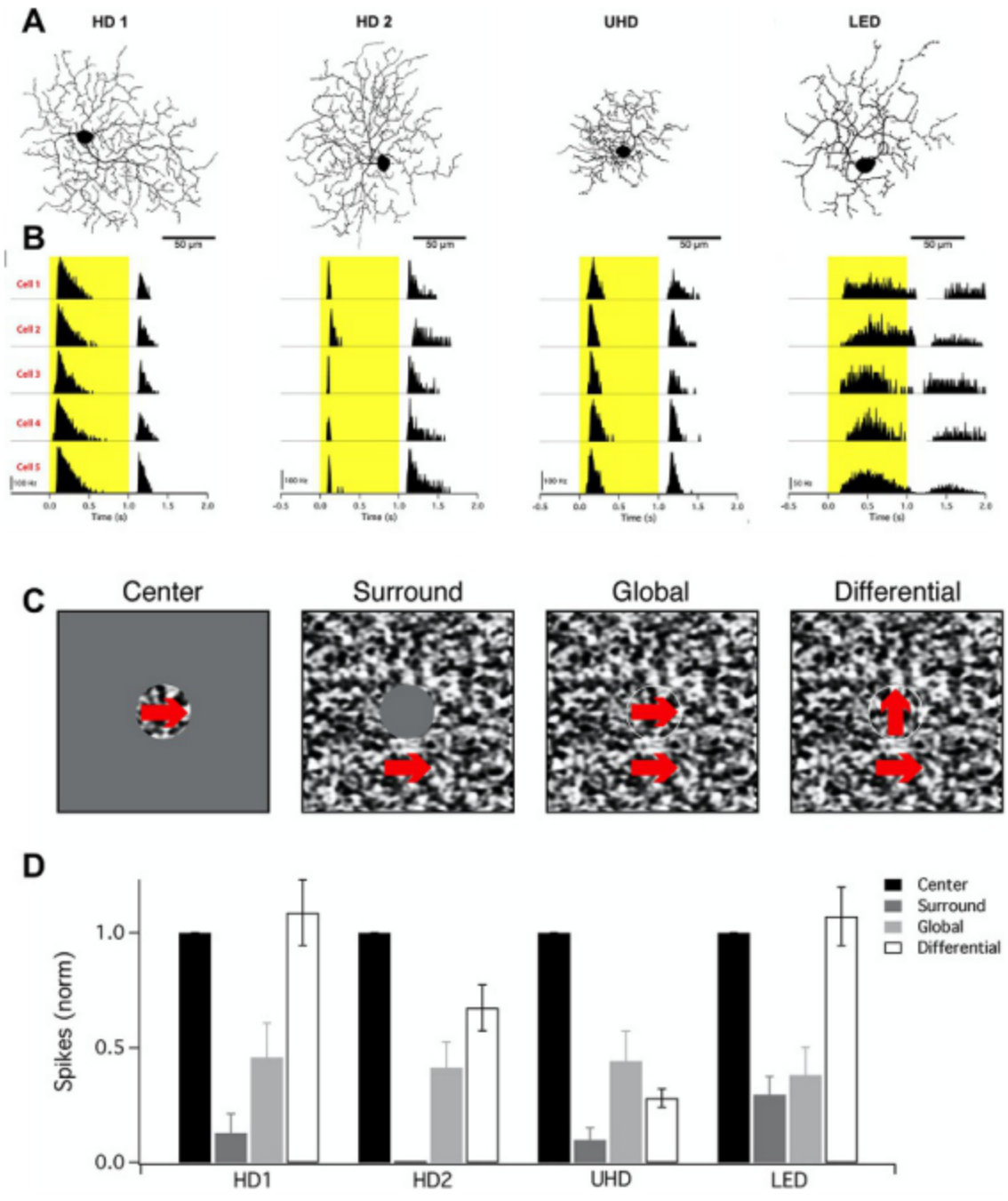

Fig. 3.7 | Four different RGC types are all suppressed by global motion relative to local motion. (**A**) Morphologies of four small-RF, surround-suppressed RGCs in the mouse retina. (**B**) Five examples of spike responses from each RGC type to the presentation of a small spot centered on the RF. (**C**) Motion stimulus paradigms in which textures are drifted in the center, surround, globally, or differentially

by shifting the center motion direction 90 degrees relative to that of the surround. (**D**) Mean responses of the four RGC types to each type of motion stimulus. (Modified from Jacoby and Schwartz[23]).

Indeed, Jacoby and Schwartz[23] described four different RGC types in the mouse with small receptive fields and strong surround suppression (**Fig. 3.7**). The morphological similarities between these four types add to the possibility that they could have been erroneously grouped in previous studies. Each cell type had nonlinear centers and surrounds. When tested with a stimulus in which textures either moved synchronously across both center and surround (global motion) or with the center and surround offset 90 degrees in their movement direction (differential motion), the authors found a spread of OMS. Two of the cell types were highly OMS (LED and HD1), one cell type was only slightly OMS (HD2), and the last type was not at all OMS (UHD). However, all four of these cells would have been considered OMS under the definition imposed by other mouse studies since they all responded more strongly to local motion (RF center alone) than to global motion.

Is direction selectivity related to OMS?

One might expect OMS to be a useful feature in RGCs that are also direction-selective (DS) since both computations deal with motion. Olveczky et al.[34] showed that ON-OFF DS cells in the rabbit were OMS cells, indicating that they would respond to differential motion in a preferred direction under naturalistic conditions. Kuhn and Gollisch[43] reported a group of OMS-DS RGCs in salamander that encoded a specific direction of motion (**Fig. 3.8**). The OMS-DS RGC type in this study had smaller RFs than the non-OMS DS RGCs, further implicating surround suppression in OMS.

The lack of OMS in most DS cells might actually be important for their behavioral role. In mouse and rabbit, both ON DS RGCs and ON-OFF DS RGCs have been implicated in sensing the direction of optic flow induced by locomotion [15,44]. An OMS RGC would be suppressed by the global motion caused by optic flow. Perhaps, DS cells specifically avoid OMS by receiving linear or weak surround suppression or by timing excitation and inhibition to avoid suppression during global motion.

Why have multiple RGC types that are OMS?

Movement is varied and ubiquitous within natural visual scenes. Having multiple OMS RGC types could allow cell types to occupy different niches in stimulus space, such as object size, acceleration, or velocity. The RGC types described by Jacoby and Schwartz[23] each had distinct size and speed tuning. Whether these cells are silenced by particular background motion depends on matching the temporal selectivity of excitation in the center and inhibition from the background. Therefore, different OMS RGCs types might then be better suited for supporting different behaviors, such as canceling out activity caused by random jitter from fixational eye movements, tracking an object during locomotion-induced smooth optic flow, canceling out activity caused by fixational eye movements, or promoting the perceptual suppression that briefly occurs following saccades. More comprehensive studies of the OMS computation, aided by our improved knowledge of mouse RGC types, will be important in parsing out the subtleties in what appears to be a fairly general circuit motif in the retina.

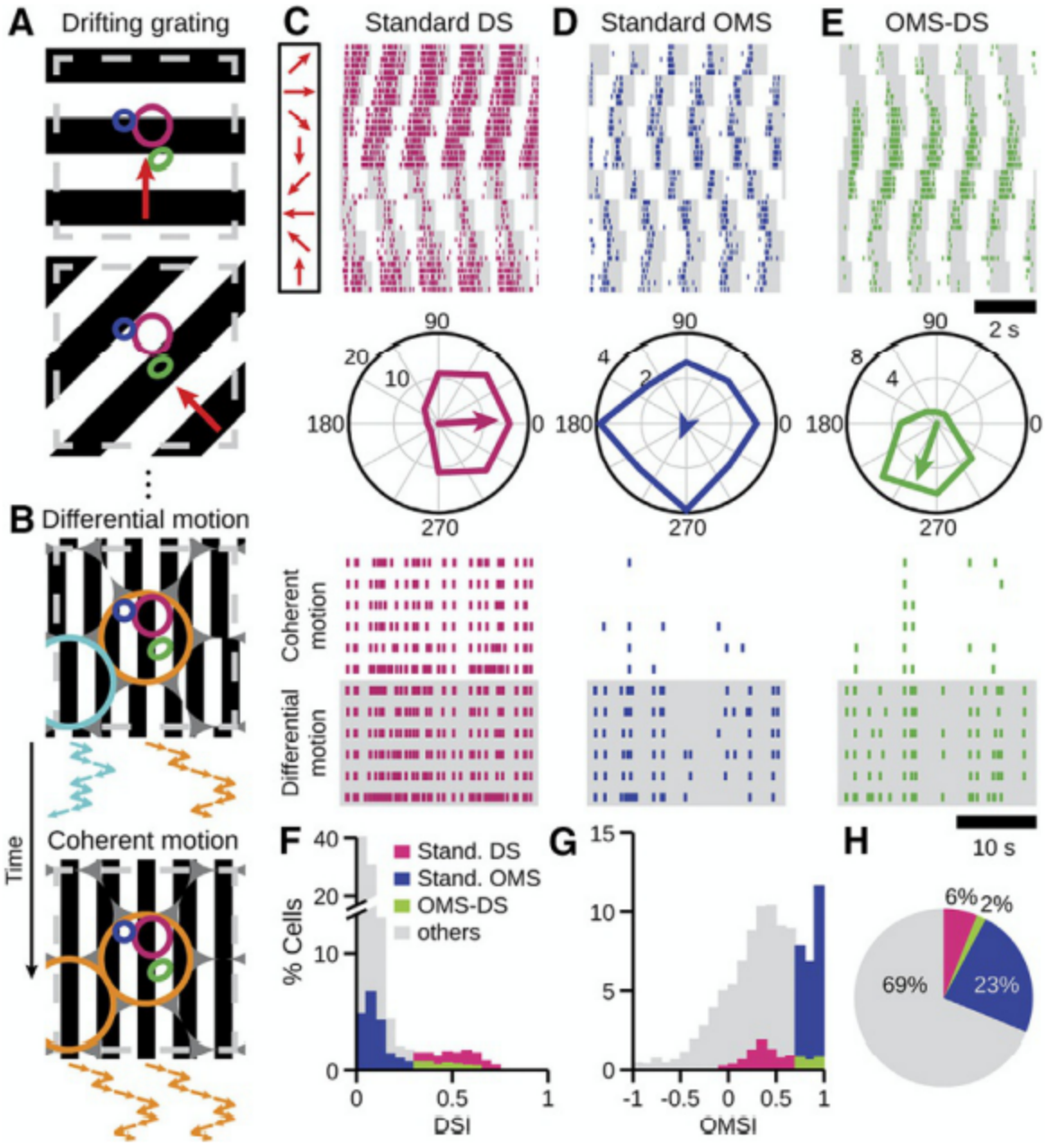

Fig. 3.8 | A population of RGCs in salamander is both OMS and direction selective.

(**A**) Global drifting grating stimulus presented at different directions. (**B**) Differential motion stimulus in which separate, circular patches of the stimulus move with either different trajectories (top) or coherently (bottom). (**C**) Example spike raster (top) and polar plot (bottom) of a “Standard DS” RGC stimulated with drifting gratings. Bottom, spike rasters for the coherent and differential motion stimuli

shown in **B**. (**D**) Same as **C** but for a “Standard OMS” RGC. (**E**) Same as **C** but for an “OMS-DS” RGC. (**F**) Distribution of direction selectivity index (DSI) for all cells including the three types above (corresponding colors) and other RGCs (gray). (**G**) Same as **F** but for object motion sensitivity index (OMSI). (**H**) Pie chart showing the percentage of each type in the recorded population. (From Kuhn and Gollisch[43])

Methods

Ex vivo retina preparation

Wild-type mice (C57BL/6, Jackson Lab Strain # 000664) of either sex aged 6 - 36 weeks were used for recordings and imaging.

Whole mount retinas were prepared in a similar manner to previous publications[12,13,23,28–31]. In short, dark-adapted mice were sacrificed, and retinas were dissected under infrared illumination (940 nm). The intact retina was flat-mounted photoreceptor side down on a poly-D-lysine-coated glass coverslip and placed in a recording chamber. Retinas were perfused with oxygenated Ames medium at 32°C at a rate of 10 mL/min throughout the experiment. Animals were sacrificed following animal protocols approved by the Center for Comparative Medicine at Northwestern University.

Cell-attached recordings

All recordings were obtained using a 2-channel patch-clamp amplifier (Multiclamp 700B, Molecular Devices) sampling at 10 kHz. Spike trains were recorded using glass pipettes (2–3MΩ) filled with AMES solution in cell-attached configuration.

Visual stimulation

Visual stimuli were generated with a 912 x 1140 pixel DLP projector (1.3 µm/pixel) at a 60 Hz frame rate using a blue LED (450 nm) focused on the photoreceptor outer segments. Light intensities are reported in rhodopsin isomerizations per rod per second (R*/rod/s). Each cell’s receptive field center was determined

by flashing horizontal and vertical bars at different locations, and all subsequent stimuli were centered on the location that elicited maximal responses.

Four different stimulus paradigms were used to investigate object motion sensitivity and surround suppression.

Moving objects stimuli:

The "moving objects" stimuli consisted of a circular object with a fixed vertical square grating layered on top of a vertical square background grating. Both the object and background grating had bar widths of ~100 um. The center object had a diameter that roughly corresponded to the size of the receptive field center as determined by the spots of multiple-size stimuli (see below). After a two-second adaptation period, the object and background positions began moving, and the movement continued for 14 seconds. The movement followed random Brownian motion with step sizes of 1.3 μm lowpass filtered by 5 Hz. This motion occurred across a 180 μm standard deviation of distance from the receptive field center. During global motion trials, the object and background moved in synchrony with the same random seed. During object motion trials, the object and background moved independently from each other with differing random seeds.

The object motion sensitivity index (OMSI) was calculated as

$OMSI = (R_{object} - R_{global}) / (R_{object} + R_{global})$,

with R_{object} indicating the RGC's spiking response during object motion and R_{global} indicating the RGC's spiking response during global motion.

Differential motion stimuli:

The second stimulus paradigm, termed "differential motion", was the same as the object motion stimuli, except that the object position was fixed at the center of the RGC's receptive field. Instead of the object itself moving, the gratings within the object's aperture moved according to Brownian motion.

Reversing contrast stimuli:

The third stimulus paradigm, termed “reversing contrast”, consisted of the same object and background gratings as the previous two stimulus paradigms; however, no actual movement occurred. Instead, the contrast of the bars simply reversed, with bright bars switching from 100% contrast to -100% contrast and dark bars switching from -100% contrast to 100% contrast. During the “center” trials, the object and background were uniform. After the two-second adaptation period, the object reversed the contrast of its bars so that it was 180° phase-shifted compared to the background gratings. during the global trials, both the center and background shifted their phase synchronously after the two-second adaptation period.

Spots of multiple sizes stimuli:

The fourth stimulus paradigm, termed “spots of multiple sizes”, measured surround suppression using a pseudorandom sequence of 12 spot sizes (diameters logarithmically spaced from 30-1200 μm) each presented for 1 second. RGC spiking responses were measured as the average spike rate during and 1-second following the visual stimulus. The preferred size response ($R_{preferred\ size}$) was defined as the maximal response measured during the presentation of all sizes of spot stimuli (30 - 1200 μm diameter). The full-field response ($R_{full\text{-}field}$) was defined as the response recorded during the presentation of the largest stimulus spot (1200 μm diameter). The suppression index (SI) was calculated as $SI = (R_{preferred\ size} - R_{full\text{-}field}) / (R_{preferred\ size} + R_{full\text{-}field})$.

Results

When measuring object motion sensitivity using the moving object stimulus (see methods), we found that OMS varied across and within cell types (**Fig. 3.9**). Although the data is preliminary, we did see that many RGC types with weak surround suppression, such as the ON alpha, M2, ON transient MeRF, OFF sustained alpha, and OFF transient alpha, had much lower OMS when compared to RGC types with strong surround suppression, such as the ON transient EW6t, ON transient SmRF, OFF transient small RF, F-mini-ON, Local Edge Detector, HD1, HD2, and UHD ($p<0.05$, ANOVA). We also note that these RGC types with high OMS also tended to have transient responses and smaller receptive field sizes.

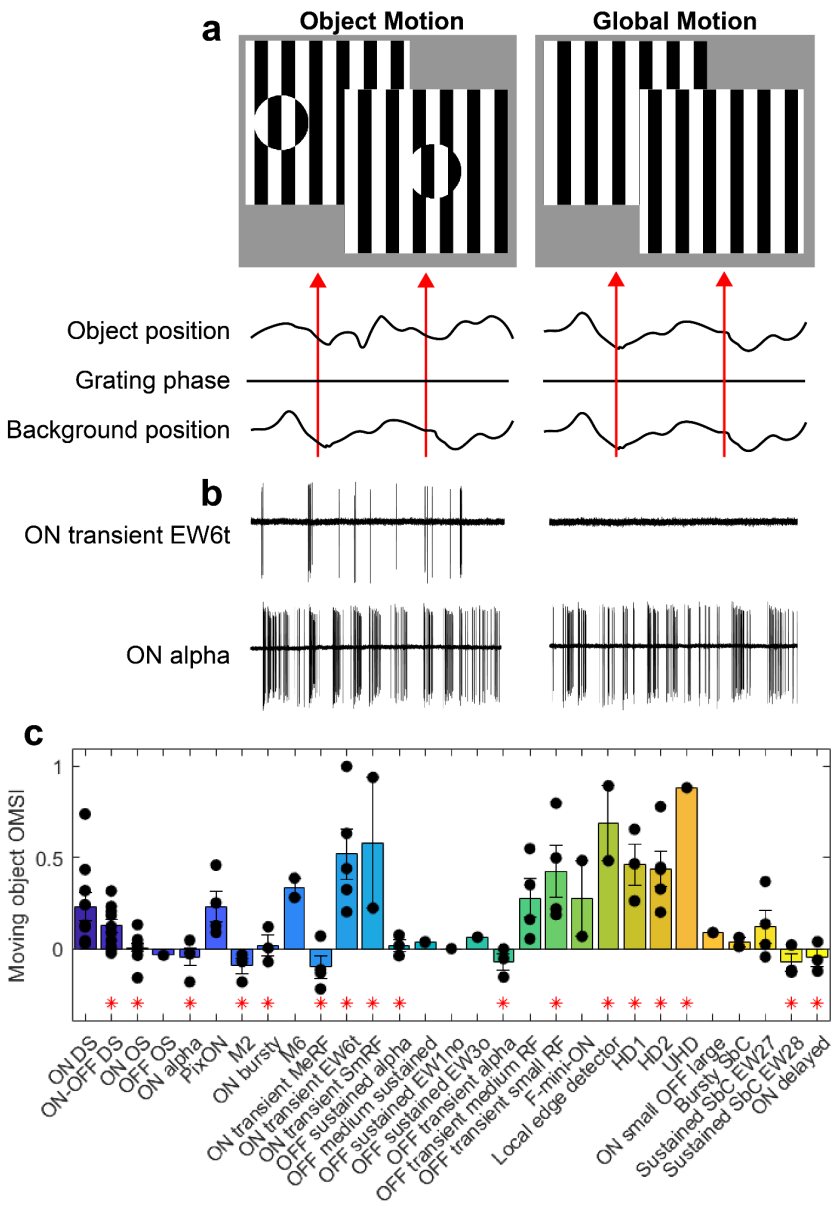

Fig. 3.9 | Object motion sensitivity across cell types.

(**a**) Object motion stimuli in which an object moved differently than the background. Responses were compared to the global motion stimulus in which the object and surround moved synchronously (see methods for more details). (**b**), Example spiking responses from an RGC with high OMS (ON transient EW6t) and an RGC with low OMS (ON alpha). (**c**), Object motion sensitivity index (OMSI) was calculated for each RGC grouped by cell type. Black dots indicate data from individual cells.

Since Baccus et al. [35] showed that OMS could be computed by static receptive field properties, namely nonlinear surround suppression, we sought to test the predictive power of visual stimuli in which the position of the object did not actually move. We first examined RGC responses to differential motion, in which the object's position did not move across the RGC's receptive field, but the grating texture within the static object did move (**Fig 3.10a**). We found that selectivity for this differential motion strongly predicted the RGC's sensitivity to object motion (**Fig 3.10b**, r^2=0.80). The next visual stimuli we tested removed motion altogether, with the center and surround grating textures simply reversing their contrast (**Fig 3.10c**). We expect this stimulus to measure the RGC's nonlinear surround suppression. Surprisingly, this stimulus was a relatively poor predictor of object motion sensitivity (**Fig 3.10d**, r^2=0.16). Finally, we tested a visual stimulus in which a static spot activated the RGCs center and compared these responses to full-field stimuli that activated both the center and surround (**Fig 3.10e**). We expect this stimulus to measure the RGCs' surround suppression, agnostic to its nonlinearity. We found this stimulus to be a moderately strong predictor of OMS (**Fig 3.10f**, r^2=0.16). While it was unexpected that the stimuli which measured surround suppression (**Fig 3.10e**) would better predict OMS than the stimuli which measured *nonlinear* surround suppression (**Fig 3.10c**), it should be noted that these stimuli differed in other ways; specifically, the spot stimuli were presented from a dimmer background light intensity resulting in a higher level of contrast.

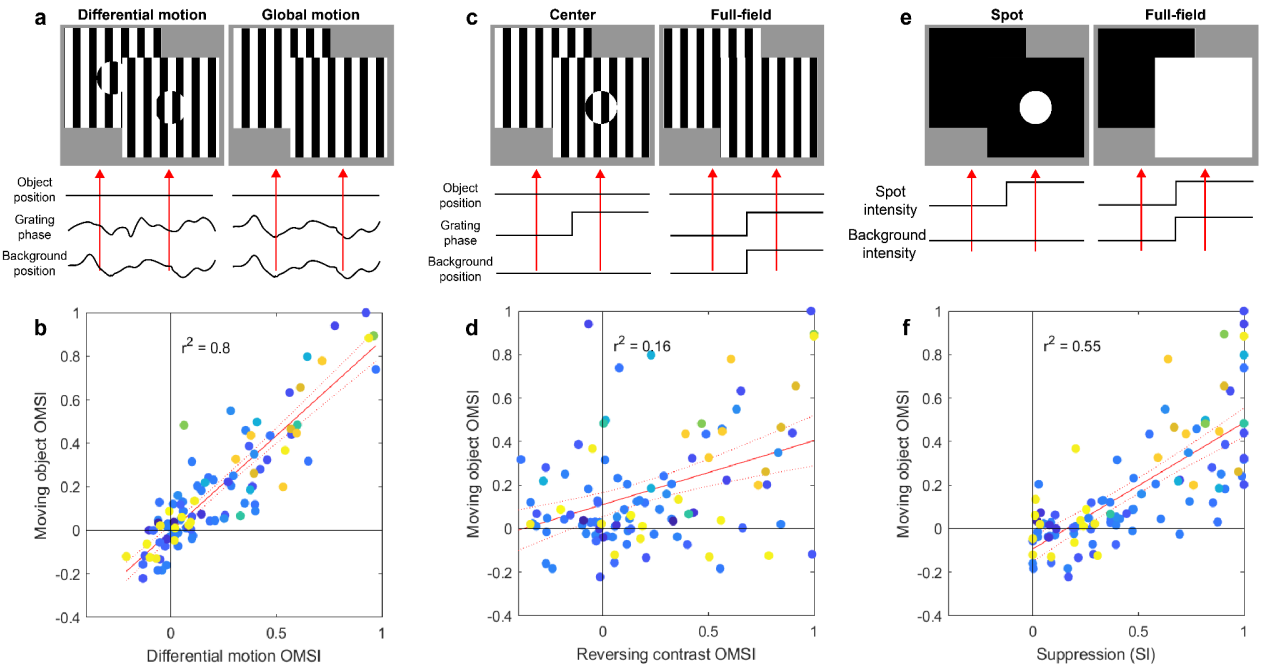

Fig. 3.10 | Object motion sensitivity predicted by stimuli without object motion.
(**a**) Stimuli in which the object remained in the center of the RGC's receptive field, but the grating texture of the object shifted either differently (differential motion) or in synchrony (global motion) with the background grating. (**b**) Prediction of OMSI from responses to the differential motion stimuli depicted in **a**. Red line indicated linear fit with dotted lines representing 95% confidence bounds of fit. r^2 indicates the proportion of variance in moving object OMSI described by the variance of differential motion OMSI. Dots indicate individual RGCs (same cells as **Fig 3.9c**) colored according to their cell type. (**c**) Stimuli in which the object and background do not experience smooth motion but instead reverse the contrast of their grating textures. (**d**) Same as **b**, but predicting moving object OMSI from the stimuli shown in **c**. (**e**) Stimuli in which a static spot is presented to either the receptive field center or full-field. (**f**) same as **b**, but predicting moving object OMS from the stimuli shown in **c**.

Since the analysis in **Figure 3.10** predicted OMS while blind to RGC type, we sought to examine the additional variance explained when accounting for random effects across cell types. To do this, we fit the data from **Figure 3.10** with a linear mixed-effects model with RGC cell type as the grouping variable. Including cell type increased the explained variance most for the reversing contrast stimuli, but had little impact on data from the differential motion stimuli (**Fig 3.11**).

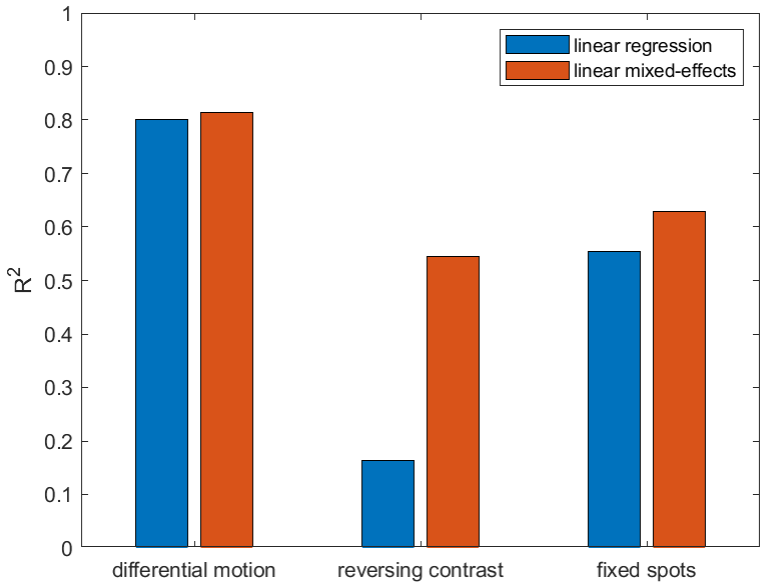

Fig. 3.11 | Incorporation of RGC subtype through a linear mixed-effects model.

R^2 indicates The proportion of variance in moving object OMSI described by data from the three visual stimuli shown in **Figure 3.10**. Linear regression (blue) is modeled without RGC type as a predictor. Linear mixed-effects (red) are modeled with RGC cell type as a grouping variable.

Chapter 4: A presynaptic source drives differing levels of surround suppression in two mouse retinal ganglion cell types

Abstract

In early sensory systems, cell-type diversity generally increases from the periphery into the brain, resulting in a greater heterogeneity of responses to the same stimuli. Surround suppression is a canonical visual computation that begins within the retina and is found at varying levels across retinal ganglion cell types. Our results show that divergence in the level of surround suppression occurs subcellularly, at bipolar cell synapses. Using single-cell electrophysiology and serial block-face scanning electron microscopy, we show that two retinal ganglion cell types exhibit very different levels of surround suppression even though they receive input from the same set of bipolar cell types. This divergence of the bipolar cell signal occurs through synapse-specific regulation by amacrine cells at the scale of tens of microns. These findings indicate that each synapse of a single bipolar cell can carry a unique visual signal, expanding the number of possible functional channels at the earliest stages of visual processing.

Introduction

Visual processing is already well underway in the retina. The analog luminance, contrast, and wavelength representation that begins in photoreceptors are transformed into >40 unique, behaviorally relevant channels of digital information that exit the retina via spikes in retinal ganglion cell (RGC) axons. Stratification of the presynaptic bipolar cell (BC) and amacrine cell (AC) interneurons and the RGC dendrites within sublaminae of the inner plexiform layer (IPL) is an established organizing principle by which retinal circuits build feature selectivity[1,45–47]. Nonetheless, the number of functionally distinct RGC types exceeds their stratification diversity[10,45,48]. What circuit motifs enable RGC types with nearly identical stratification patterns to have different light responses?

Previous studies have identified contributions to functional divergence from precise wiring specificity even within the same IPL sublamina[49] or from differences in intrinsic properties of the RGCs[31,50]. Here, we examine such an example where two RGC types receive the same set of excitatory inputs but exhibit

functionally distinct output signals. We isolate the circuit location at which their functions diverge, and surprisingly, it is at the level of BC output synapses, despite the commonly held view of BCs as electrically compact neurons that constitute a single information channel.

We compared two RGC types in the mouse (Pix_{ON} and ON alpha) that share very similar patterns of IPL stratification but show a striking difference in feature selectivity. The visual feature that we investigated is surround suppression: one of the oldest and best-studied visual computations[51]. The first recordings of the receptive fields (RFs) of mammalian RGCs showed a center region that was antagonized by the surrounding region, resulting in weaker signals to large stimuli than stimuli covering only the RF center[52]. Over the many decades of work that followed, it has become clear that surround suppression is not computed by a single mechanism, but instead differs by species and cell types and can arise at multiple locations in the retina[51]. We sought to identify the circuit locations at which surround suppression is computed in Pix_{ON} RGCs, where it is particularly prominent[53] as compared to ON alpha RGCs, where it is much weaker[54].

Surround suppression has largely been considered to be driven by wiring patterns between specific cell types. However, we show that Pix_{ON} and ON alpha RGCs have very similar circuit connectivity, particularly in their excitation, but show very different surround suppression. We find that these differences in suppression are inherited from differences in the RGC presynaptic excitatory drive, suggesting that this computation occurs at the subcellular level. These findings reveal a new location for the computation of a classical receptive field property. More generally, they suggest that subcellular computation imparts neural circuits with even more capacity for functional divergence than can be inferred from their synaptic wiring diagrams.

Results

The Pix_{ON} RGC has stronger surround suppression than the ON alpha RGC

We identified Pix_{ON} and ON alpha RGCs by their unique morphology and light responses[10,53,54]. These two RGC types have large dendritic arbors that primarily stratify in sublamina 5 of the IPL and exhibit

ON-sustained light responses (**Fig. 4.1a,b**). Despite their many similarities, the Pix_{ON} and ON alpha have been shown to correspond to two unique cell types[10,53,55,56]. Morphological characteristics, such as soma size and arbor complexity, do differ between the two cell types, and ON alpha but not Pix_{ON} RGCs are SMI-32 immunoreactive (**Supplementary Fig. 4.1** and [ref**.** [57]]). The Pix_{ON} and ON alpha RGC types both exhibit weak intrinsic light responses and correspond to the M5 and M4 intrinsically photosensitive RGC types, respectively (**Supplementary Fig. 4.1** and [refs. [55,58]]). Functionally, these RGC types exhibit differing excitatory, inhibitory, and spiking receptive fields (**Fig. 4.1c-k**).

The most obvious way in which the Pix_{ON} and ON alpha RGC's receptive fields differ is in their magnitude of surround suppression. Both RGC types exhibited ON sustained spiking responses when presented with a 200 μm diameter spot of light (**Fig. 4.1c**). However, when presented with large stimuli (1200 μm diameter spot), the Pix_{ON} RGC's spike response was strongly suppressed, while the ON alpha's spike response was only weakly suppressed (**Fig. 4.1d,e**; Pix_{ON} suppressed 89 ± 1.8%, n=46; ON alpha suppressed 26 ± 1.8%, n=90; $P<10^{-47}$). This difference in surround suppression between the two RGC types was present in both scotopic and photopic conditions (**Supplementary Fig. 4.2**) and across retinal locations (**Supplementary Fig. 4.3**).

To investigate if synaptic conductances could lead to the differing levels of surround suppression in these two RGC types, we voltage-clamped both cell types and recorded excitatory and inhibitory synaptic conductances across stimulus size. Previous work demonstrated that Pix_{ON} RGCs have spatially distinct regions of their receptive fields in which they receive excitation and inhibition[53], so we took advantage of this property to confirm that voltage-clamp effectively isolated excitation and inhibition (**Supplementary Fig. 4.4**). The excitatory conductances of both RGC types mirrored their spike responses; the Pix_{ON} excitatory conductances showed strong surround suppression and the ON alpha excitatory conductances showed weak surround suppression (**Fig. 4.1h**; Pix_{ON} suppressed 79 ± 2.0%, n=37; ON alpha suppressed 30 ± 2.1%, n=30; $P<10^{-24}$). As previously reported[53], the Pix_{ON} inhibitory conductances were small for small spot sizes but continually increased for larger

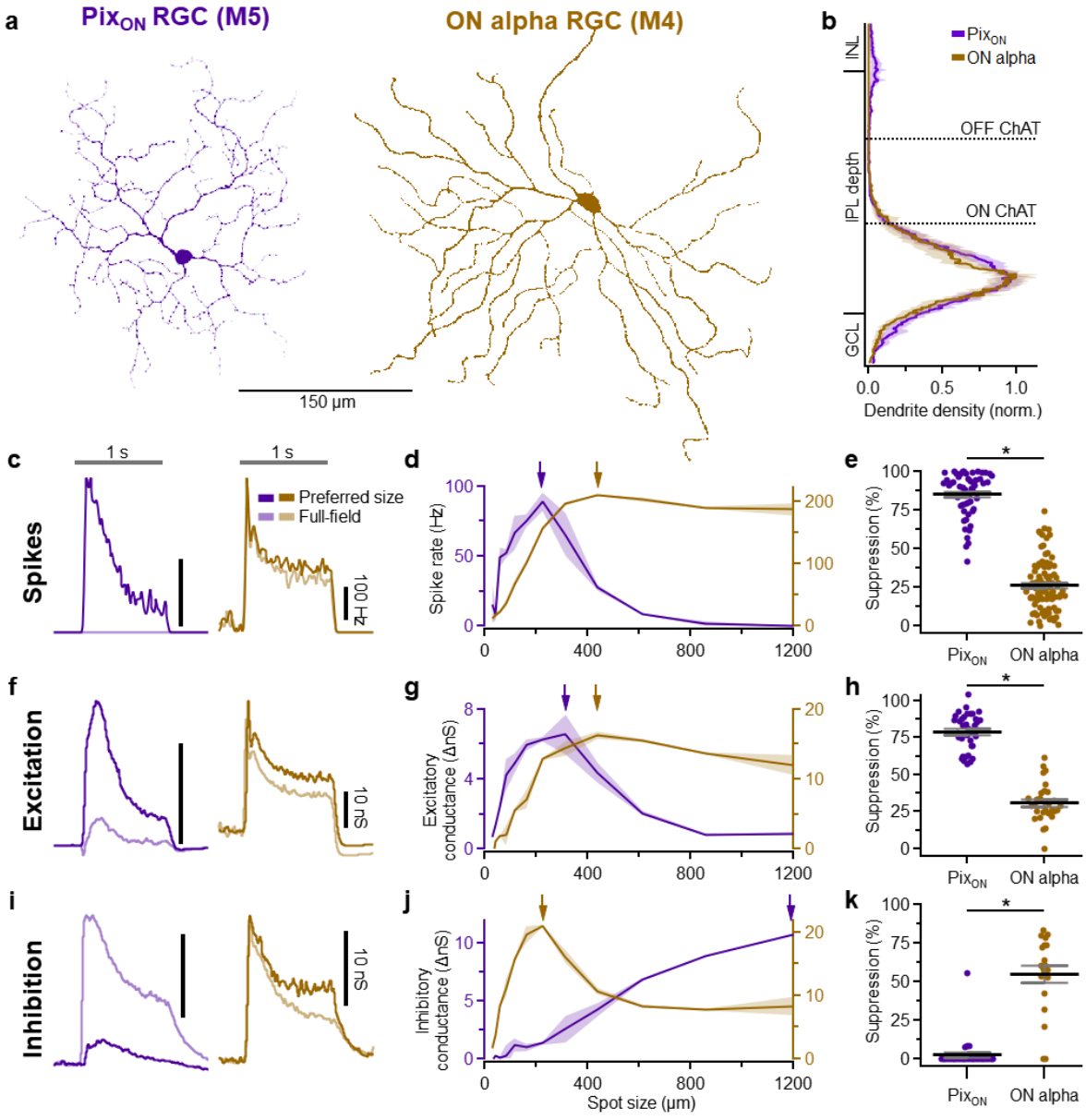
a
Pix$_{ON}$ RGC (M5)
ON alpha RGC (M4)
150 µm
b
Pix$_{ON}$
ON alpha
INL
OFF ChAT
IPL depth
ON ChAT
GCL
0.0
0.5
1.0
Dendrite density (norm.)
c
1 s
1 s
Preferred size
Full-field
Spikes
100 Hz
d
Spike rate (Hz)
e
Suppression (%)
Pix$_{ON}$
ON alpha
f
Excitation
10 nS
g
Excitatory conductance (ΔnS)
h
i
Inhibition
10 nS
j
Inhibitory conductance (ΔnS)
Spot size (µm)
k

Fig. 4.1 | Surround suppression is stronger in Pix_{ON} RGCs than in ON alpha RGCs.
(**a**) *En-face* view of a Pix_{ON} (purple) and an ON alpha (brown) dendritic arbor. (**b**) Dendritic stratification of Pix_{ON} (n=19) and ON alpha (n=10) RGCs within the inner nuclear layer (INL), inner plexiform layer (IPL), and ganglion cell layer (GCL). Dotted lines refer to the ON and OFF choline acetyltransferase (ChAT) bands used to determine stratification. (**c**) Example peristimulus time histograms to preferred size and full-field light spot stimuli. The gray horizontal bar indicates the 1-second presentation of the 250 R*/rod/s spot stimulus from a background luminance of ~0.3 R*/rod/s. (**d**) Example spike rate across a range of spot sizes. Arrows indicate the preferred spot size. (**e**) Surround suppression of spiking response for Pix_{ON} (n=55) and ON alpha (n=90) RGCs. Dots indicate data from individual cells. Bar plots indicate average ± s.e.m., *P<0.05, Welch's t-test. (**f-h**) Same as **c-e** but measuring excitatory conductances via whole-cell voltage clamp configuration. (**h**) Pix_{ON} (n=37) and ON alpha (n=31). (**i-k**) Same as **c-e** but measuring inhibitory conductances via whole-cell voltage clamp configuration. (**k**) Pix_{ON} (n=32) and ON alpha (n=21).

spot sizes. In contrast, the ON alpha inhibitory conductances were large for small spot sizes and moderately suppressed for larger spot sizes (Fig. 1k; Pix_{ON} suppressed 2.6 ± 2.8%, n=31; ON alpha suppressed 55 ± 5.3%, n=21; $P<10^{-8}$).

Excitatory synaptic conductances drive surround suppression

The differing levels of surround suppression between the Pix_{ON} and ON alpha RGC types could be driven by differences in synaptic conductances (e.g., excitation and inhibition, see **Fig. 4.1f-k**) or by differences in cell-intrinsic factors (e.g., voltage-gated channels). To independently test the contribution of synaptic conductances and cell-intrinsic factors, we used dynamic clamp to simulate previously recorded Pix_{ON} and ON alpha excitatory and inhibitory conductances in a new set of Pix_{ON} and ON alpha RGCs (**Fig. 4.2a**). **Figure 4.2b-g** shows that strong surround suppression occurred when simulating Pix_{ON} conductances in either Pix_{ON} RGCs (suppressed 99 ± 0.4%, n=4) or ON alpha RGCs (99 ± 1%, n=3). In contrast, the simulation of ON alpha conductances induced weak surround suppression in both Pix_{ON} RGCs (18 ±

0.9%, n=4) and ON alpha RGCs (23 ± 5%, n=3). These results show that the differing levels of surround suppression in the Pixon and ON alpha spiking responses are driven by their differing conductances (99% of total variance, $p<10^{-12}$), not by cell-intrinsic factors (0.1% of total variance, p=0.22, two-way ANOVA).

To independently test the ability of the Pix_{ON} RGC's excitatory versus inhibitory synaptic conductances to drive its strong surround suppression, we again utilized dynamic clamp. First, we simulated excitatory and inhibitory conductances for the preferred spot size. To test the role of excitation, we then measured how much the preferred spot spiking response was suppressed when switching to full-field excitatory conductances, but maintaining the same preferred size inhibition. Likewise, to test the role of inhibition, we measured how much the preferred spot spiking response was suppressed when simulating full-field inhibition and preferred size excitation (**Fig. 4.2f)**.

We found that both inhibition and excitation induced some level of surround suppression. However, full-field excitation induced significantly more surround suppression (96 ± 3%) than full-field inhibition (29 ± 3%; n=4, P=0.0002; **Fig. 4.2g**). These results suggest that suppression of the Pix_{ON} excitatory conductances by full-field stimuli is an important driver of surround suppression in the Pix_{ON} spiking output. Conversely, the absence of strong surround suppression of the ON alpha excitatory conductances allows the ON alpha RGC to exhibit very little surround suppression in its spiking output. Given the dominant role of excitatory conductances in dictating surround suppression of the spiking output, we next investigated sources that could cause the excitatory conductances of the Pix_{ON} and ON alpha RGCs to experience differing levels of surround suppression.

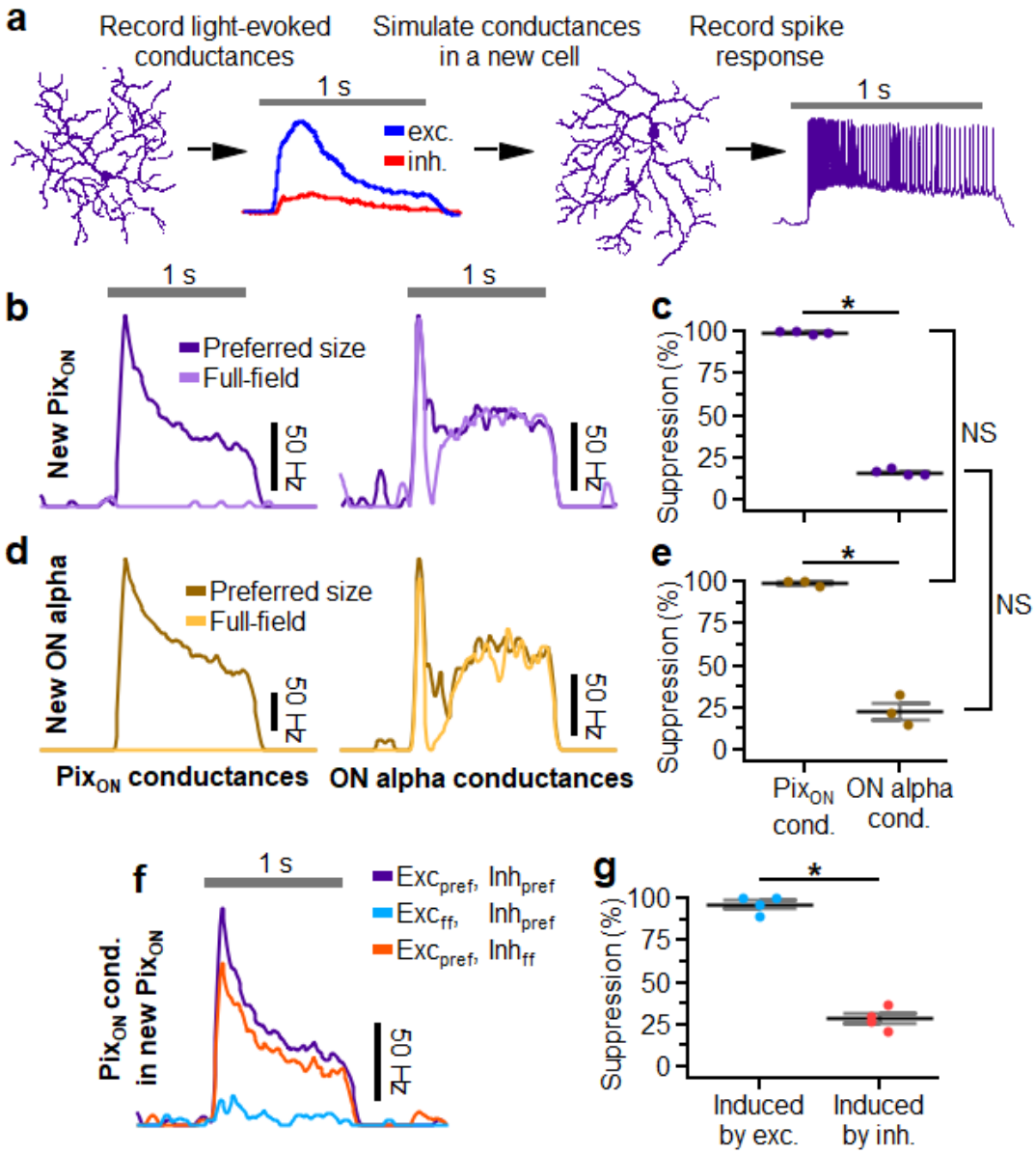
a
Record light-evoked conductances
Simulate conductances in a new cell
Record spike response
1 s
exc.
inh.
1 s
b
1 s
1 s
New Pix$_{ON}$
Preferred size
Full-field
50 Hz
50 Hz
c
*
Suppression (%)
100
75
50
25
0
NS
d
New ON alpha
Preferred size
Full-field
50 Hz
50 Hz
Pix$_{ON}$ conductances
ON alpha conductances
e
*
Suppression (%)
100
75
50
25
0
NS
Pix$_{ON}$ cond.
ON alpha cond.
f
1 s
Pix$_{ON}$ cond. in new Pix$_{ON}$
Exc$_{pref}$, Inh$_{pref}$
Exc$_{ff}$, Inh$_{pref}$
Exc$_{pref}$, Inh$_{ff}$
50 Hz
g
*
Suppression (%)
100
75
50
25
0
Induced by exc.
Induced by inh.

Fig. 4.2 | Excitatory conductances drive differing levels of surround suppression in Pix_{ON} and ON alpha RGCs.

(**a**) Schematic illustrating dynamic clamp protocol in which previously recorded excitatory (blue) and inhibitory (red) conductances are simulated in a new RGC via current injections. (**b**,**c**) Example peristimulus time histogram recorded from a Pix_{ON} RGC when simulating excitatory and inhibitory conductances recorded from a different Pix_{ON} RGC **b** or an ON alpha RGC **c**. "Preferred-size" (dark purple) indicates the maximal spiking response when simulating conductances recorded during 200, 600, and 1200 μm diameter spot stimuli. "Full-field" (light purple) indicates simulation of conductances recorded during 1200 μm spot stimuli. (**d**) Surround suppression of Pix_{ON} spiking responses when simulating conductances recorded from a different Pix_{ON} (left) or an ON alpha (right) (n=8). (**e**-**g**) Same as **b**-**c** but simulating conductances within an ON alpha RGC (n=3). (**h**) Example peristimulus time histogram recorded from a Pix_{ON} RGC when simulating PixON conductances as to isolate the effect of full-field excitation or full-field inhibition. Purple indicates simultaneous simulation of preferred size excitation and inhibition (same as "preferred size" in **b**). Blue indicates the simulation of full-field excitation and preferred size inhibition. Orange indicates simulation of preferred size excitation and full-field inhibition. (**i**) Suppression of the "preferred size" spiking response (purple trace in **h**) that is induced when switching to full-field excitation (blue trace in **h**) or full-field inhibition (orange trace in **h**) (n=4). (**d**,**g**,**i**) Dots indicate data from individual cells. Bar plots indicate average ± s.e.m., n=8 for all conditions, *P<0.05, Significance was determined by Two-way ANOVA for **d**,**g** and paired two-sample Student's *t*-test for **i**.

Postsynaptic saturation or desensitization does not alter surround suppression

Differing levels of surround suppression between the Pix_{ON} and ON alpha excitatory conductances could result from differing expression of glutamate receptors in the two RGC types. If the ON alpha glutamate receptors more easily undergo saturation or desensitization, the

excitatory response to the preferred size stimuli could be blunted compared to the full-field response, resulting in weaker surround suppression.

To test if glutamate receptor saturation or desensitization is necessary for the weak surround suppression in ON alpha RGCs, we measured surround suppression during bath application of subsaturating concentrations of either a weak glutamate receptor antagonist (700 nM kynurenic acid) or a strong glutamate receptor antagonist (300 nM NBQX). While both kynurenic acid (Kyn) and NBQX are expected to decrease the magnitude of the excitatory conductances, only the rapidly dissociating Kyn is expected to reduce glutamate receptor desensitization and saturation[59]. Excitatory conductances were significantly smaller in the presence of either Kyn or NBQX (Kyn 8 ± 7% of control, $P<10^{-2}$; NBQX 20 ± 1% of control, $P<10^{-3}$; n=3; **Fig. 4.3a-c**). However, surround suppression was not stronger in the presence of Kyn compared to NBQX (Kyn suppressed 12 ± 6%; NBQX suppressed 17 ± 1.9%; n=3, P=0.8; **Fig. 4.3c-e**). These results suggest that neither glutamate receptor saturation nor desensitization is responsible for the weak surround suppression observed in ON alpha excitatory conductances.

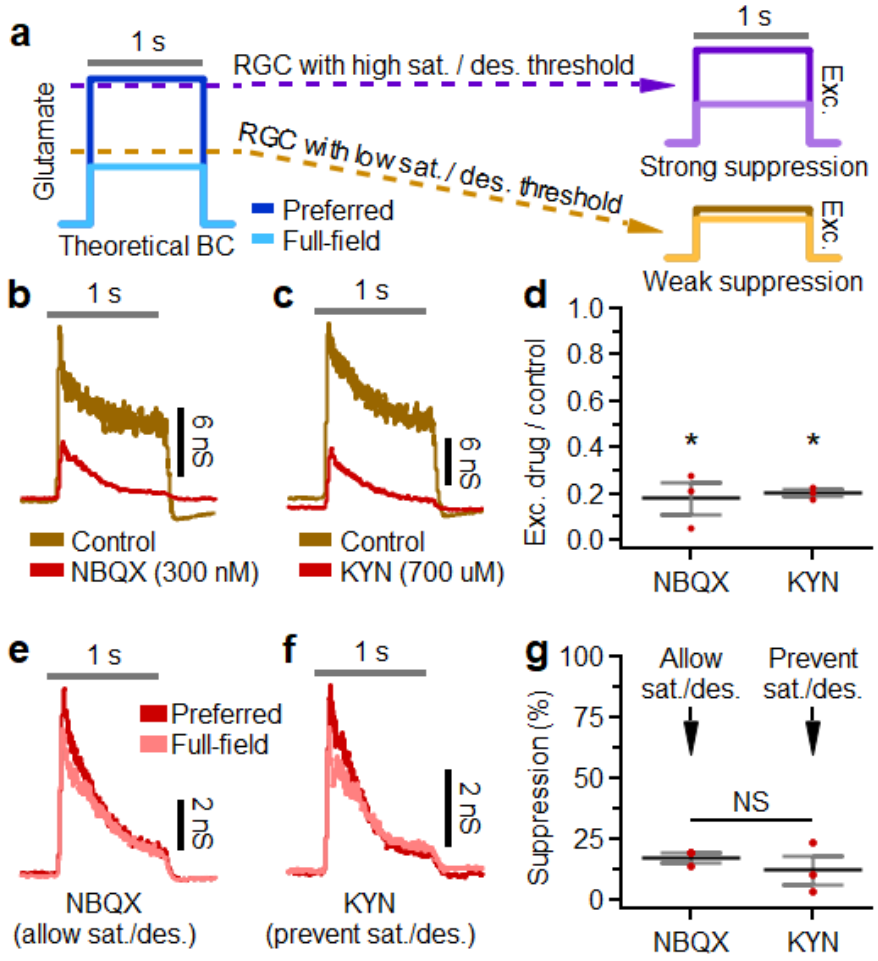

Fig. 4.3 | Weak surround suppression of ON alpha excitatory conductances does not depend on glutamate receptor saturation or desensitization.

(**a**) Example ON alpha excitatory conductances evoked by a preferred spot size in control conditions (brown) or during subsaturating bath application of NBQX (red). (**b**) Same as **a**, but red indicates bath application of kynurenic acid (KYN). (**c**) Proportion of ON alpha excitatory response evoked in NBQX (n=3) or KYN (n=3) compared to control conditions. (**d**) ON alpha excitatory conductances evoked by a preferred (red) or full-field (pink) spot size during bath application of NBQX. (**e**) Same as **d** but during bath application of KYN. (**f**) Surround suppression of ON alpha excitatory conductances in the presence of NBQX (n=3) or KYN (n=3). (**a**,**b**,**d**,**e**) Gray horizontal bar indicates a 1-second presentation of the stimulus. (**c**,**f**) Dots indicate data from individual cells. Bar plots indicate average ± s.e.m., *P<0.05, paired two-sample Student's *t*-test.

Since bath application of pharmacological agents can have unintended effects that complicate interpretation, we also tested for differential saturation of the excitatory currents to Pix_{ON} and ON alpha RGCs with a different, non-pharmacological approach. We stimulated both RGC types with a range of contrast steps. The two RGC types showed similar excitatory contrast response functions, and neither cell type experienced saturation at 100% contrast (**Supplementary Fig. 4.5**). Together, these results suggest that the difference in excitation to Pix_{ON} and ON alpha RGCs that drives their difference in surround suppression is not a result of differential saturation or desensitization of postsynaptic glutamate receptors.

Surround suppression in Pix_{ON} and ON alphas is accurately predicted from differing bipolar cell input but not differing RGC dendritic arbors.

Having demonstrated that glutamate receptor saturation or desensitization is not the source of functionally distinct excitation in Pix_{ON} vs. ON alpha RGCs, we shifted our investigation upstream to the presynaptic BC subunits that drive excitation. An RGC's excitatory receptive field is composed of BC subunits sampled across its dendritic arbor, with each of these BC subunits activated according to its own receptive field. The differing levels of surround suppression between the Pix_{ON} and ON alpha excitatory conductances could occur if their BC subunits had differing receptive fields, such as Pix_{ON} BC subunits exhibiting stronger surrounds. Alternatively, the differing levels of surround suppression between the Pix_{ON} and ON alpha excitatory conductances could be driven by differences in their dendritic arbors, resulting in a different spatial sampling of their BC subunits. Although Pix_{ON} and ON alpha dendritic arbors were similar in many respects, there were differences between the two RGC types, such as the slightly larger dendritic field size of the ON alpha (**Supplementary Fig. 4.1d**), which could cancel out BC subunit inhibitory surrounds over a larger area, resulting in decreased surround suppression of the ON alpha excitatory conductances.

To investigate how these two variables might influence surround suppression of Pix_{ON} and ON alpha excitation, we modeled an RGC's light-evoked excitatory conductances as the summation of BC subunits sampled across its dendritic arbor (**Supplementary Fig. 4.6a**). We estimated the receptive field

properties of these BC subunits by supplying the model with Pix_{ON} or ON alpha dendritic skeletons and then optimizing the BC's center-to-surround ratio (CSR) and receptive field surround size (σ_s) so that the model output best replicated the cell's experimentally measured excitatory response across spot sizes.

Fitting the BC receptive fields to Pix_{ON} RGCs resulted in a smaller CSR (1.1 ± 0.01, median ± median absolute deviation) and a smaller σ_s (75 ± 5 μm) than when fitting to ON alpha RGCs (CSR = 1.8 ± 0.2, σ_s = 100 ± 20 μm; **Supplementary Fig. 4.6c,f**). Encouragingly, these receptive field properties enabled the model to accurately reproduce the experimentally measured Pix_{ON} and ON alpha excitatory responses (**Supplementary Fig. 4.6b,e**) and are within the range of those estimated from ON BCs glutamate signals[60,61].

When cross-validating these BC receptive fields, the model more accurately predicted surround suppression when testing against RGCs of the same type to which the receptive field parameters were fit but failed to accurately predict surround suppression of the opposite cell type (**Supplementary Fig. 4.6d,g**).

When fit to Pix_{ON} RGCs, the model underestimated surround suppression in new Pix_{ON} RGCs by only 5 ± 3% (mean ± s.e.m, n=14) but overestimated surround suppression in ON alpha RGCs by 42 ± 3% (n=8). Conversely, when fit to ON alpha RGCs, the model underestimated surround suppression in new ON alpha RGCs by only 0.8 ± 4% (n=8) but underestimated surround suppression in Pix_{ON} RGCs by 49 ± 3% (n=14).

These results suggest that surround suppression of Pix_{ON} and ON alpha excitatory conductances can be well-described by input from BC subunits with reasonable RF profiles. However, fitting to either Pix_{ON} or ON alpha RGCs did not result in converging BC RF properties and poorly predicted responses in the opposite cell type, suggesting that differing BC RF properties might be required and RGC arbors cannot explain the observed differences between Pix_{ON} and ON alpha RGCs.

To directly test if any BC RF could enable the RGC dendritic arbors to accurately predict both the Pix_{ON} and ON alpha excitatory responses, we simultaneously fit a single BC RF to both RGC types. This resulted in a BC RF that provided a poorer fit to both RGC types and whose surround size was much smaller than previously reported for BC glutamate release (CSR = 1.1 ± 0.04, σ_s = 44 ± 7 μm, **Supplementary Fig. 4.6h,i**[60,61]). When cross-validating against new Pix_{ON} and ON alpha RGCs, this BC RF underestimated surround suppression for Pix_{ON} RGCs by 29 ± 4% and overestimated surround suppression for ON alpha RGCs by 14 ± 3% (**Supplementary Fig. 4.6j**).

Together, these results suggest that BC subunits with different receptive field properties are capable of producing the surround suppression observed in the Pix_{ON} and ON alpha excitatory conductances but differences in the dendritic arbors of Pix_{ON} and ON alphas do not appear capable of producing their differing levels of surround suppression.

Pix_{ON} and ON alpha RGCs receive input from the same bipolar cell types.

If the functionally distinct excitation in Pix_{ON} and ON alpha RGCs is driven by functionally distinct BC input, how might this difference arise? Although Pix_{ON} and ON alpha RGCs have very similar stratification profiles in the IPL where they form synapses with BCs (**Fig. 4.1b**), perhaps they selectively form synapses with different BC types. To determine which BCs types synapse onto the Pix_{ON} and ON alpha RGCs, we carried out serial block-face scanning electron microscopy (SBFSEM) on retinal sections that contained overlapping dendritic arbor of functionally identified Pix_{ON} and ON alpha RGCs. We identified ribbon synapses onto the dendrites of both RGCs (Pix_{ON} n=86, ON alpha n=50,) and reconstructed their presynaptic BCs (**Fig. 4.4a-i**). SBFSEM revealed that the Pix_{ON} and ON alpha RGCs synapsed with the same BC types in similar proportions (**Fig. 4.4j**). Type 6 BCs provided the majority of excitatory synapses to both the Pix_{ON} RGC (60%) and the ON alpha RGC (52%). The remaining synapses were provided by type 7 (Pix_{ON} = 31%, ON alpha = 46%), type 8 (Pix_{ON} = 1%, ON alpha = 2%), and type 9 (Pix_{ON} = 7%, ON alpha = 0%) BCs. The proportion of input from each of these types was not found to be significantly different between the Pix_{ON} and the ON alpha (T6 P=0.7, T7 P=0.3, T8 P=0.7, T9 P=0.2, two-proportions

z-test with Holm-Bonferroni correction). This is also consistent with results from a different SBFSEM volume [62].

Although both RGC types received input from a similar complement of BC types, perhaps the Pix_{ON} and ON alpha RGCs form synapses with distinct subpopulations of cells within the same BC type? This hypothesis seems unlikely as we found multiple examples of individual type 6 (n=6) and type 7 (n=2) BCs that synapsed onto both the Pix_{ON} RGC and the ON alpha RGC (**Fig. 4.4c**).

Since our SBFSEM reconstruction only covered a small area (80 x 150 μm), we sought an additional method to investigate BC input across the entire dendritic arbor of Pix_{ON} and ON alpha RGCs. To do this, we filled Pix_{ON} and ON alpha RGCs with Neurobiotin in a mouse line that fluorescently labels type 6 BCs (CCK-ires-Cre/Ai14 [refs.[63,64]]). We then used antibodies to fluorescently label an excitatory postsynaptic scaffolding protein present at excitatory synapses (PSD95[65], **Supplementary Fig. 4.7a**). After confocal imaging the entire dendritic volume, we identified which PSD95-labeled synapses within the RGC dendrite were apposed to type 6 BCs (**Supplementary Fig. 4.7b**). In agreement with our SBFSEM results, we found that a majority of PSD95-labeled synapses were apposed to type 6 BCs for both Pix_{ON} RGCs (61 ± 2%, n=3) and ON alpha RGCs (72 ± 3%, n=2; **Supplementary Fig. 4.7c**) and these proportions did not significantly differ across dendritic eccentricity for either RGC type (**Supplementary Fig. 4.7d**, Pix_{ON} P=0.25, ON alpha P=0.17, Kolmogorov-Smirnov test).

Amacrine cells regulate the bipolar cell terminal

If the same BCs drive excitatory conductances in both the Pix_{ON} and the ON alpha RGC types, then why is surround suppression different between the Pix_{ON} and ON alpha excitatory conductances? Perhaps surround suppression is generated at a subcellular level within the terminals of these BCs, allowing different output synapses of the same BC to convey either strong or weak surround suppression.

Wide-field ACs are a promising candidate for generating surround suppression in BCs because wide-field spiking ACs have been shown to provide surround suppression of BC depolarization and glutamate release via $GABA_C$ receptors clustered at cone BC output synapses[61,66–68].

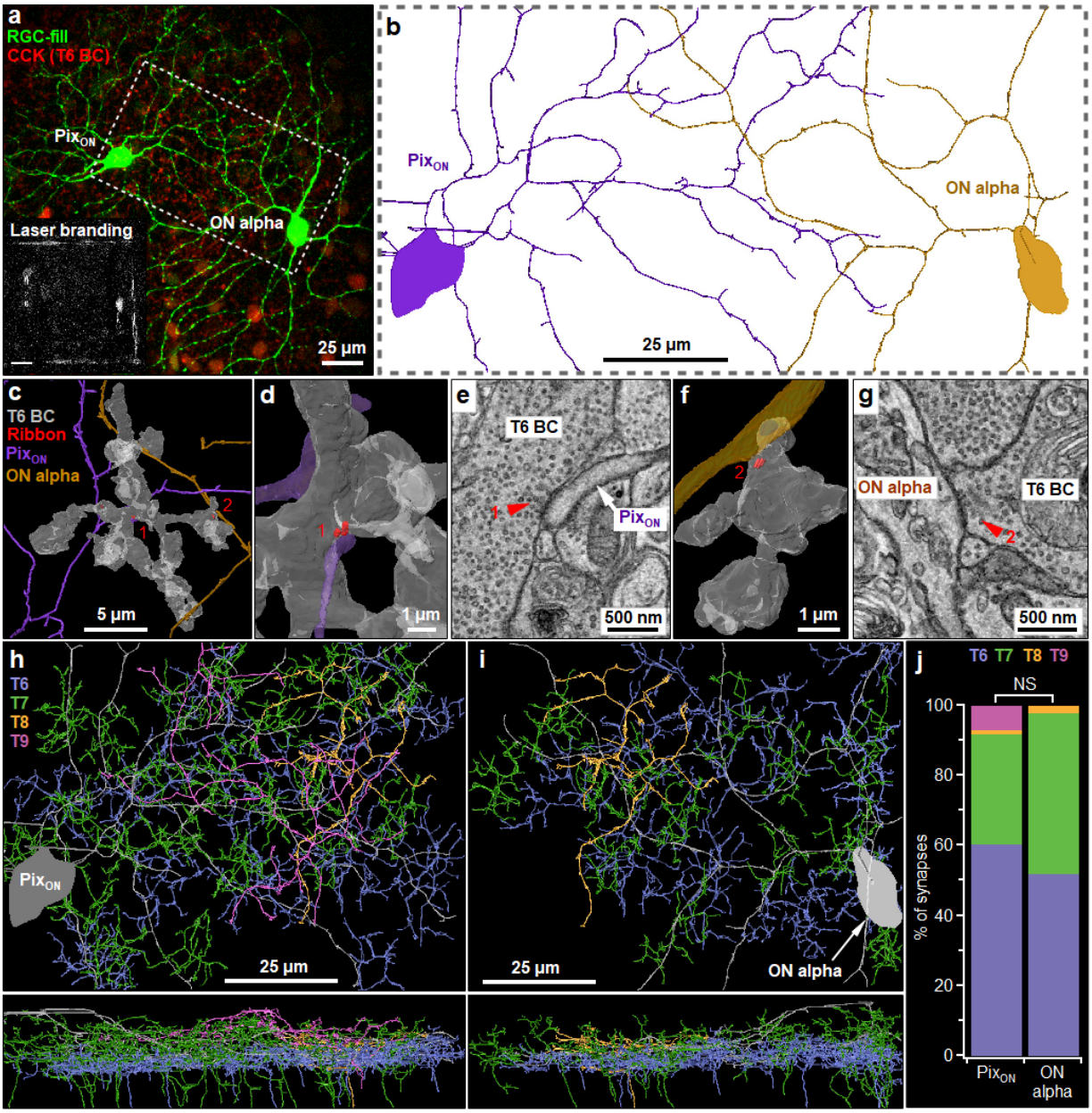
a
RGC-fill
CCK (T6 BC)
Pix$_{ON}$
Laser branding
ON alpha
25 µm
b
Pix$_{ON}$
ON alpha
25 µm
c
T6 BC
Ribbon
Pix$_{ON}$
ON alpha
1
2
5 µm
d
1
2
1 µm
e
T6 BC
1
Pix$_{ON}$
500 nm
f
2
1 µm
g
ON alpha
T6 BC
2
500 nm
h
T6
T7
T8
T9
Pix$_{ON}$
25 µm
i
25 µm
ON alpha
j
T6 T7 T8 T9
NS
100
80
60
40
20
0
% of synapses
Pix$_{ON}$
ON alpha

Fig. 4.4 | Pix_{ON} and ON alpha RGCs receive excitatory input from the same bipolar cells. (**a**) En-face view of filled Pix_{ON} and ON alpha RGCs imaged with 2-photon microscopy in the CCK-ires-Cre/Ai14 mouse line which labels type 6 BCs (T6 BC, red). Inset shows laser burn marks used as fiducial markers during SBFSEM alignment (see methods). (**b**) Pix_{ON} and ON alpha SBFSEM reconstructions of the tissue volume shown in **a**. (**c**) Example reconstruction showing a T6 BC (grey) forming ribbon synapses (red) onto a Pix_{ON} dendrite (purple) and an ON alpha dendrite (brown). (**d**) Reconstruction of a T6 BC ribbon synapse onto a Pix_{ON} dendrite (synapse #1 from **c**). (**e**) SBFSEM slice used to identify ribbon synapses (red arrow) in **d**. (**f**,**g**) same as **d**,**e** but showing a T6 BC ribbon synapse onto an ON alpha dendrite (synapse #2 from **c**). (**h**) En face (top) and cross-sectional view (bottom) of BCs types (T6-T7) presynaptic to the Pix_{ON} RGC. (**i**) same as **h** but for BCs presynaptic to the ON alpha RGC. (**j**) The proportion of synapses formed by each bipolar cell type onto Pix_{ON} (n=86) and ON alpha (n=50) RGCs. Differences in the proportion of BC type between Pix_{ON} and ON alpha were not significant. P>0.05, two-proportions z-test with Holm-Bonferroni correction.

To examine the role of presynaptic inhibition by spiking ACs in generating surround suppression in Pix_{ON} RGCs, we measured Pix_{ON} excitatory conductances in the presence of GABA and glycine receptor antagonists (**Fig. 4.5a,b**). Surround suppression was significantly decreased in the presence of a $GABA_C$ receptor antagonist (control 71 ± 4%; TPMPA 34 ± 4%; n=6, $P<10^{-3}$) but was not significantly altered by the application of a $GABA_A$ antagonist (control 76 ± 9%; gabazine 80 ± 10%; n=3, P=0.8), a $GABA_B$ antagonist (control 77 ± 5%; saclofen 74 ± 5%; n=4, P=0.06), or a glycine receptor antagonist (control 79 ± 9%; strychnine 78 ± 9%; n=3, P=0.7). Additionally, we found that surround suppression was significantly decreased in the presence of a voltage-gated sodium channel blocker (control 85 ± 5%; TTX 43 ± 2%; n=4, P=0.003), which is expected to block spike propagation along the neurites of spiking wide-field ACs. While TPMPA and TTX each significantly reduced surround suppression of the Pix_{ON} excitatory conductances, some surround suppression remained. However, the simultaneous application of TPMPA and TTX completely abolished surround suppression (control 71 ± 4%, TPMPA + TTX 0.3 ± 0.3%, n=2) and had a greater effect than TPMPA alone (P=0.0002), or TTX alone (P=0.0002). Experiments in ON

alpha RGCs showed qualitatively similar effects but decreases in surround suppression but were more difficult to measure since surround suppression of the ON alpha excitatory conductances was already weak in control conditions (**Supplementary Fig. 4.8**). These results suggest that the strong surround suppression observed in the Pix_{ON} excitatory conductances is driven by spiking wide-field ACs via $GABA_C$ receptors at the BC terminal. While these same cells may drive what little surround suppression is present in the ON alpha excitatory conductances, they appear unable to induce the same level of surround suppression as seen in Pix_{ON} RGCs.

While our pharmacology results suggested a role for presynaptic inhibition by spiking GABAergic ACs in generating surround suppression in Pix_{ON} RGCs, they did not offer direct evidence of differential inhibition at synapses to Pix_{ON} vs. ON alpha RGCs. To investigate presynaptic AC inhibition at a subcellular level, we reconstructed the ACs which formed output synapses onto the presynaptic BCs identified in our SBFSEM volume (from **Fig. 4.4**). For each type 6 and type 7 BC ribbon synapse onto the Pix_{ON} and ON alpha RGC, we identified the nearest presynaptic inhibitory site (**Fig. 4.5c**). Although a presynaptic inhibitory site was always found within a few microns of each BC ribbon synapse, this distance tended to be shorter for type 6 BC synapses onto the Pix_{ON} RGC (0.74 ± 0.05 µm, n=51) compared to the ON alpha RGC (1.04 ± 0.1 µm, n=26; P=0.009; **Fig. 4.5f**). However, this difference in presynaptic inhibitory distance was not significant for type 7 BCs (Pix_{ON} = 0.86 ± 0.07 µm, n=14; ON alpha = 0.73 ± 0.05 µm, n=17; P=0.14). We traced the presynaptic ACs at each type 6 BC ribbon to determine if they were a likely candidate to carry inhibition from the surround. Due to the limited size of the SBFSEM reconstruction, only 60% of these ACs could be classified by field size, but all of these were identified as medium to large-field ACs (spanning >40 µm), with none of their somas contained within the reconstructed volume (**Fig. 4.5e**). Additionally, of the nine ACs for which we observed multiple inhibitory feedback synapses onto the type 6 BCs within the field of view, only one provided presynaptic inhibition to both a BC-Pix_{ON} and a BC-ON alpha synapses, suggesting the possibility of synapse preference based on the postsynaptic ganglion cell identity. While we could not determine the specific cell type of these wide-field ACs due to the limited size of the SBFSEM reconstruction, these results show that wide-field AC inhibition is present near each BC output synapse, but is more tightly localized at type 6 BC-Pix_{ON} synapses. This

suggests that synapse-specific regulation could occur within the same BC dependent upon the identity of the postsynaptic RGC type.

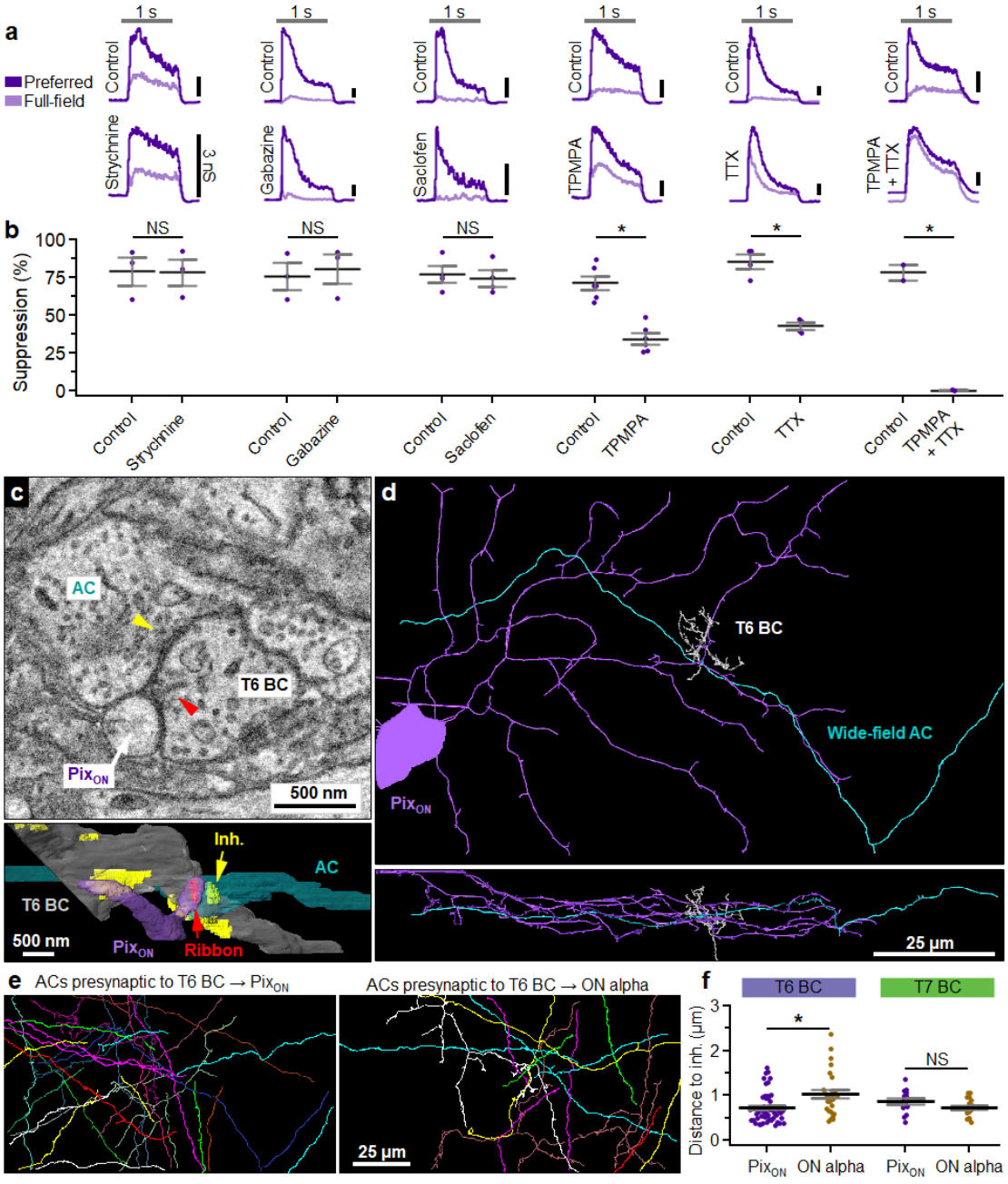

Fig. 4.5 | Wide-field amacrine cell regulation at the bipolar cell terminal contributes to stronger surround suppression in Pix_{ON} RGCs.

(**a**) Pix_{ON} excitatory conductances evoked before (top) and after (bottom) bath application of antagonists of glycine receptors (strychnine), $GABA_A$ receptors (gabazine), $GABA_B$ receptors (saclofen), $GABA_C$ receptors (TPMPA), or Na_V channels (TTX). The gray horizontal bar indicates a 1-second presentation of the stimulus. Note: conductance trace in TPMPA+TTX was shifted down 2 nS to improve visibility. (**b**) Surround suppression of excitatory conductances in control and antagonists conditions. Dots indicate data from individual cells strychnine (n=3), gabazine (n=3), saclofen (n=4), TPMPA (n=6), TTX (n=4), TPMPA+TTX (n=2). Bar plots indicate average ± s.e.m., *P<0.05, paired two-sample Student's *t*-test. (**c**) SBFSEM slice (top) and reconstruction (bottom) showing an AC neurite (cyan) forming an inhibitory synapse (yellow) onto a BC (gray) which then forms a ribbon synapse (red arrow) onto a Pix_{ON} RGC dendrite (purple). (**d**) A zoomed-out En face (top) and cross-sectional (bottom) view of the AC from **c.** (**e**) Reconstruction of nearest presynaptic ACs to T6 BC-to-Pix_{ON} (left) and T6-to-ON alpha (right) ribbon synapses. (**f**) Distance to nearest inhibitory from T6 BC output synapses (Pix_{ON} n=51, ON alpha n=26) and T7 BC output synapses (Pix_{ON} n=14, ON alpha n=17). Dots indicate data from each BC-to-RGC synapse. Bar plots indicate average ± s.e.m., *P<0.05, Welch's t-test.

Electrotonic properties of bipolar cell terminals

Since inhibitory synapses were closer to the type 6 BC-Pix_{ON} synapses than type 6 BC-ON alpha synapses (**Fig. 4.5f**) and Pix_{ON} surround suppression is dependent on ionotropic $GABA_C$ receptors (**Fig. 4.5b**), one might hypothesize that subcellular surround suppression is achieved by subcellular hyperpolarization localized to BC-Pix_{ON} output synapses. But BCs are small and so is the distance between their output synapses, bringing into doubt whether voltage could differ enough between output synapses to actually cause differing glutamate release. To investigate whether electrical compartmentalization can support functionally divergent signals from a BC, we generated a morphologically detailed NEURON cable model[69] from an SBFSEM reconstruction of a type 6 BC,

including the location of all 91 ribbon output synapses and 120 presynaptic inhibitory synapses (**Fig. 4.6a**). Although BCs are often modeled using only passive membrane properties[70–72], multiple studies have measured voltage-gated ion conductances from BCs which could lead to greater electrical compartmentalization[73–76]. Thus we performed all experiments in both a passive model and an active model containing L-type Ca^{2+} channels[77,78], K_V^+ channels[79], and HCN_2 channels[80,81] (see **Methods** for model details, **Table 4.3** for parameter values, and **Supplementary Fig. 4.9** for robustness tests).

To estimate the ability of the inhibitory sites to differentially suppress ribbon output synapses, we depolarized the BC by activating excitatory synapses on the dendrites. We then activated sets of presynaptic inhibitory synapses and measured the resulting hyperpolarization at each ribbon output synapse (**Fig. 4.6b**). When activating a single inhibitory synapse, the magnitude of the hyperpolarization varied across the 91 ribbon output synapses (**Fig. 4.6c**). To quantify this variation, we calculated the percent decrease of hyperpolarization from the top to the bottom quartile of ribbons. This measure of inhibitory voltage decay varied based on which inhibitory synapse was activated, but tended to be much larger for the active model compared to the passive model, with a median hyperpolarization decay of 29% in the active model and only 4% in the passive model. These data are plotted as a function of distance in **Supplementary Fig. 4.10** to estimate the effective electrotonic length constant of each inhibitory synapse for each model.

As it seems unlikely that the BC's inhibitory surround is actually conveyed by a single inhibitory synapse, we also performed this same experiment while simultaneously activating multiple inhibitory synapses. To assess how the simultaneous activation of multiple inhibitory synapses impacts the spread of hyperpolarization, we repeated the sequential activation of each of the 120 inhibitory synapses but also included the simultaneous activation of the n-nearest neighbors to that synapse. As more inhibitory synapses were simultaneously activated, the range of hyperpolarizations across the ribbons decreased (**Fig. 4.6c-e**) with a corresponding decrease in the inhibitory voltage decay between the top and bottom quartiles of ribbons (inhibitory decay of 1.8% for the passive model and 12% for the active model when activating all 120 inhibitory synapses, **Fig. 4.6f**).

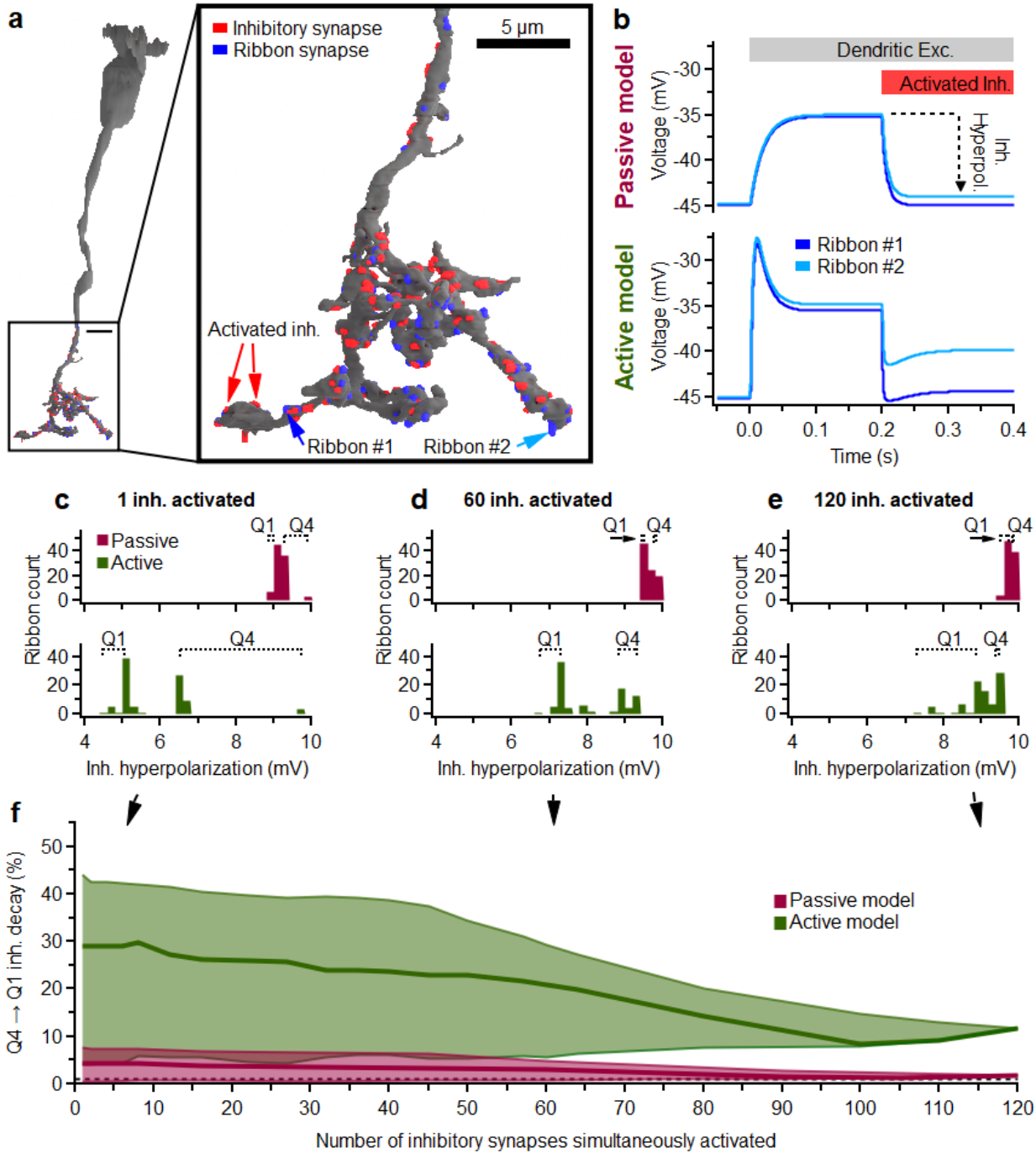
a
Inhibitory synapse
Ribbon synapse
5 µm
Activated inh.
Ribbon #1
Ribbon #2
b
Passive model
Active model
Dendritic Exc.
Activated Inh.
Inh. Hyperpol.
Voltage (mV)
Ribbon #1
Ribbon #2
Time (s)
c
1 inh. activated
d
60 inh. activated
e
120 inh. activated
Passive
Active
Q1
Q4
Ribbon count
Inh. hyperpolarization (mV)
f
Q4 → Q1 inh. decay (%)
Passive model
Active model
Number of inhibitory synapses simultaneously activated

Fig. 4.6 | Cable model of the bipolar cell terminal.

(**a**) An SBFSEM reconstruction of a type 6 BC (T6 BC), including 91 ribbon output synapses (blue) and 120 inhibitory input synapses (red). (**b**) Example voltage trace of ribbons in **a** (blue arrows) during a simulation experiment in which the BC is depolarized via excitatory currents at its dendrites (dendritic exc.) and then inhibitory synapses are activated (Activated inh., red arrows from **a**). *Top,* ribbon voltage measured in a passive model of the BC. *Bottom,* voltage measured in an active model of a T6 BC which includes voltage-gated channels (L-type Ca^{2+}, K_V^+, and HCN2). (**c**) Example histogram of inhibitory hyperpolarization of the ribbon synapses in the passive (*top*) and active (*bottom*) BC model when activating a single inhibitory synapse. Q1 and Q4 indicate the range of the top and bottom quartiles of ribbon hyperpolarization. (**d**,**e**) Same as **c** but when simultaneously activating 60 **d** or 120 **e** inhibitory synapses. (**f**) Decrement of the average inhibitory hyperpolarization of Q2 ribbons to Q1 ribbons based on the number of inhibitory synapses simultaneously activated. Thick lines indicate the median decay across all sets of inhibitory synapses activated. Shading indicates the range of inhibitory decay across all sets of activated inhibitory synapses (n=120).

We wanted to test if the compartmentalization of inhibition seen in either the passive or active model of the BC could enable the differing levels of surround suppression measured in the Pix_{ON} and ON alpha excitatory conductances. However, this requires moving beyond a model of a single BC, as an RGC receives input from many BCs across its dendritic arbor. Thus, we combined the results of the BC cable model with the previously described BC subunit model that predicts an RGC's excitatory response as the summation of BC receptive field subunits sampled across its dendritic arbor (**Supplementary Fig. 4.6a**).

If voltage decay of the BC's inhibitory surround causes the weakened surround suppression of the ON alpha's excitatory input compared to the Pix_{ON}, then the two RGCs would have to selectively sample from the pool of ribbon output synapses based on their level of inhibitory decay. Thus, we assigned the quartile of ribbons with the greatest hyperpolarization to the Pix_{ON} and the quartile of ribbons with the least

hyperpolarization to the ON alpha (**Fig. 4.7a**). This was an arbitrary assignment, and further research is needed to determine if this level of functionally specific synapse formation actually occurs.

If we additionally assume that voltage is linearly related to glutamate release, we can infer the relative center-to-surround ratio (CSR) of the Pix_{ON} and ON alpha's BC subunits from the voltage decay of inhibition at their assigned ribbons (i.e. if the BC-ON alpha ribbons experience 50% inhibitory decay compared to BC- Pix_{ON} ribbons, then the ON alpha BC subunits will have CSR values twice as large as Pix_{ON} BC subunits). We fixed the Pix_{ON} BC subunit CSR value to 1.1, as it accurately predicted surround suppression for the Pix_{ON} (**Supplementary Fig. 4.6a)**. We then determined the ON alpha BC subunit CSR from the inhibitory voltage decay at its ribbons and predicted surround suppression of the ON alpha excitatory input using the BC subunit model (**Fig. 4.7a**,**b**).

Figure 4.7c shows that in the passive BC model, none of the individual inhibitory synapses provided inhibition with enough decay to support the decreased surround suppression measured from the ON alpha excitatory conductances. However, in the active BC model, 62 of the 120 inhibitory synapses were predicted to cause a level of surround suppression equal to or less than that measured in the ON alpha. When repeating this experiment with the simultaneous activation of half of the BC's 120 inhibitory synapses, 41 of the 120 sets of 60 inhibitory synapses continued to predict a level of surround suppression equal to or less than the measured ON alpha surround suppression (**Fig. 4.7d**).

These modeling results suggest that the BC axonal arbor is not completely isopotential and that voltage gradients could feasibly contribute to localized glutamate release, particularly since a nonlinear relationship between voltage and glutamate release[82,83] could accentuate differences between ribbons. However, a voltage gradient within the BC arbor is not absolutely required for functional divergence. We speculate in the **Discussion** about chemical sources of subcellular functional divergence at small spatial scales within the BC terminal that could work in concert with the voltage gradient or independently.

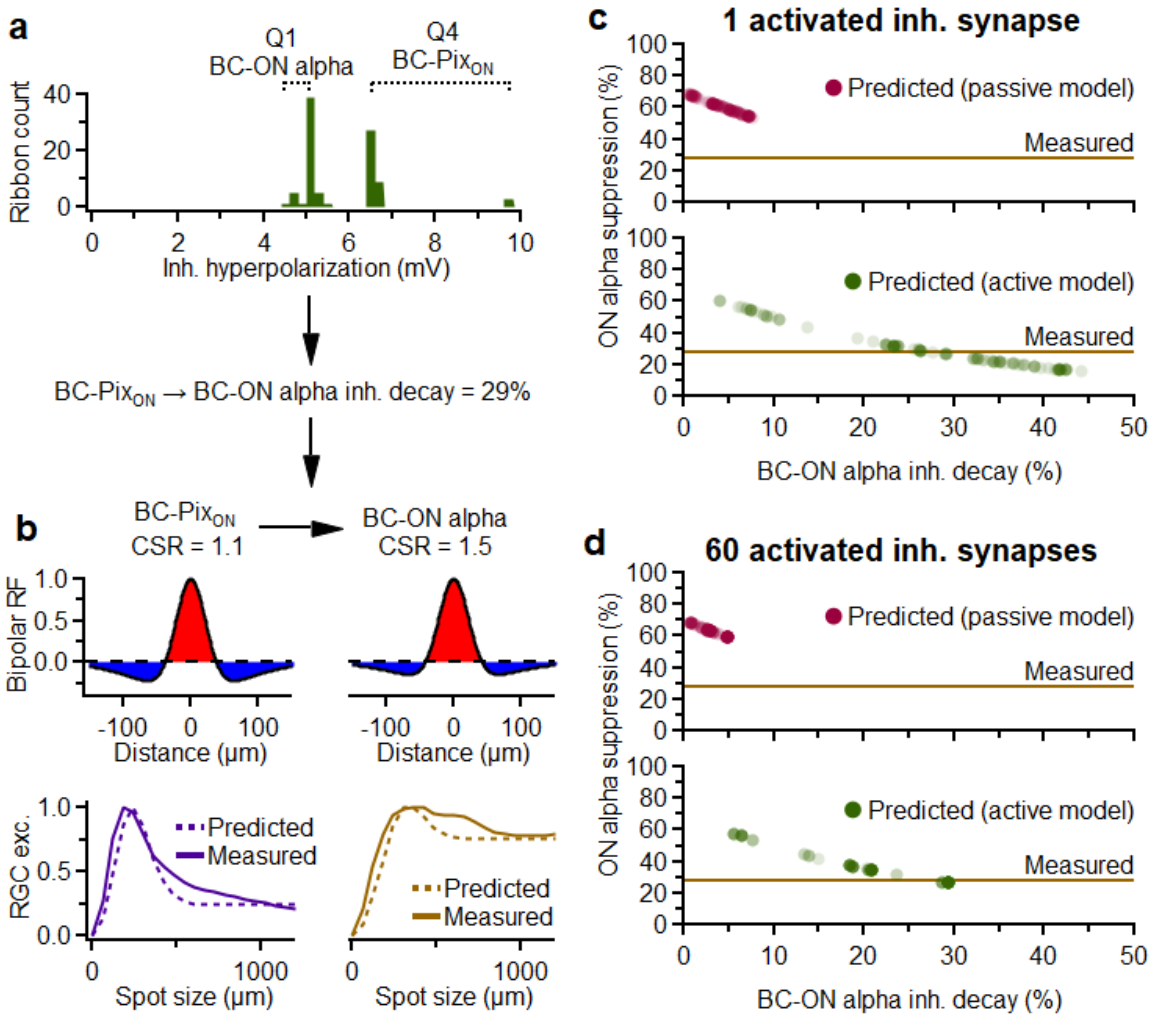
a
Q1
BC-ON alpha
Q4
BC-Pix$_{ON}$
Ribbon count
Inh. hyperpolarization (mV)
BC-Pix$_{ON}$ → BC-ON alpha inh. decay = 29%
b
BC-Pix$_{ON}$
CSR = 1.1
BC-ON alpha
CSR = 1.5
Bipolar RF
Distance (µm)
RGC exc.
Predicted
Measured
Spot size (µm)
c
1 activated inh. synapse
Predicted (passive model)
Measured
Predicted (active model)
ON alpha suppression (%)
BC-ON alpha inh. decay (%)
d
60 activated inh. synapses

Fig. 4.7 | Modeling suppression of RGC excitation through electrical isolation of inhibition on the bipolar axonal arbor.

(**a**) Example histogram of hyperpolarization experienced by the BC ribbon output synapses upon activation of an inhibitory synapse (see **Fig. 4.6**). If the top (Q4) and bottom (Q1) quartiles of ribbons are assumed to synapse on Pix_{ON} and ON alpha respectively, then inhibition of ON alpha BC input would be expected to decay by 29% compared to the Pix_{ON} for this example. (**b**) *Top*, BC center-to-surround ratio (CSR) and receptive fields predicted for Pix_{ON} and ON alpha BC subunits given a 29% inhibitory decay (assumptions described in text). *Bottom*, Resulting model predictions (dotted lines) for surround suppression of Pix_{ON} (n=14) and ON alpha (n=8) excitatory conductances according to the BC subunit model detailed in **Supplementary Fig. 4.6**. Solid lines indicate average experimentally measured excitatory responses for the same cells. (**c**) Inhibitory voltage decay predicted for each inhibitory synapse in the passive (*Top*) or active (*Bottom*) models of the T6 BC and the resulting predictions of ON alpha surround suppression. The brown line indicated experimentally measured ON alpha surround suppression (n=8). (**d**) Same as **c** but simultaneously activating sets of 60 inhibitory synapses.

Discussion

Our study identified the site of functional divergence between an RGC type with strong surround suppression (Pix_{ON}) and a type with weak suppression (ON alpha). Contrary to the prevailing view of the functional organization of the retina and the central nervous system more generally, this site of divergence was not different types of neurons but instead nearby (<20 μm) synapses within the axon terminal of the same neuron. The capacity for functional compartmentalization at such a small spatial scale requires a new framework for information processing in the excitatory pathways of the retina. These results, along with an increasing set of similar observations throughout the brain, suggest that more detailed biophysical work on the pre-synapse is required to appreciate the computational complexity of neuronal output.

Subcellular output divergence in the retina and the brain

In spiking neurons, action potentials measured at or near the soma are typically thought of as all-or-none signals that invade the full axon terminal to drive synaptic release. Compact, non-spiking neurons, like BCs, are assumed to be nearly isopotential (**Fig. 4.6**). Thus, somatic voltage is measured as the signal driving synaptic release. There is precedent, however, for both spiking and non-spiking neurons transmitting different signals at different output locations. The degree to which functional divergence occurs in axons has been highlighted as one of the most important questions in neuroscience[84].

Motor neurons in both rat[85–87] and spiny lobster[88–90] propagate spikes down some parts of the axonal arbor but not others in conditions that the authors of these studies argued were physiological. Motor neurons in locusts contain two axonal branches, each with its own axon initial segments that can initiate spikes independently. These spikes often propagate to the opposite branch but can fail to propagate in some conditions[91]. Functional divergence has also been measured in spiking sensory neurons. Leach mechanoreceptors can propagate spikes to different postsynaptic neurons and fail to propagate to others depending on which part of their receptive field is stimulated[92–97]. Auditory afferents in bush cricket can display different frequency tuning in nearby parts of the axonal arbor through a mechanism involving presynaptic inhibition[98]. Mechanisms for the functional compartmentalization of the axonal arbors of spiking neurons have included both intrinsic electrical properties[85–87,99–101] and the external influence of GABAergic interneurons[102–104].

In the retina, functional divergence has been demonstrated in several types of non-spiking ACs, including the A17 [ref. [105]], VGluT3 [ref. [106]], and starburst[107]. These ACs, however, have substantially larger neuritic arbors than BCs axons, so electrotonic isolation is greater and can better support functional divergence. Some types of BCs in the zebrafish retina have distinct lobular output boutons in different layers of the IPL, which can display different light-driven calcium signals. Differential bouton volume has been suggested as a mechanism for functional divergence in these BCs[108].

Possible mechanisms of synapse-specific surround suppression in bipolar cells.

Compartmentalization of synaptic release at the micron scale is difficult to reconcile with the canonical view that transmitter release within a neuron is controlled exclusively by presynaptic voltage, especially for a cell type typically modeled as passive and isopotential. Indeed, our modeling suggests that such a passive model of the BC would not support sufficient electrical compartmentalization for much subcellular functional divergence. However, the inclusion of active conductances decreased the membrane resistance to the point that voltage gradients could feasibly contribute to functionally divergent signals within a single BC.

This model contained many assumptions, such as the degree of functionally specific synapse formation and the linearity of the voltage-to-glutamate relationship. If these assumptions are shown to be incorrect, such as functionally indiscriminate BC-RGC synapse formation, the model would overestimate voltage-driven functional divergence. However, other inaccuracies, such as a supralinear relation between voltage and glutamate release[82,83], would cause the model to underestimate voltage-driven functional divergence. Regardless, our model highlights the importance of considering active conductances and challenges the assumption that all output synapses experience the same voltage signal.

Although our modeling suggests the possibility of voltage compartmentalization, chemical compartmentalization within the BC terminal could also contribute to functional divergence. But which molecule(s) could be localized at the micron scale to alter glutamate release? Calcium influx triggers vesicle fusion and glutamate release, and voltage-gated Ca^{2+} channels are clustered near ribbons where they can form Ca^{2+} nanodomains[109]. Strong buffering, including by the release machinery itself, and physical barriers, like the endoplasmic reticulum, the ribbon, and the hundreds of associated vesicles, could limit Ca^{2+} diffusion. Different subtypes of voltage-gated Ca^{2+} channels or associated accessory proteins that modulate their function could be localized to particular synapses, and these barriers to Ca^{2+} diffusion could endow the nanodomains with some degree of independence.

We think the most likely mechanism is that an external, diffusible chemical signal (from ACs to the BC ribbon) causes local regulation of individual synapses. Our pharmacology results showed that $GABA_C$ receptors and spiking ACs are required for surround suppression of Pix_{ON} excitation (**Fig. 4.5b**), but this does not exclude the involvement of another modulator. Perhaps GABA release from spiking ACs causes a moderate hyperpolarization of the BC, which is necessary for any level of surround suppression, but differing levels of surround suppression are achieved through the simultaneous release of an additional modulator which induces a voltage-independent reduction of Ca^{2+} at BC-Pix_{ON} synapses or a voltage-independent enhancement of Ca^{2+} at BC-ON alpha synapses.

Collectively, ACs contain at least 20 different small molecule or peptide transmitters and neuromodulators, and the differential expression of these molecules is one of the primary ways to classify them into different types[110], yet the functions of most of these molecules in visual processing remain largely unknown. Reports of voltage-independent effects of these substances on calcium levels include activation of Ca^{2+}-permeable α7 nicotinic acetylcholine receptors on type 7 BCs[111], activation of D1 dopamine receptors on rat and mouse BC terminals[112,113], leading to increased Ca^{2+} levels through PKA-dependent enhancement of L-type Ca^{2+} currents or through PIP2-dependent Ca^{2+} release from internal stores[114], and regulation of Ca^{2+} current at OFF BC terminals via S-nitrosylation from retrogradely released nitric oxide[115]. While their molecular mechanisms and possible subcellular compartmentalization were not studied, dopamine has been shown to decrease surround suppression in fish BCs[116], and both agonists and reverse agonists of cannabinoid receptors have been shown to alter the surrounds of mouse ON alpha RGCs[117].

Measuring functional divergence at the micron scale

While our interpretation is that functional divergence in BC terminals can occur at the scale of tens of microns, our functional measurements were made at the macroscopic scale of spikes and synaptic currents in RGCs. Functional imaging of calcium or glutamate with genetically encoded indicators could presumably offer more direct measurements at the micron scale. These techniques have been used for studying functional compartmentalization in retinal ACs[105,118,119], the dendrites of RGCs[120–122], and even in

a recent paper that similarly reported divergence of a different function (direction selectivity) in type 7 BCs[71].

While these imaging techniques theoretically offer better spatial resolution, they are indirect measures of synaptic function and suffer from their own technical limitations. Calcium imaging revealed functional compartmentalization in A17 ACs where synaptic boutons are separated by ~20 µm sections of a single, extremely thin (100 nm) neurite[105]. In contrast, a type 6 BC terminal has ~90 ribbon synapses all within a compact 3D structure mostly lacking anatomical compartmentalization (**Fig. 4.6a**). In addition to the ever-present issue of the nonlinear relationship between calcium changes and neurotransmitter release, the morphology of these terminals makes measurements of local calcium at the scale of individual synapses with a diffusible indicator infeasible.

Glutamate imaging enables a more direct measurement of the molecule driving postsynaptic current, but it suffers from a different kind of spatial localization problem: uncertainty about the origin of the glutamate. The sensor (iGluSnFR) is present throughout the membrane of each cell in which it is expressed. Thus, it lacks synaptic localization. Expressing iGluSnFR in RGCs could reveal postsynaptic compartmentalization, but it would not reveal whether nearby signals arose from the same or different BCs. Alternatively, expressing iGluSnFR sparsely in the BCs themselves, as was achieved for type 7 BCs via subretinal viral injections[71], does not guarantee that the measured signals arise from the BCs in which the sensor is expressed given the extremely high density of glutamatergic synapses in the IPL. Of course, any imaging technique in the functioning retina also interferes to some extent with the light responses of the photoreceptors[123]. Laser-induced light exposure is especially problematic when attempting to compare responses to small spots of light within the imaging field (the scale of one or several BCs) to large spots of light that extend beyond the imaging field.

Instead of functional imaging, we used electrophysiology to ascertain the presynaptic origin of the divergence in surround suppression between Pix_{ON} and ON alpha RGCs (**Figs. 4.1-4.3 & Supplementary Figs. 4.2-4.5**). We then used SBFSEM and confocal imaging to determine that these RGCs share input

from the same set of BCs (**Fig. 4.4 & Supplementary Fig. 4.7**). Thus, while we did not directly measure different functional signals within the terminals of a single BC, we showed that different glutamate release profiles are experienced by RGCs that collect from the same population of BCs.

Implications for visual processing in bipolar cells

A decade ago, RGC spike recordings during current injections into single salamander BCs suggested that individual BCs could, at least indirectly, transmit different functional signals to different RGCs; however, it remained unclear to what extent postsynaptic mechanisms, ACs, or gap junctions were involved[124]. These authors and others[125] have speculated about the vast computational power of a neural network in which individual connections between neurons could have some degree of functional independence. Our results demonstrate that, indeed, one of the most canonical retinal computations, surround suppression, can manifest within a neuron whose output synapses are on average less than 25 μm apart.

We focused on type 6 BCs (**Fig. 4.5e**, **Fig. 4.6**, and **Supplementary Fig. 4.7**), but type 7 BCs also provide a substantial input to Pix_{ON} and ON alpha RGCs (**Fig. 4.4h-j**), and functional divergence of direction selectivity in their terminals has been measured by glutamate release[71]. Rather than an exception, functional divergence may be the rule in mouse (and perhaps other mammalian) BCs. Importantly, one cannot necessarily measure functional divergence with a single stimulus paradigm[71]. Since the difference we measured was in the degree of surround suppression, we would not have measured it with spatially uniform stimuli or when analyzing only a single spot size at a time. This could help explain the lack of evidence for subcellular processing in a previous study of mouse BC glutamate release[60], though the same researchers did find evidence for functional divergence in BCs with improved analysis methods[126].

Functional specialization at the subcellular scale is noteworthy in the context of interpretations of ultrastructural (connectomics) datasets, where the mouse retina has been a model for linking circuit structure to function[49,127,128]. SBFSEM reconstructions allowed us to quantify BC inputs to Pix_{ON} and ON alpha RGCs (**Fig. 4.4**) and to measure details of the locations of synapses (**Figs. 4.5f, 4.6a**), but the main

conclusion of our study suggests that one should be cautious in interpreting similar patterns of synaptic connectivity as a proxy for similar function.

Methods

Ex vivo retina preparation

Mice of either sex aged 6 - 36 weeks were used for recordings and imaging. For experiments requiring labeled type 6 BCs (**Figs. 4.4-4.5** and **Supplementary Fig. 4.7**), CCK-ires-Cre/Ai14 mice were used (Jackson Lab Strain # 012706 / 007914). All other experiments used wild-type mice (C57BL/6, Jackson Lab Strain # 000664).

Whole mount retinas were prepared in a similar manner to previous publications[12,13,23,28–31]. In short, dark-adapted mice were sacrificed, and retinas were dissected under infrared illumination (940 nm). The intact retina was flat-mounted photoreceptor side down on a poly-D-lysine-coated glass coverslip and placed in a recording chamber. Retinas were perfused with oxygenated Ames medium at 32°C at a rate of 10 mL/min throughout the experiment. Animals were sacrificed following animal protocols approved by the Center for Comparative Medicine at Northwestern University.

Visual stimulation

Visual stimuli were generated with a 912 x 1140 pixel DLP projector (1.3 μm/pixel) at a 60 Hz frame rate using a blue LED (450 nm) focused on the photoreceptor outer segments. Light intensities are reported in rhodopsin isomerizations per rod per second (R*/rod/s). Visual stimuli had intensity values of 200-300 R*/rod/s and background intensity values of ~0.3 R*/rod/s unless otherwise noted (**Supplementary Figs. 4.2** and **4.5**). Each cell's receptive field center was determined by flashing horizontal and vertical bars at different locations, and all subsequent stimuli were centered on the location that elicited maximal responses. Surround suppression was probed using a pseudorandom sequence of 12 spot sizes (diameters logarithmically spaced from 30-1200 μm), each presented for 1 second.

Cell-attached and whole-cell recordings.

All recordings were obtained using a 2-channel patch-clamp amplifier (Multiclamp 700B, Molecular Devices) sampling at 10 kHz. Spike trains were recorded using glass pipettes (2–3MΩ) filled with AMES solution in cell-attached configuration. Voltage-clamp recordings were performed using glass pipettes (4–6MΩ) filled with a cesium-based intracellular solution (105 mM Cs methanesulfonate, 10 mM TEA-Cl, 20 mM HEPES, 10 mM EGTA, 2 mM QX-314, 5 mM Mg-ATP, and 0.5 mM Tris-GTP; ~277 mOsm; pH ~7.32 with CsOH). Voltage was corrected for the liquid junction potential (−8.6 mV) and the cell was clamped to the reversal potential of chloride (−60 mV) to measure excitatory conductances or the reversal potential of glutamate-induced cation currents (+20 mV) to measure inhibitory conductances. Current clamp recordings and cell fills of neurobiotin were performed using glass pipettes (4–6MΩ) filled with a potassium-based intracellular solution (125 mM K-aspartate, 10 mM KCl, 1 mM MgCl2, 10 mM HEPES, 1 mM CaCl2, 2 mM EGTA, 4 mM Mg-ATP and 0.5 mM Tris-GTP; 77 mOsm; pH ~7.15 with KOH).

Dynamic clamp recordings

Dynamic clamp hardware and software were implemented as described in Desai et al. (2017)[129]. Pix_{ON} and ON alpha excitatory and inhibitory conductances were recorded in response to 200, 600, and 1200 μm diameter spots of light. New RGCs were then patched in whole-cell current-clamp configuration, the previously recorded conductances were simulated via current injections, and the resulting spike train was recorded.

In each experiment, excitatory and inhibitory conductances were simultaneously simulated, and these excitatory and inhibitory conductances were equally scaled for each cell to best reproduce the cell's response to a real preferred spot visual stimuli.

For **Figure 4.2b-g**, the paired excitatory and inhibitory conductances were always derived from the same size spot stimuli (e.g., if simulating excitation evoked by a 200μm spot, inhibition evoked by a 200 μm spot was simultaneously simulated). The "Preferred size" response was taken as the maximal spiking response observed during the simulation of all excitatory and inhibitory conductance pairs (200 μm, 600

μm, and 1200 μm). “Full-field” responses were taken as the spiking response when simulating excitation and inhibition recorded during 1200 μm spot stimuli.

For **Figure 4.2h**,**i**, “Exc_{pref}” and “Inh_{pref}” refer to the Pix_{ON} excitatory and inhibitory conductances that were found to elicit the maximal spiking response in **Figure 4.2b,d**. Conversely, “Exc_{ff}” and “Inh_{ff}” refer to the Pix_{ON} excitatory and inhibitory conductances recorded during the presentation of a 1200 μm diameter light spot.

Pharmacology

Intrinsic light responses were measured by providing full-field light stimuli while voltage clamping at -60 mV during bath application of L-AP4, DNQX, and D-AP5 to block photoreceptor-driven light response[130]. See **Table 4.1** for a complete listing of pharmacological agents and their targets.

Physiology analysis

RGC spiking responses were measured as the average spike rate during the 1-second light stimulus. RGC conductance responses were measured as the total charge transfer during the 1-second light stimulus. The preferred size response ($R_{preferred\ size}$) was defined as the maximal response measured during the presentation of all sizes of spot stimuli (30 - 1200 μm diameter). The full-field response ($R_{full\text{-}field}$) was defined as the response recorded during the presentation of the largest stimulus spot (1200 μm diameter). Suppression was calculated as

Suppression = $1 - (R_{full\text{-}field} / R_{preferred\ size})$

Two-photon imaging

RGCs were filled with AlexaFluor 488 via a whole-cell patch pipette. Images were collected through a ×60 water immersion objective (Olympus LUMPLan FLN 60x/1.00 NA) using 980 nm two-photon laser excitation (MaiTai HP, SpectraPhysics).

Immunohistochemistry

Retinas were fixed at room temperature for 15 min in 3% paraformaldehyde (Electron Microscopy Sciences) and then blocked at room temperature for 2 hours in 3% Normal Donkey Serum (Jackson Labs) and 0.5% Triton (Sigma) in Phosphate Buffer.

Retinas were then incubated with primary antibodies for 5 days at 4°C. After washing, retinas were incubated with secondary antibodies for 2 days at 4°C. All antibodies were diluted 1:500. Retinas were then mounted on glass coverslips using Vectashield Antifade (Vector Labs).

Confocal imaging

RGCs were filled with Neurobiotin tracer (Vector Laboratories, SP-1150, ~3% w/v potassium-based internal solution) and fixed in 3% paraformaldehyde solution. After performing immunohistochemical labeling, tissues were imaged on a Nikon A1R laser scanning confocal microscope through a ×40 or ×100 oil immersion objective (Nikon Plan Apo VC ×40/×60/1.4 NA).

Quantification of RGC morphology

From both two-photon and confocal images, soma diameter was calculated by tracing an outline of the soma using ‘Freehand Selections’ and solving for diameter in FIJI. Similarly, the dendritic diameter was measured by drawing a convex polygon around the tips of the dendrites in a flattened view of the image. Average branch length, number of branches, and total dendritic length were calculated by tracing the RGC dendrites using the SNT plug-in in FIJI and its built-in analysis tools[131].

Stratification analysis was performed by measuring dendrite depth in the IPL in relation to the immunohistochemically labeled ChAT bands (Starburst amacrine dendrites). Custom MATLAB software (Nath and Schwartz, 2016) based on a published algorithm [132] were used to flatten the image prior to analysis.

M5 and M4 RGC morphological data were provided by Professor David Berson and are published in Stabio, et al.[130] and Estevez et al.[58], respectively.

Correlative Fluorescence and serial block-face scanning electron microscopy (SBFSEM)

Neighboring Pix_{ON} and ON Alpha RGCs with overlapping dendritic arbors were physiologically identified in a mouse line with fluorescently labeled type 6 BCs (CCK-ires-Cre/Ai14[63,64]). After verifying that the two ganglion cells had differing levels of surround suppression in their spiking response, both ganglion cells were filled with Alexa 488. Two-photon volume images of the RGCs overlapping dendrites and the type 6 BC axonal arbors were then acquired. The retina was fixed with 1.5% glutaraldehyde and 2.5% paraformaldehyde in 0.1M Na Cacodylate buffer for 10 minutes. The retina was washed with 0.1M Na Cacodylate buffer and transferred to 4% glutaraldehyde for 4 hours at 4° C to stiffen the tissue.
We utilized the previously published near-infrared branding technique [133] to burn fiducial markers into the retina with the two-photon laser (860 nm, ~100 mW), allowing for the alignment of two-photon images with electron microscopy volumes. The tissue was prepared for SBEM according to the protocol described previously [134]. Image stacks were acquired using a VolumeScope SEM (Apreo, Thermo Fisher Scientific) at a voxel size of 5 x 5 x 50 nm^3.

Volume reconstruction and Image analysis

SBFSEM image stacks were aligned and registered using ImageJ/TrakEM2[135]. The neuronal processes were traced and segmented using AreaTree or AreaList function, whereas synapses were segmented using AreaList function in TrakEM2. The 3D objects of either traced skeletons or surface segmentations were visualized in either 3D view in ImageJ or exported to and rendered in Amira (Thermo Fisher Scientific).

The somata of both Pix_{ON} and ON alpha RGCs were located according to the fiducial markers. We traced the dendritic arbors of both RGCs within the limit of the SBFSEM volume. BC synapses were identified by the presence of a presynaptic ribbon apposed to the postsynaptic dendrites of both RGCs. Presynaptic amacrine cell contacts were identified by the presence of clusters of synaptic vesicles apposed to BC

axonal terminals. Presynaptic BCs were reconstructed, and their type was determined according to their stereotyped morphology[136–138]. Type 6 BCs were further confirmed by the presence of the fluorescence marker in the corresponding 2-photon volume.

We identified all the presynaptic (amacrine) inhibitory sites on the BC bouton where the ribbon synapses resided. For each ribbon, the Euclidean distances between the ribbon and all the presynaptic inhibitory sites were measured, and the inhibitory synapse with the shortest distance was identified.

Bipolar cell summation over RGC dendrites model

We modeled RGC excitation across spot sizes as the summation of BC subunits sampled across the RGC's dendritic arbor. To do this, a skeleton of the RGCs dendritic arbor was provided to the model, and excitatory input synapses were randomly assigned along the length of the dendritic skeleton (0.3 μm / synapse[139,140]). At each of these synapses, a BC was assigned, and its receptive field was centered on that synapse.

RGC excitatory responses across spot sizes were predicted by presenting virtual spots of multiple sizes centered at the centroid of the ganglion cell dendritic field and calculating each BC's activation as the overlap of its receptive field with the presented spot. RGC excitatory conductances were then modeled as the linear sum of each BC's activation. Both experimentally measured and model-predicted excitatory responses were normalized across spot sizes by the maximal response.

The BC receptive field was modeled as a circular difference of gaussians[141] with 3 parameters; center size (σ_c), surround size (σ_s), and center-to-surround ratio (CSR). While σ_c was fixed at 22 μm [ref. [140]], σ_s and CSR were obtained by minimizing the mean absolute error between the model output and the experimentally recorded RGC excitatory responses across all spot sizes. Error was minimized using the Interior-point optimization algorithm, and initial values of 100 μm for σ_s and 1 for CSR. 6 RGCs were simultaneously fit for each estimation of σ_s and CSR. Cross-validation was performed on the remaining RGCs. When fitting to both Pix_{ON} and ON alpha RGCs, 3 Pix_{ON} and ON alpha RGCs were used for fitting.

Four hundred random fitting combinations of the 14 Pix_{ON} and 8 ON alpha RGCs were performed to obtain average cross-validation values.

The model was written using MATLAB 2022a. Code and data are available at https://github.com/davidswygart/rgc_bipolar_dog.

NEURON compartment model of type 6 bipolar cell

Modeling was performed using Python 3.8 and NEURON 8.0 [ref. [69]]. SBFSEM reconstructions were imported to NEURON using NEURON's *Import3d* tool. To simulate light-evoked activation, the axon terminals were depolarized to ~-35 mV by activating synapses on its dendrites (0 mV reversal potential[82]). Each inhibitory synapse (reversal potential = -60 mV) was then activated with enough conductance to hyperpolarize the membrane to -45 mV the location of the activated inhibitory synapse[82,142]. When measuring the effect of a single inhibitory synapse (**Fig. 4.6c** & **4.7c**), hyperpolarization was measured for all 91 ribbon output synapses in response to the activation of each of the 120 inhibitory synapses (a new simulation was performed for each inhibitory synapse). When testing the simultaneous activation of inhibitory synapses (**Fig. 4.6d-f** & **Fig. 4.7d**), the same 120 inhibitory synapses were sequentially activated, but the additional N number of nearest inhibitory synapses (by path distance) were also simultaneously activated.

Inhibition-induced hyperpolarization was measured for each ribbon as the change in membrane potential caused by activation of the inhibitory synapses. All measurements were acquired after the membrane had reached a steady-state (200 ms). To calculate Q4→Q1 inh. decay, ribbons were sorted by the magnitude of their hyperpolarization. The 91 ribbons were then split into quartiles (23 ribbons in each quartile), and the average hyperpolarization was calculated for the top (Q4) and bottom (Q1) quartiles. Inhibitory decay was then calculated as 100% - Q1 / Q4.

Key model parameters can be found in **Table 4.3**. Model stability was tested by measuring inhibitory voltage decay across a range of key model parameters (**Supplementary Fig. 4.9**). Whenever model

parameters were altered, excitatory and inhibitory conductances were adjusted to maintain the same membrane potentials at the inhibitory synapse (-35 mV → -45 mV).

To better enable comparisons of our model to previous literature, we fit length constants for each inhibitory synapse (**Supplementary Fig. 4.9**). To do this, hyperpolarization was measured at the activated inhibitory synapse (ΔV_{inh}) and at each ribbon output synapse (ΔV_{rib}). The length constant (λ) for each inhibitory synapse was estimated by fitting

$$\Delta V_{rib} / \Delta V_{inh} = e^{-x/\lambda}$$

where x was the path distance between each ribbon and the activated inhibitory synapse.

Supplementary Fig. 4.9 shows that the median length constant of the inhibitory synapses in our passive BC model was 616 ± 138 µm (± median absolute deviation), which is similar to values estimated in previously published passive models of rod BCs[70] and type 7 ON cone BCs[71]. In our active BC model that contained L-type Ca^{2+} channels[77,78], K_V^+ channels[79], and HCN_2 channels[80,81], the median length constant of the inhibitory synapses was 82 ± 13 µm (median ± median absolute deviation).

Code and data are available at,

https://github.com/davidswygart/T6_NEURON_python

Statistical tests

Statistics and data representation are reported in figure legends. In short, data are reported as mean ± SEM. Differing means were assessed with Welch's t-test for unpaired data, paired two-sample Student's t-test for paired data, and two-way ANOVA for multivariate data. Comparisons of proportions were assessed with a two-proportions z-test with Holm-Bonferroni correction. Differing continuous distributions were assessed with Kolmogorov–Smirnov tests.

Table 4.1 | Pharmacological agents.

Pharmacological agent	Target	Concentration	Vendor
Tetrodotoxin (TTX)	Inhibitor of voltage-gated sodium channels[143]	500 nM	Tocris #1078
Gabazine (SR-95531)	$GABA_A$ receptor antagonist[144]	10 μM	Sigma #S106
TPMPA ((1,2,5,6-Tetrahydropyridin-4-yl)methylphosphinic acid)	$GABA_C$ receptor antagonist[145]	50 μM	Tocris #1040
Saclofen (3-Amino-2-(4-chlorophenyl)-2-hydroxypropanesulfonic acid)	$GABA_B$ receptor antagonist[146]	100 μM	Sigma #S116
Strychnine Hydrochloride	glycine receptor antagonis[147]	1 μM	Sigma #S8753
Kynurenic acid (4-Hydroxyquinoline-2-carboxylic acid)	Weak AMPA, kainate, and NMDA receptor antagonist[148]	700 nM	Sigma #K3375
NBQX (2,3-dioxo-6-nitro-7-sulfamoyl-benzo[f]quinoxaline)	Strong AMPA and kainate receptor antagonist[149]	300 nM	Tocris #1044

L-AP4 (L-(+)-2-Amino-4-phosphonobutyric acid)	group III mGluR agonist[150]	100 μM	Tocris #0103
DNQX (6,7-Dinitroquinoxaline-2,3-dione disodium salt)	non-NMDA iGluR antagonist[151]	40 μM	Tocris #2312
D-AP5 (D-(-)-2-Amino-5-phosphonopentanoic acid)	NMDA receptor antagonist[152]	30 μM	Tocris #0106

Table 4.2 | Antibodies used in immunohistochemical labeling.

Primary antibody		**Secondary antibody**	
Name	**Vendor**	**Name**	**Vendor**
Rabbit anti-PSD95	Cell Signaling #3450	Donkey anti-rabbit Alexa Fluor 647	Jackson Immuno #711-605-152
Goat anti-ChAT	Millipore #AB144P	Donkey anti-goat Alexa Fluor 647	Life Technologies #A21447
Mouse anti-SMI-32	BioLegend #801702	Donkey anti-mouse Alexa Fluor 647	Life Technologies #A31571
		Streptavidin 488	Thermo Science #21832

.

Table 4.3 | Key parameters of type 6 BC NEURON model.

Experimental parameters	Time step	25 μs
	Temperature	32°
Passive properties	Membrane capacitance	11.8 fF/μm^2 [ref. [70]]
	Cytoplasmic resistivity	13.2 mOhm-μm [ref. [70]]
	Leak conductance	3.9 pS/μm^2 [ref. [70]]
	Leak reversal potential	-60 mV [ref. [70]]
Excitation at dendrites (8 synapses)	Reversal potential	10.1 mV [ref. [153]]
	Total conductance (passive model)	334 pS [ref. [82,154]]
	Total conductance (active model)	2,600 pS [ref. [82,154]]
Inhibition at axon terminals	Reversal potential	−50.4 mV [ref. [155]]
	Conductance (passive model)	1,530 pS [ref. [156]]
	Conductance (active model)	8,000 pS [ref. [156]]
HCN2 channel (restricted to axonal arbor) [ref. [157]]	reversal potential	-23.4 mV [158]
	max conductance	0.78 pS/μm^2 [ref. [80,81]]
	Half-max of activation	-99 mV [ref. [159]]

	Slope of activation	-6.2 mV [ref. [159]]
K_V^+ channel [ref. [160]]	K^+ reversal potential	-84 mV
	Max conductance	12 pS/μm^2 [ref. [79]]
	Half-max of activation	-9 mV [ref. [161]]
	Slope of activation	14 mV [ref. [161]]
	Half-max of inactivation	8 mV [ref. [161]]
	Slope of inactivation	-9 mV [ref. [161]]
L-type Ca^{2+} channels (restricted to axonal arbor) [ref. [162]]	Ca^{2+} reversal potential	18 mV [ref. [78]]
	L-type Ca^{2+} max conductance	1.6 pS/μm^2 [ref. [78]]
	L-type Ca^{2+} half-max activation	-32 mV [ref. [78]]
	L-type Ca^{2+} slope of activation	10 mV [ref. [78]]
	L-type Ca^{2+} half-max inactivation	10 mV [ref. [78]]
	L-type Ca^{2+} slope of inactivation	-12 mV [ref. [78]]

Supplementary Figures

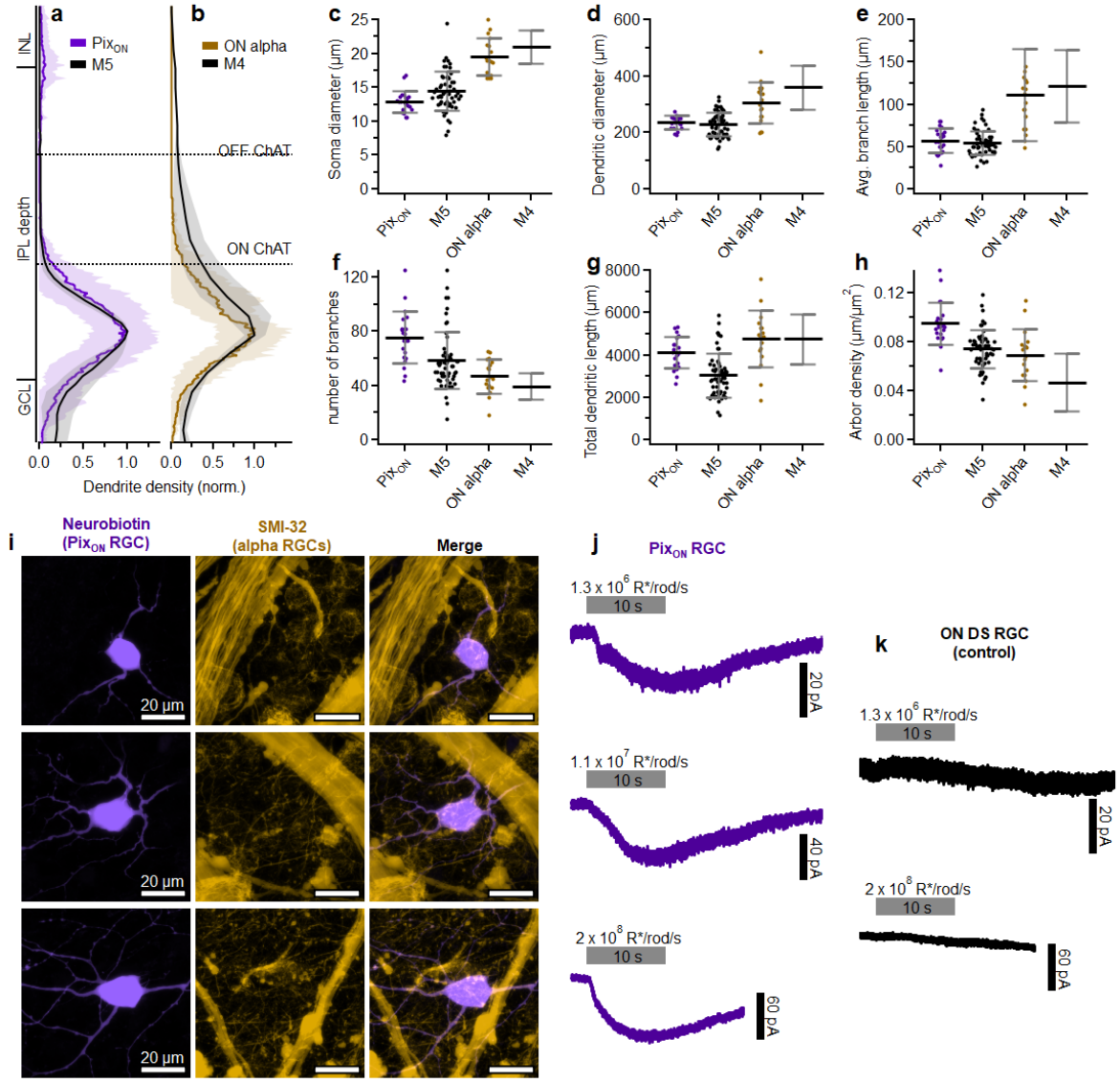

Supplementary Fig. 4.1 | Pix_{ON} and ON alpha RGCs exhibit unique morphology and correspond to M5 and M4 RGCs.

(**a**) Dendritic stratification of Pix_{ON} (n=19) and M5 (n=2) RGCs within the inner nuclear layer (INL), inner plexiform layer (IPL), and ganglion cell layer (GCL). Dotted lines refer to the ON and OFF choline acetyltransferase (ChAT) bands used to determine stratification. Shading and error bars indicate ± standard deviation. (**b**) Same as **a**, but comparing ON alpha (n=10) and M4 (n=2) dendritic stratification. (**c**-**h**) Comparison of soma diameter (**c**), dendritic diameter (**d**), average dendritic branch length (**e**), total number of dendritic branches (**f**), total dendritic length (**g**), and arbor density (**h**) between Pix_{ON} (n=22), M5 (n=56), ON alpha (n=18), and M4 (n=27) RGC types. Arbor density (**h**) was calculated as the total dendritic length normalized by dendritic area. Dots indicate data from individual cells. Bar plots indicate average ± std. (**a-h**) M5 and M4 RGC morphological data were provided by Professor David Berson and are published in Stabio, et al. (2018) and Estevez et al. (2012), respectively. (**i**) *En-face* view of three different Pix_{ON} RGC somas visualized by neurobiotin fill (left), SMI-32 staining to mark alpha RGCs (middle), and merged images. (**j**) Intrinsic photocurrents measured by voltage-clamp recordings (V_{CMD} = -60 mV) during pharmacological blockade of retinal synapses (L-AP4, DNQX, and D-AP5). Gray bars indicate 10-second full-field light step. Light intensity is reported in rhodopsin isomerizations per rod per second (R*/rod/s). Currents were measured from the same cells as in **i**. (**k**) Same as **j**, but recorded from ON direction-selective RGCs, which are not expected to exhibit intrinsic photocurrents.

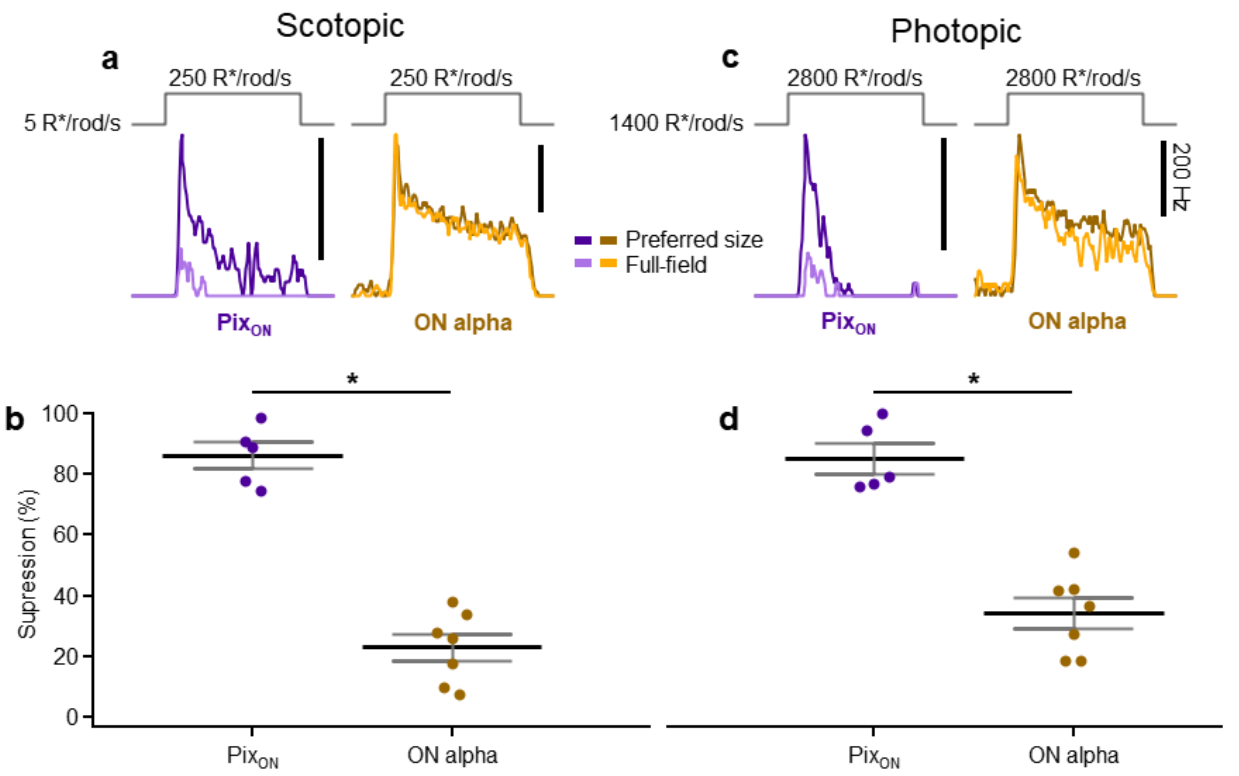

Supplementary Fig. 4.2 | Pix$_{ON}$ and ON alpha RGCs have differing levels of surround suppression in both scotopic and photopic conditions.

(**a**) Example Pix$_{ON}$ (purple) and ON alpha (brown) peristimulus time histograms to preferred size and full-field light spot stimuli. The stimulus occurred within the scotopic luminance regime, stepping to a light intensity of 250 rhodopsin isomerizations per rod per second (R*/rod/s) from a background intensity of ~0.3 R*/rod/s for 1 second. (**b**) Surround suppression in Pix$_{ON}$ (n=5) and ON alpha (n=7) RGCs to scotopic stimuli. Dots indicate data from individual cells. Bar plots indicate average ± s.e.m., *P<0.05, paired two-sample Student's *t*-test. (**c**) Same as **a**, but the stimulus occurred within the photopic luminance regime, stepping from 1400 to 2800 R*/rod/s for 1 second. (**d**) Surround suppression to photopic stimuli for the same cells as in **b**.

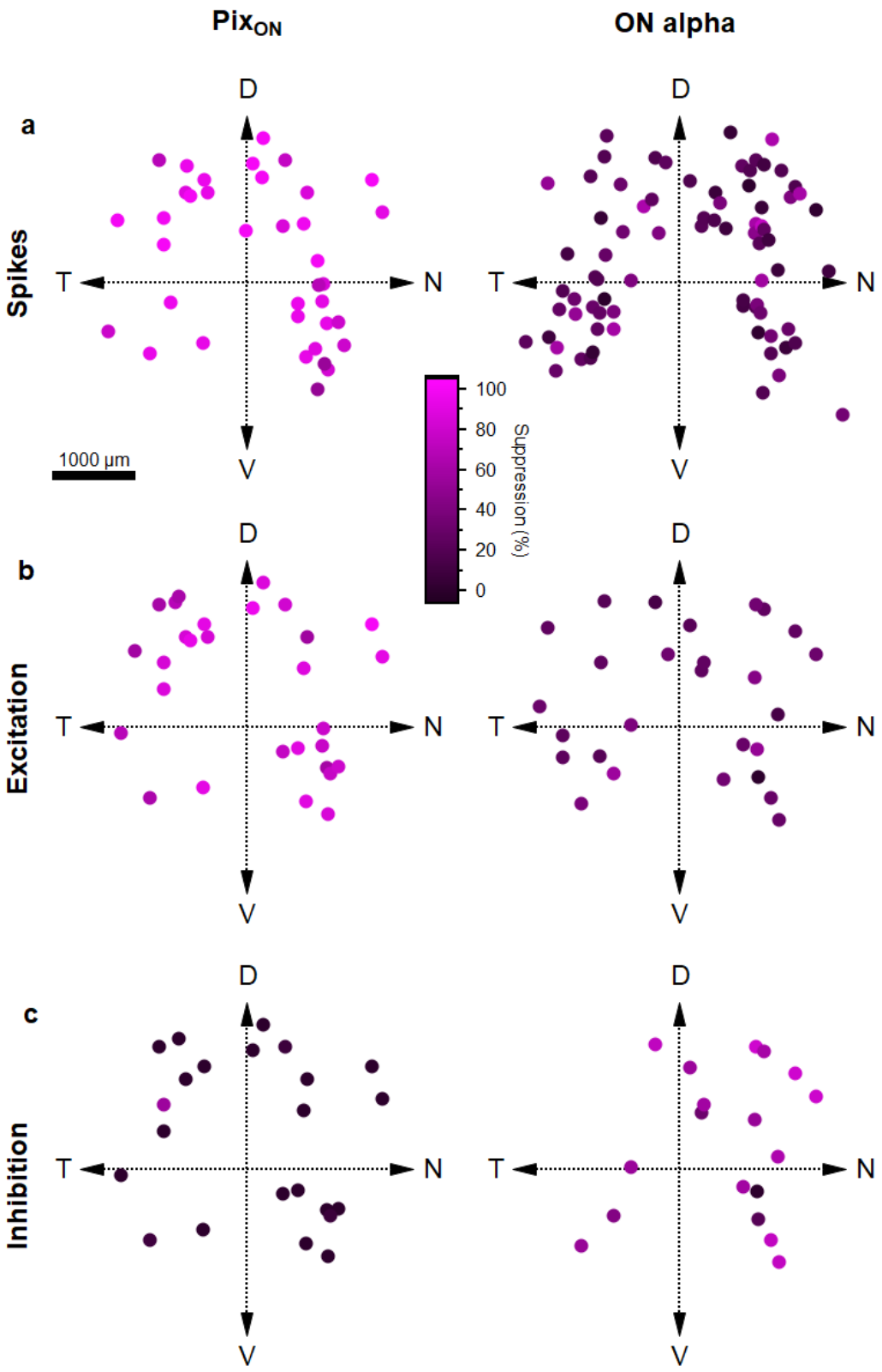
Pix$_{ON}$
ON alpha
a
b
c
Spikes
Excitation
Inhibition
D
V
T
N
1000 µm
100
80
60
40
20
0
Suppression (%)

Supplementary Fig. 4.3 | Pix_{ON} RGCs have stronger surround suppression than ON alpha RGCs across retinal locations.

(**a**) Surround suppression of Pix_{ON} (left) and ON alpha (right) spiking responses plotted by retinal location. Dots indicate the location of individual cells plotted on a dorsal (D) / ventral (V) / temporal (T) / nasal (N) coordinate scheme of the retina. Pix_{ON} (n=38), ON alpha (n=79). (**b**) Same as **a**, but for surround suppression of excitatory conductances. Pix_{ON} (n=30), ON alpha (n=27). (**c**) Same as **a**, but for surround suppression of inhibitory conductances. Pix_{ON} (n=24), ON alpha (n=18).

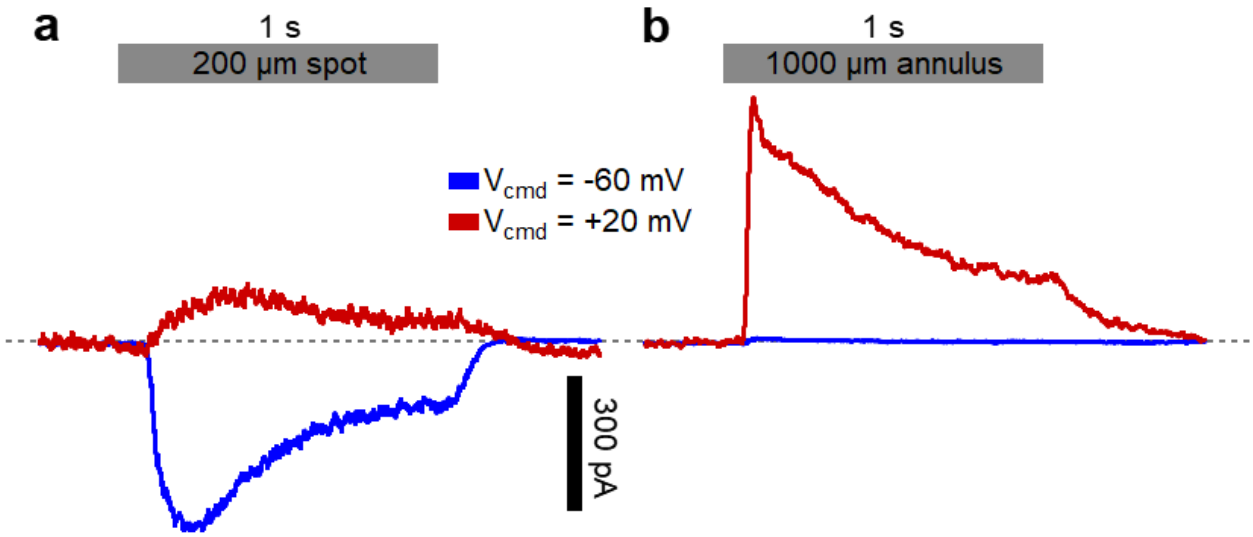

Supplementary Fig. 4.4 | Verification of voltage-clamp isolation of excitatory and inhibitory currents in a Pix_{ON} RGC.

(**a**) Synaptic currents evoked by a 1-second light step of a 200 µm diameter spot while voltage clamping at -60 mV (blue) or +20 mV (red). This stimulus primarily activated the RGC's receptive-field center, which has strong excitatory input and weak inhibitory input. (**b**) Same as **a**, but the visual stimulus was an annulus with an inner diameter of 1000 µm and an outer diameter of 1200 µm. This stimulus primarily activated the RGC's receptive-field surround, which has weak excitatory input and strong inhibitory input.

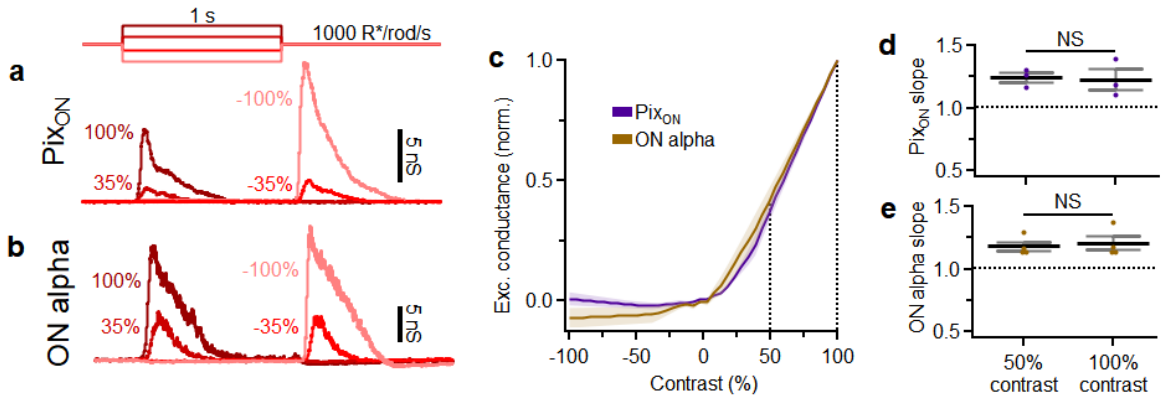

Supplementary Fig. 4.5 | Pix$_{ON}$ and ON alpha RGCs exhibit similar contrast response functions in their excitatory conductances.

(**a**) Example Pix$_{ON}$ excitatory conductances evoked by stimulation of positive and negative contrast steps from a background illumination of 1000 rhodopsin isomerizations per rod per second (R*/rod/s). (**b**) Same as **a**, but recorded from an ON alpha RGC. (**c**) Excitatory responses measured across a range of contrast steps for Pix$_{ON}$ (n=3) and ON alpha (n=3) RGCs. (**d**) Equal slopes of the Pix$_{ON}$ contrast response (from **c**) indicate that the Pix$_{ON}$ excitatory responses have not begun saturating at 100% contrast compared to 50% contrast. (**e**) Same as **d**, but for ON alpha RGCs. Dots indicate data from individual cells. Bar plots indicate average ± s.e.m., NS P>0.05, paired two-sample Student's *t*-test.

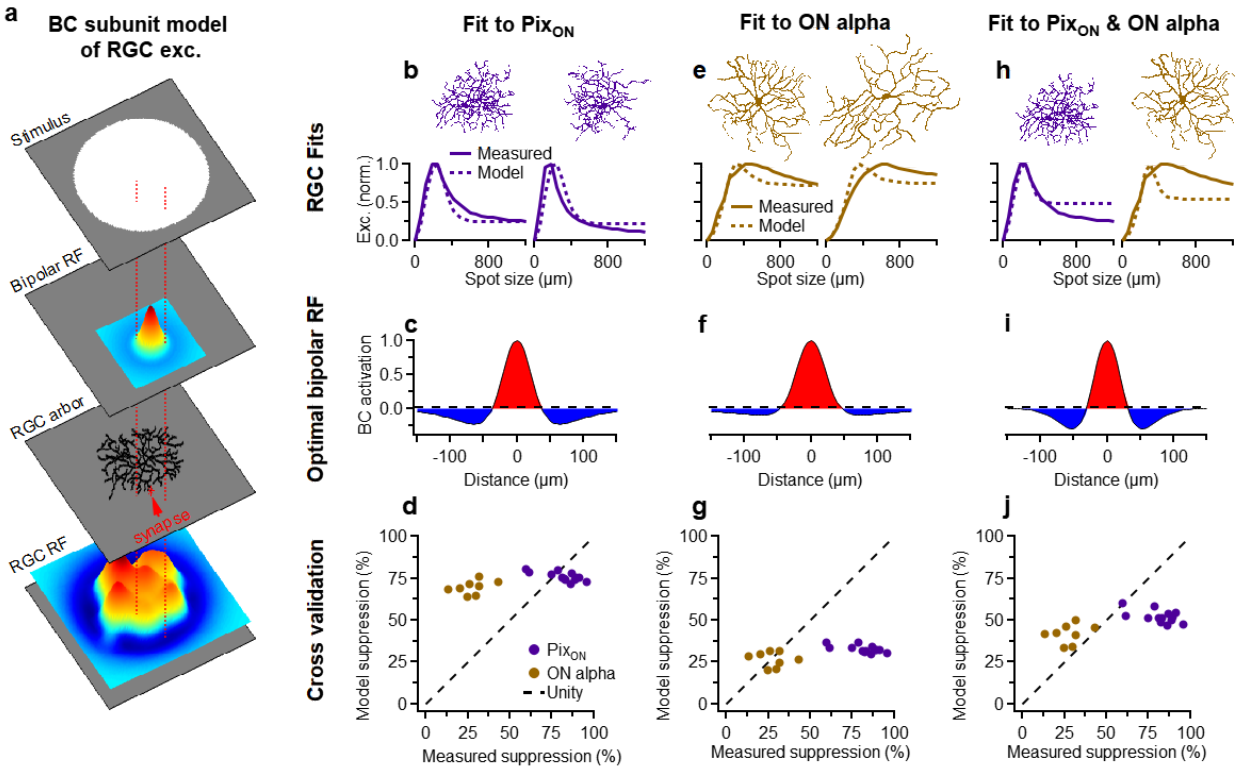
a
BC subunit model of RGC exc.
Stimulus
Bipolar RF
RGC arbor
RGC RF
synapse
Fit to Pix$_{ON}$
Fit to ON alpha
Fit to Pix$_{ON}$ & ON alpha
RGC Fits
Optimal bipolar RF
Cross validation
b
e
h
c
f
i
d
g
j
Measured
Model
Exc. (norm.)
Spot size (µm)
BC activation
Distance (µm)
Model suppression (%)
Measured suppression (%)
Pix$_{ON}$
ON alpha
Unity

Supplementary Fig. 4.6 | A bipolar subunit model of RGC excitation suggests differing bipolar receptive fields are necessary to evoke the differing level of surround suppression observed. (**a**) Schematic illustrating the BC subunit model of RGC excitation. The RGC receptive field (RGC RF) is constructed from BC receptive fields (Bipolar RF) randomly sampled across its dendritic arbor. RGC excitation is modeled as the overlap of the RGC receptive field with a virtual stimulus. (**b**) Two example Pix_{ON} dendritic arbors (*top*) and their corresponding excitatory conductances (*bottom*, solid line) used to fit the BC RF in **c**. Fitting was performed simultaneously on 6 Pix_{ON} RGCs. Dotted lines indicate the model-predicted excitatory responses across spot sizes when using the BC RF in **c**. (**c**) The BC receptive field that minimized the absolute error between measured and model-predicted excitatory responses from **a** (see methods for details). (**d**) Experimentally measured surround suppression from Pix_{ON} (n=14) and ON alpha (n=8) RGCs plotted against the average surround suppression predicted by the model when cross-validating against Pix_{ON} and ON alpha RGCs not used for fitting the BC RF. Note: alignment to unity indicates perfectly accurate model prediction. (**e-g**) same as **b**-**d**, but fitting to 6 ON alpha RGCs. (**h-j**) same as **b**-**d**, but simultaneously fitting to 3 Pix_{ON} RGCs and 3 ON alpha RGCs.

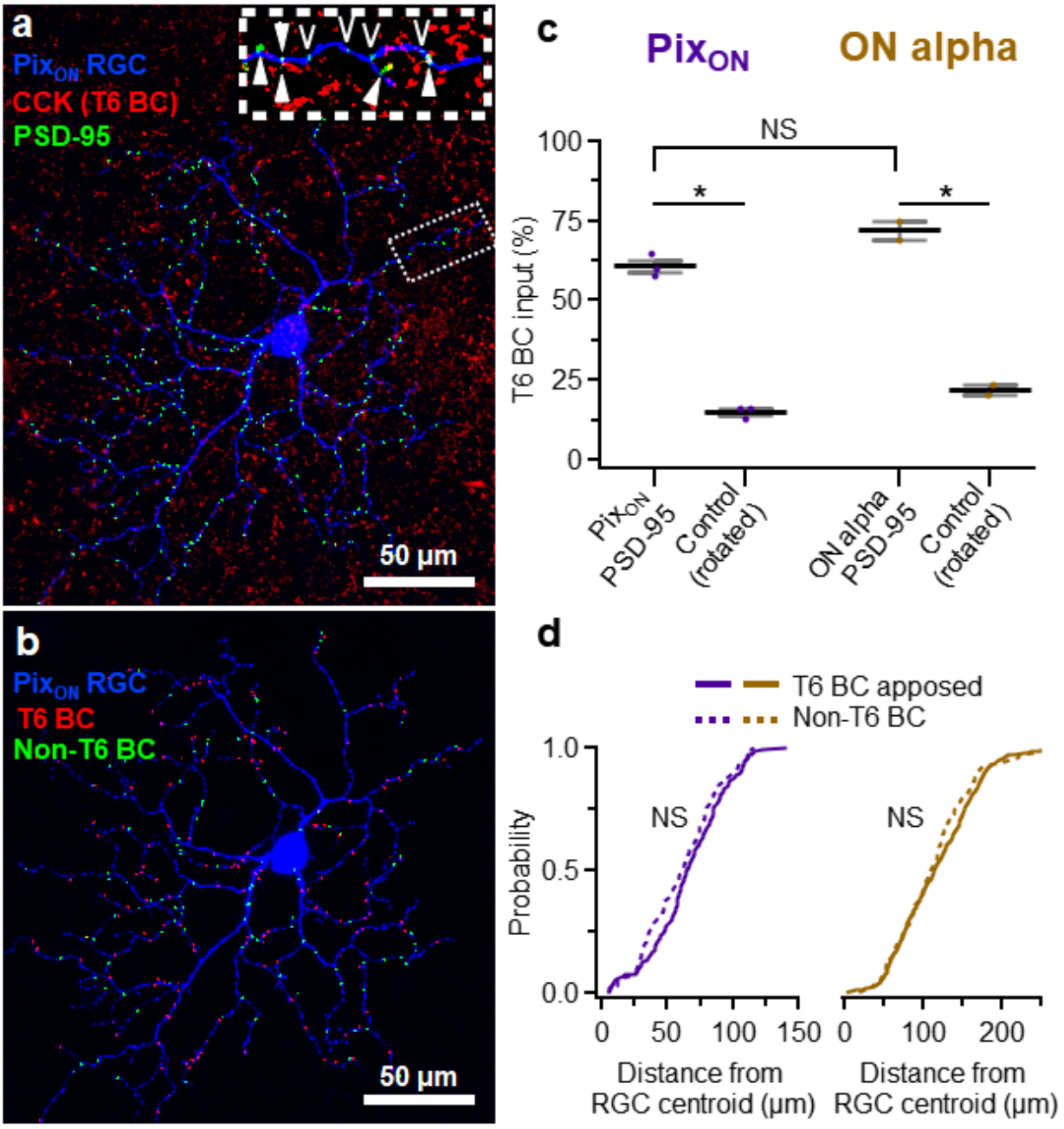
a
Pix$_{ON}$ RGC
CCK (T6 BC)
PSD-95
50 µm
b
Pix$_{ON}$ RGC
T6 BC
Non-T6 BC
50 µm
c
Pix$_{ON}$
ON alpha
NS
*
*
T6 BC input (%)
100
75
50
25
0
Pix$_{ON}$ PSD-95
Control (rotated)
ON alpha PSD-95
Control (rotated)
d
T6 BC apposed
Non-T6 BC
Probability
1.0
0.5
0.0
NS
NS
0
50
100
150
0
100
200
Distance from RGC centroid (µm)
Distance from RGC centroid (µm)

Supplementary Fig. 4.7 | PSD95 puncta apposed to type 6 bipolar cell terminals throughout the dendritic arbors of Pix_{ON} and ON alpha RGCs.

(**a**) *En-face* view of a neurobiotin-filled Pix_{ON} RGC (blue) in the CCK-ires-Cre/Ai14 mouse line which labels type 6 BCs (T6 BC, red). Postsynaptic density protein 95 (PSD95, green) is immunohistochemically labeled to identify excitatory synapses on the RGC dendrite. Inset shows a zoomed-in view of the Pix_{ON} dendrite in which some PSD95 puncta are apposed to a T6 BC axon terminal (white closed arrow), while other PSD95 puncta are not apposed to a T6 BC axon terminal (white open arrow). (**b**) Same Pix_{ON} RGC as in **a**, but all PSD95 puncta have been identified as apposed (red) or not-apposed (green) to a T6 BC terminal. (**c**) Percentage of PSD95 puncta apposed to a T6 BC within the Pix_{ON} (n=3) and ON alpha (n=2) RGCs dendritic arbor. To estimate the chance probability of PSD95 puncta overlapping with T6 BC terminals, we performed a control analysis in which the PSD95 puncta image channel was rotated 90° compared to the T6 BC image channel. *P<0.05, Welch's t-test was used for comparison of Pix_{ON} to ON alpha. Paired two-sample Student's *t*-test was used to compare the experimental group to a rotated control. (**d**) Cumulative probability of distances between PSD95 puncta and the centroid of the RGC dendritic arbor, plotted for both T6 BC apposed and non-T6 BC apposed PSD95 puncta. Differing distributions of these distances would indicate that the proportion of T6 BC apposed and non-T6 BC apposed PSD95 vary by dendritic eccentricity. These distributions were not found to differ significantly for either Pix_{ON} (T6 n=163, non-T6 n=110) or ON alpha RGCs (T6 n=461, non-T6 n=157). P>.05, Kolmogorov–Smirnov test.

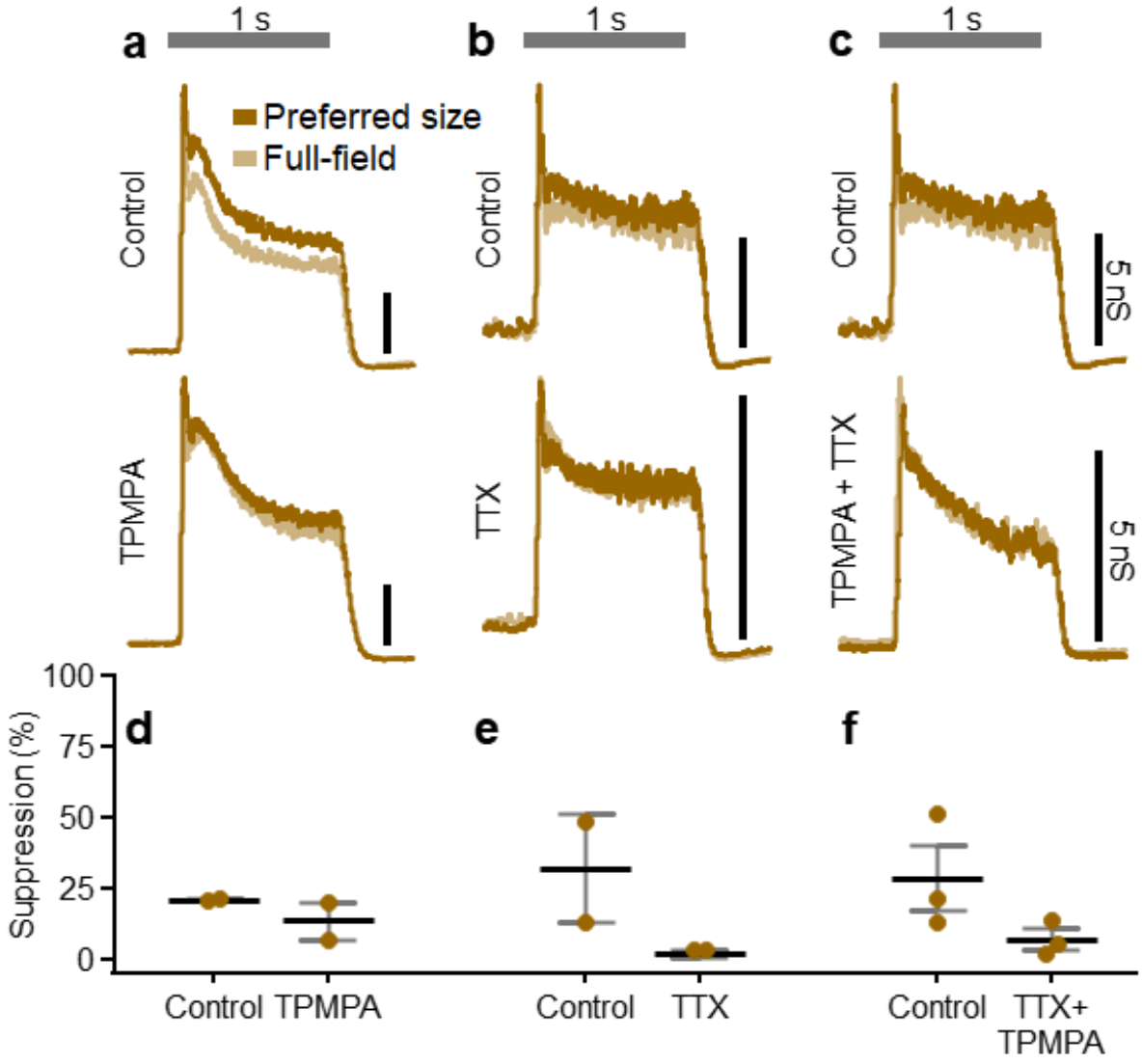
a
1 s
Preferred size
Full-field
Control
TPMPA
b
1 s
Control
TTX
c
1 s
Control
TPMPA + TTX
5 ns
5 ns
d
e
f
Suppression (%)
100
75
50
25
0
Control
TPMPA
Control
TTX
Control
TTX+
TPMPA

Supplementary Fig. 4.8 | ON alpha surround suppression of excitation remains weak in pharmacological block of $GABA_C$ receptors and Na_V channels.

(a) ON alpha excitatory conductances evoked before (top) and after (bottom) bath application of the $GABA_C$ receptors antagonist TPMPA. The gray horizontal bar indicates a 1-second presentation of either the preferred size (dark brown) or full-field (light brown) spot stimuli. (**b**) Same as **a**, but during bath application of the Na_V channel blocker TTX. (**c**) Same as **a,** but during dual application of TPMPA and TTX. (**d**) Surround suppression of ON alpha excitatory conductances in control conditions and during bath application of TPMPA (n=3). (**e**) Same as **d**, but during bath application of TTX (n=2). (**f**) Same as **d**, but during dual application of TPMPA and TTX (n=3). **d-f**, Dots indicate data from individual cells. Bar plots indicate average ± s.e.m.

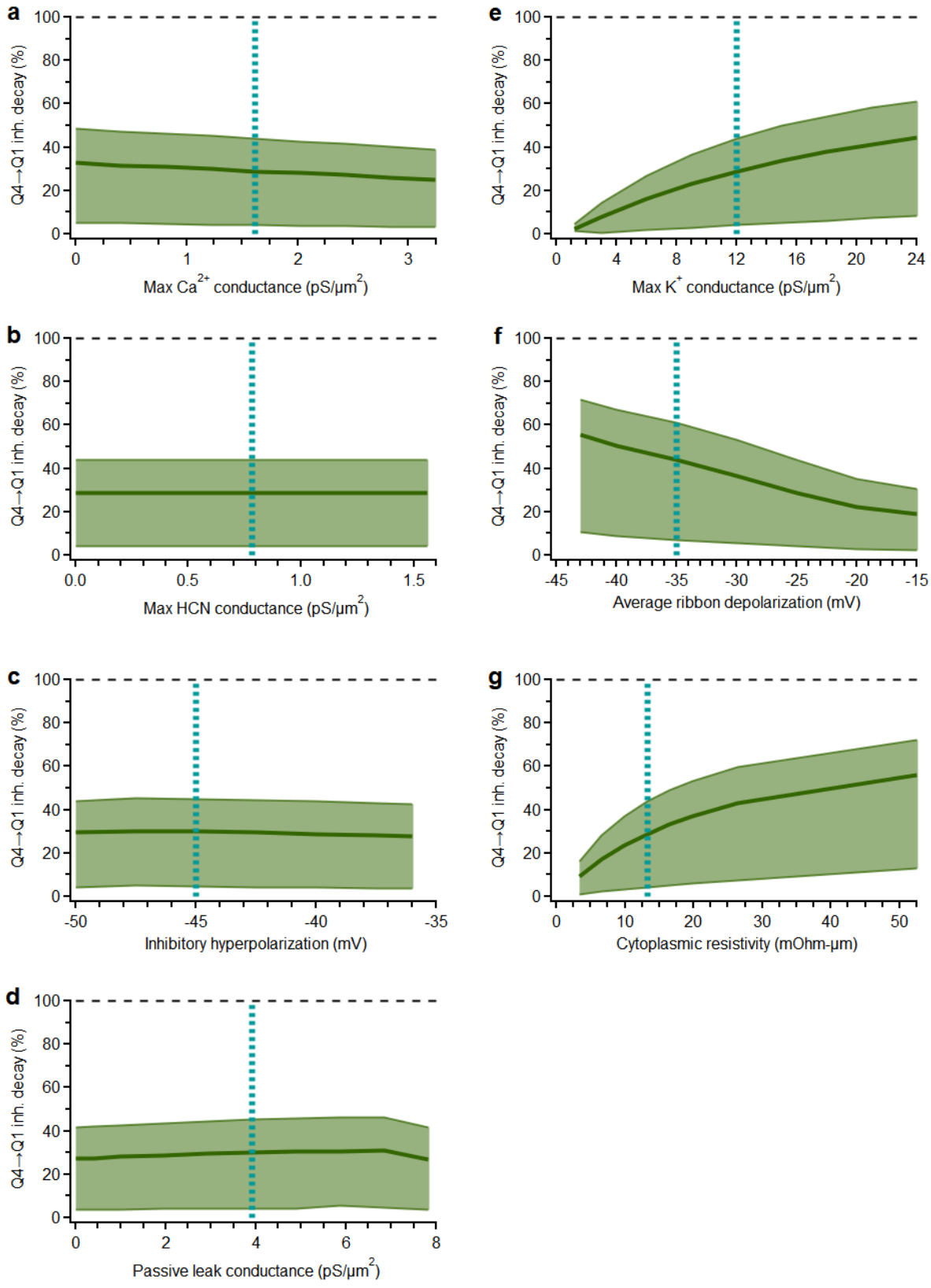
a
Q4→Q1 inh. decay (%)
Max Ca2+ conductance (pS/µm2)
b
Max HCN conductance (pS/µm2)
c
Inhibitory hyperpolarization (mV)
d
Passive leak conductance (pS/µm2)
e
Max K+ conductance (pS/µm2)
f
Average ribbon depolarization (mV)
g
Cytoplasmic resistivity (mOhm-µm)

Supplementary Fig. 4.9 | Cable model consistency over a range of parameter values.

(**a-d**) Percent decrease of hyperpolarization from the top to the bottom quartile of ribbons when activating a single inhibitory synapse plotted against a range of parameter values (see **Fig. 4.6**). Thick lines indicate the median decay across all sets of inhibitory synapses activated. Shading indicates the range (maximum to minimum) of inhibitory decay across all 120 inhibitory synapses. The vertical dotted line indicates the normal parameter value used in all other simulations (Ca^{2+}, K_V^+, and HCN_2 conductances are only applicable for the active model).

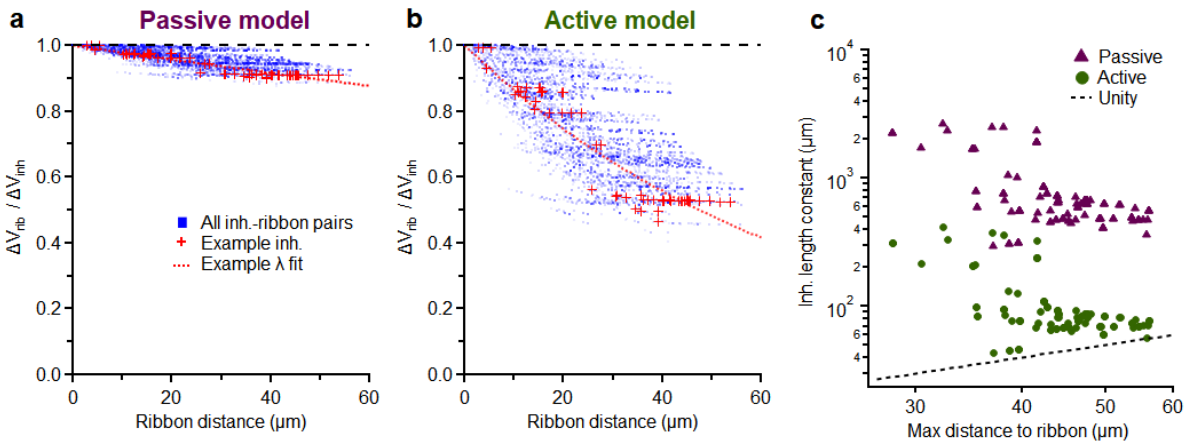

Supplementary Fig. 4.10 | Fitting length constants to inhibitory synapses.

(**a**,**b**) Cable model simulations in which a single inhibitory synapse is activated (same as **Fig. 4.6c**). The voltage change induced by inhibition is measured at the activated inhibitory synapse (ΔV_{inh}) and at each ribbon output synapse (ΔV_{rib}). The inhibitory voltage decay ($\Delta V_{rib}/\Delta V_{inh}$) is calculated for each ribbon output synapse and plotted against the path distance from the activated inhibitory synapse to that ribbon. Length constants are fit for each synapse according to the formula $\Delta V_{rib} / \Delta V_{inh} = e^{-x/\lambda}$, where x is the path distance and λ is the length constant. Length constants were calculated for both the passive (**a**) and active (**b**) versions of the type 6 BC model. (**c**) The length constant of each inhibitory synapse plotted against the distance to the furthest ribbon from that same inhibitory synapse.

References

1. Sanes, J. R. & Masland, R. H. The types of retinal ganglion cells: current status and implications for neuronal classification. *Annu. Rev. Neurosci.* **38**, 221–246 (2015).
2. Goetz, J. *et al.* Unified classification of mouse retinal ganglion cells using function, morphology, and gene expression. *bioRxiv* 2021.06.10.447922 (2022) doi:10.1101/2021.06.10.447922.
3. Rheaume, B. A. *et al.* Single cell transcriptome profiling of retinal ganglion cells identifies cellular subtypes. *Nat. Commun.* **9**, 2759 (2018).
4. Yuste, R. *et al.* A community-based transcriptomics classification and nomenclature of neocortical cell types. *Nat. Neurosci.* **23**, 1456–1468 (2020).
5. Dhande, O. S. *et al.* Molecular Fingerprinting of On–Off Direction-Selective Retinal Ganglion Cells Across Species and Relevance to Primate Visual Circuits. *J. Neurosci.* **39**, 78–95 (2019).
6. Wang, F., Li, E., De, L., Wu, Q. & Zhang, Y. OFF-transient alpha RGCs mediate looming triggered innate defensive response. *Curr. Biol.* **31**, 2263–2273.e3 (2021).
7. Parmhans, N. *et al.* Identification of retinal ganglion cell types and brain nuclei expressing the transcription factor Brn3c/Pou4f3 using a Cre recombinase knock-in allele. *J. Comp. Neurol.* **529**, 1926–1953 (2021).
8. D'Souza, S. P. *et al.* Retinal patterns and the cellular repertoire of neuropsin (Opn5) retinal ganglion cells. *J. Comp. Neurol.* **530**, 1247–1262 (2022).
9. Tran, N. M. *et al.* Single-Cell Profiles of Retinal Ganglion Cells Differing in Resilience to Injury Reveal Neuroprotective Genes. *Neuron* **104**, 1039–1055.e12 (2019).
10. Goetz, J. *et al.* Unified classification of mouse retinal ganglion cells using function, morphology, and gene expression. *Cell Rep.* **40**, 111040 (2022).
11. Bae, J. A. *et al.* Digital Museum of Retinal Ganglion Cells with Dense Anatomy and Physiology. *Cell* **173**, 1293–1306.e19 (2018).
12. Nath, A. & Schwartz, G. W. Cardinal Orientation Selectivity Is Represented by Two Distinct Ganglion Cell Types in Mouse Retina. *J. Neurosci.* **36**, 3208–3221 (2016).
13. Nath, A. & Schwartz, G. W. Electrical synapses convey orientation selectivity in the mouse retina. *Nat. Commun.* **8**, 2025 (2017).

14. Barlow, H. B., Hill, R. M. & Levick, W. R. RETINAL GANGLION CELLS RESPONDING SELECTIVELY TO DIRECTION AND SPEED OF IMAGE MOTION IN THE RABBIT. *J. Physiol.* **173**, 377–407 (1964).
15. Sabbah, S. *et al.* A retinal code for motion along the gravitational and body axes. *Nature* **546**, 492–497 (2017).
16. Swygart, D., Yu, W.-Q., Takeuchi, S., Wong, R. R. O. L. & Schwartz, G. W. A presynaptic source drives differing levels of surround suppression in two mouse retinal ganglion cell types. *bioRxiv* (2022) doi:10.1101/2022.11.12.516278.
17. Badea, T. C. & Nathans, J. Morphologies of mouse retinal ganglion cells expressing transcription factors Brn3a, Brn3b, and Brn3c: analysis of wild type and mutant cells using genetically-directed sparse labeling. *Vision Res.* **51**, 269–279 (2011).
18. Liu, W. *et al.* All Brn3 genes can promote retinal ganglion cell differentiation in the chick. *Development* **127**, 3237–3247 (2000).
19. Findlay, J. B. & Pappin, D. J. The opsin family of proteins. *Biochem. J* **238**, 625–642 (1986).
20. Schmidt, T. M. *et al.* Melanopsin-positive intrinsically photosensitive retinal ganglion cells: from form to function. *J. Neurosci.* **31**, 16094–16101 (2011).
21. Kojima, D. *et al.* UV-Sensitive Photoreceptor Protein OPN5 in Humans and Mice. *PLoS ONE* vol. 6 e26388 Preprint at https://doi.org/10.1371/journal.pone.0026388 (2011).
22. Cooler, S. & Schwartz, G. W. An offset ON–OFF receptive field is created by gap junctions between distinct types of retinal ganglion cells. *Nature Neuroscience* vol. 24 105–115 Preprint at https://doi.org/10.1038/s41593-020-00747-8 (2021).
23. Jacoby, J. & Schwartz, G. W. Three Small-Receptive-Field Ganglion Cells in the Mouse Retina Are Distinctly Tuned to Size, Speed, and Object Motion. *J. Neurosci.* **37**, 610–625 (2017).
24. Russo, R. *et al.* Retinal ganglion cell death in glaucoma: Exploring the role of neuroinflammation. *Eur. J. Pharmacol.* **787**, 134–142 (2016).
25. Kim, I.-J., Zhang, Y., Yamagata, M., Meister, M. & Sanes, J. R. Molecular identification of a retinal cell type that responds to upward motion. *Nature* **452**, 478–482 (2008).
26. Devries, S. H. & Baylor, D. A. Mosaic Arrangement of Ganglion Cell Receptive Fields in Rabbit

Retina. *Journal of Neurophysiology* vol. 78 2048–2060 Preprint at https://doi.org/10.1152/jn.1997.78.4.2048 (1997).

27. Bleckert, A., Schwartz, G. W., Turner, M. H., Rieke, F. & Wong, R. O. L. Visual space is represented by nonmatching topographies of distinct mouse retinal ganglion cell types. *Curr. Biol.* **24**, 310–315 (2014).
28. Mani, A. & Schwartz, G. W. Circuit Mechanisms of a Retinal Ganglion Cell with Stimulus-Dependent Response Latency and Activation Beyond Its Dendrites. *Curr. Biol.* **27**, 471–482 (2017).
29. Jacoby, J., Zhu, Y., DeVries, S. H. & Schwartz, G. W. An Amacrine Cell Circuit for Signaling Steady Illumination in the Retina. *Cell Rep.* **13**, 2663–2670 (2015).
30. Jacoby, J., Nath, A., Jessen, Z. F. & Schwartz, G. W. A Self-Regulating Gap Junction Network of Amacrine Cells Controls Nitric Oxide Release in the Retina. *Neuron* **100**, 1149–1162.e5 (2018).
31. Wienbar, S. & Schwartz, G. W. Differences in spike generation instead of synaptic inputs determine the feature selectivity of two retinal cell types. *Neuron* **110**, 2110–2123.e4 (2022).
32. Wurtz, R. H. Corollary Discharge Contributions to Perceptual Continuity Across Saccades. *Annu Rev Vis Sci* **4**, 215–237 (2018).
33. Franconeri, S. L. & Simons, D. J. Moving and looming stimuli capture attention. *Percept. Psychophys.* **65**, 999–1010 (2003).
34. Olveczky, B. P., Baccus, S. A. & Meister, M. Segregation of object and background motion in the retina. *Nature* **423**, 401–408 (2003).
35. Baccus, S. A., Olveczky, B. P., Manu, M. & Meister, M. A Retinal Circuit That Computes Object Motion. *Journal of Neuroscience* vol. 28 6807–6817 Preprint at https://doi.org/10.1523/jneurosci.4206-07.2008 (2008).
36. Zhang, Y., Kim, I.-J., Sanes, J. R. & Meister, M. The most numerous ganglion cell type of the mouse retina is a selective feature detector. *Proc. Natl. Acad. Sci. U. S. A.* **109**, E2391–8 (2012).
37. Kim, T. & Kerschensteiner, D. Inhibitory Control of Feature Selectivity in an Object Motion Sensitive Circuit of the Retina. *Cell Rep.* **19**, 1343–1350 (2017).
38. Vuong, H. E., Pérez de Sevilla Müller, L., Hardi, C. N., McMahon, D. G. & Brecha, N. C. Heterogeneous transgene expression in the retinas of the TH-RFP, TH-Cre, TH-BAC-Cre and

DAT-Cre mouse lines. *Neuroscience* **307**, 319–337 (2015).

39. Kim, T., Soto, F. & Kerschensteiner, D. An excitatory amacrine cell detects object motion and provides feature-selective input to ganglion cells in the mouse retina. *Elife* **4**, (2015).
40. Krishnaswamy, A., Yamagata, M., Duan, X., Hong, Y. K. & Sanes, J. R. Sidekick 2 directs formation of a retinal circuit that detects differential motion. *Nature* **524**, 466–470 (2015).
41. Lee, S. *et al.* An unconventional glutamatergic circuit in the retina formed by vGluT3 amacrine cells. *Neuron* **84**, 708–715 (2014).
42. Grimes, W. N., Seal, R. P., Oesch, N., Edwards, R. H. & Diamond, J. S. Genetic targeting and physiological features of VGLUT3 amacrine cells. *Visual Neuroscience* vol. 28 381–392 Preprint at https://doi.org/10.1017/s0952523811000290 (2011).
43. Kühn, N. K. & Gollisch, T. Joint Encoding of Object Motion and Motion Direction in the Salamander Retina. *J. Neurosci.* **36**, 12203–12216 (2016).
44. Cafaro, J., Zylberberg, J. & Field, G. D. Global Motion Processing by Populations of Direction-Selective Retinal Ganglion Cells. *J. Neurosci.* **40**, 5807–5819 (2020).
45. Bae, J. A. *et al.* Digital museum of retinal ganglion cells with dense anatomy and physiology. Preprint at https://doi.org/10.1101/182758.
46. Kerschensteiner, D. Feature Detection by Retinal Ganglion Cells. *Annu Rev Vis Sci* **8**, 135–169 (2022).
47. Masland, R. H. The neuronal organization of the retina. *Neuron* **76**, 266–280 (2012).
48. Baden, T. *et al.* The functional diversity of retinal ganglion cells in the mouse. *Nature* **529**, 345–350 (2016).
49. Briggman, K. L. *et al.* Wiring specificity in the direction-selectivity circuit of the retina. *Nature* **471**, 183–188 (2011).
50. Milner, E. S. & Do, M. T. H. A Population Representation of Absolute Light Intensity in the Mammalian Retina. *Cell* 1–12 (2017).
51. Schwartz, G. W. Surround suppression. in *Retinal Computation* (Academic Press, 2021).
52. Kuffler, S. W. Discharge patterns and functional organization of mammalian retina. *J. Neurophysiol.* **16**, 37–68 (1953).

53. Johnson, K. P., Zhao, L. & Kerschensteiner, D. A Pixel-Encoder Retinal Ganglion Cell with Spatially Offset Excitatory and Inhibitory Receptive Fields. *Cell Rep.* **22**, 1462–1472 (2018).

54. VAN Wyk, M., Van Wyk, M., Wässle, H. & Rowland Taylor, W. Receptive field properties of ON- and OFF-ganglion cells in the mouse retina. *Visual Neuroscience* vol. 26 297–308 Preprint at https://doi.org/10.1017/s0952523809990137 (2009).

55. Johnson, K. P. *et al.* Cell-type-specific binocular vision guides predation in mice. *Neuron* **109**, 1527–1539.e4 (2021).

56. Sonoda, T., Okabe, Y. & Schmidt, T. M. Overlapping morphological and functional properties between M4 and M5 intrinsically photosensitive retinal ganglion cells. *J. Comp. Neurol.* **528**, 1028–1040 (2020).

57. Bleckert, A., Schwartz, G. W., Turner, M. H., Rieke, F. & Wong, R. O. L. Visual Space Is Represented by Nonmatching Topographies of Distinct Mouse Retinal Ganglion Cell Types. *Curr. Biol.* **24**, 310–315 (2014).

58. Estevez, M. E. *et al.* Form and function of the M4 cell, an intrinsically photosensitive retinal ganglion cell type contributing to geniculocortical vision. *J. Neurosci.* **32**, 13608–13620 (2012).

59. Dunn, F. A. & Rieke, F. Single-photon absorptions evoke synaptic depression in the retina to extend the operational range of rod vision. *Neuron* **57**, 894–904 (2008).

60. Franke, K. *et al.* Inhibition decorrelates visual feature representations in the inner retina. *Nature* **542**, 439–444 (2017).

61. Borghuis, B. G., Marvin, J. S., Looger, L. L. & Demb, J. B. Two-photon imaging of nonlinear glutamate release dynamics at bipolar cell synapses in the mouse retina. *J. Neurosci.* **33**, 10972–10985 (2013).

62. Sabbah, S. *et al.* Intrinsically photosensitive retinal ganglion cells evade temporal filtering to encode environmental light intensity. *bioRxiv* 2022.04.09.487733 (2022) doi:10.1101/2022.04.09.487733.

63. Tien, N.-W., Soto, F. & Kerschensteiner, D. Homeostatic Plasticity Shapes Cell-Type-Specific Wiring in the Retina. *Neuron* **94**, 656–665.e4 (2017).

64. Shekhar, K. *et al.* Comprehensive Classification of Retinal Bipolar Neurons by Single-Cell Transcriptomics. *Cell* **166**, 1308–1323.e30 (2016).

65. Bleckert, A. *et al.* Spatial Relationships between GABAergic and Glutamatergic Synapses on the Dendrites of Distinct Types of Mouse Retinal Ganglion Cells across Development. *PLoS ONE* vol. 8 e69612 Preprint at https://doi.org/10.1371/journal.pone.0069612 (2013).

66. Chavez, A. E., Grimes, W. N. & Diamond, J. S. Mechanisms Underlying Lateral GABAergic Feedback onto Rod Bipolar Cells in Rat Retina. *Journal of Neuroscience* **30**, 2330–2339 (2010).

67. Shields, C. R. & Lukasiewicz, P. D. Spike-dependent GABA inputs to bipolar cell axon terminals contribute to lateral inhibition of retinal ganglion cells. *J. Neurophysiol.* **89**, 2449–2458 (2003).

68. Koulen, P., Brandstätter, J. H., Enz, R., Bormann, J. & Wässle, H. Synaptic clustering of GABA C receptor ρ-subunits in the rat retina. *Eur. J. Neurosci.* **10**, 115–127 (1998).

69. Carnevale, N. T. & Hines, M. L. *The NEURON Book*. (Cambridge University Press, 2006).

70. Oltedal, L., Veruki, M. L. & Hartveit, E. Passive membrane properties and electrotonic signal processing in retinal rod bipolar cells. *J. Physiol.* **587**, 829–849 (2009).

71. Matsumoto, A. *et al.* Direction selectivity in retinal bipolar cell axon terminals. *Neuron* vol. 109 3895–3896 Preprint at https://doi.org/10.1016/j.neuron.2021.11.004 (2021).

72. Oltedal, L., Mørkve, S. H., Veruki, M. L. & Hartveit, E. Patch-clamp investigations and compartmental modeling of rod bipolar axon terminals in an in vitro thin-slice preparation of the mammalian retina. *J. Neurophysiol.* **97**, 1171–1187 (2007).

73. Puthussery, T., Venkataramani, S., Gayet-Primo, J., Smith, R. G. & Taylor, W. R. NaV1.1 Channels in Axon Initial Segments of Bipolar Cells Augment Input to Magnocellular Visual Pathways in the Primate Retina. *Journal of Neuroscience* vol. 33 16045–16059 Preprint at https://doi.org/10.1523/jneurosci.1249-13.2013 (2013).

74. Werginz, P., Benav, H., Zrenner, E. & Rattay, F. Modeling the response of ON and OFF retinal bipolar cells during electric stimulation. *Vision Res.* **111**, 170–181 (2015).

75. Rattay, F., Bassereh, H. & Stiennon, I. Compartment models for the electrical stimulation of retinal bipolar cells. *PLOS ONE* vol. 13 e0209123 Preprint at https://doi.org/10.1371/journal.pone.0209123 (2018).

76. Paknahad, J. *et al.* Modeling ON Cone Bipolar Cells for Electrical Stimulation. *2021 43rd Annual International Conference of the IEEE Engineering in Medicine & Biology Society (EMBC)* Preprint at

https://doi.org/10.1109/embc46164.2021.9629884 (2021).

77. Hu, C., Bi, A. & Pan, Z.-H. Differential expression of three T-type calcium channels in retinal bipolar cells in rats. *Visual Neuroscience* vol. 26 177–187 Preprint at https://doi.org/10.1017/s0952523809090026 (2009).
78. Berntson, A., Rowland Taylor, W. & Morgans, C. W. Molecular identity, synaptic localization, and physiology of calcium channels in retinal bipolar cells. *Journal of Neuroscience Research* vol. 71 146–151 Preprint at https://doi.org/10.1002/jnr.10459 (2003).
79. Hu, H.-J. & Pan, Z.-H. Differential expression of K+ currents in mammalian retinal bipolar cells. *Vis. Neurosci.* **19**, 163–173 (2002).
80. Müller, F. *et al.* HCN channels are expressed differentially in retinal bipolar cells and concentrated at synaptic terminals. *Eur. J. Neurosci.* **17**, 2084–2096 (2003).
81. Ivanova, E. & Müller, F. Retinal bipolar cell types differ in their inventory of ion channels. *Vis. Neurosci.* **23**, 143–154 (2006).
82. Grimes, W. N., Schwartz, G. W. & Rieke, F. The Synaptic and Circuit Mechanisms Underlying a Change in Spatial Encoding in the Retina. *Neuron* vol. 82 460–473 Preprint at https://doi.org/10.1016/j.neuron.2014.02.037 (2014).
83. Neher, E. & Sakaba, T. Multiple roles of calcium ions in the regulation of neurotransmitter release. *Neuron* **59**, 861–872 (2008).
84. Linden, D. J. A life in science, ending soon. *Neuron* **110**, 2899–2901 (2022).
85. Krnjevic, K. & Miledi, R. Presynaptic failure of neuromuscular propagation in rats. *J. Physiol.* **149**, 1–22 (1959).
86. Krnjevic, K. & Miledi, R. Adrenaline and failure of neuromuscular transmission. *Nature* **180**, 814–815 (1957).
87. Krnjevic, K. & Miledi, R. Failure of neuromuscular propagation in rats. *J. Physiol.* **140**, 440–461 (1958).
88. Grossman, Y., Parnas, I. & Spira, M. E. Mechanisms involved in differential conduction of potentials at high frequency in a branching axon. *J. Physiol.* **295**, 307–322 (1979).
89. Grossman, Y., Parnas, I. & Spira, M. E. Differential conduction block in branches of a bifurcating

axon. *J. Physiol.* **295**, 283–305 (1979).

90. Zhou, L. & Chiu, S. Y. Computer model for action potential propagation through branch point in myelinated nerves. *J. Neurophysiol.* **85**, 197–210 (2001).
91. Heitler & Goodman. Multiple sites of spike initiation in a bifurcating locust neurone. *J. Exp. Biol.*
92. Baccus, S. A., Burrell, B. D., Sahley, C. L. & Muller, K. J. Action potential reflection and failure at axon branch points cause stepwise changes in EPSPs in a neuron essential for learning. *J. Neurophysiol.* **83**, 1693–1700 (2000).
93. Cataldo, E. *et al.* Computational model of touch sensory cells (T Cells) of the leech: role of the afterhyperpolarization (AHP) in activity-dependent conduction failure. *J. Comput. Neurosci.* **18**, 5–24 (2005).
94. Gu, X. N. Effect of conduction block at axon bifurcations on synaptic transmission to different postsynaptic neurones in the leech. *J. Physiol.* **441**, 755–778 (1991).
95. Macagno, E. R., Muller, K. J. & Pitman, R. M. Conduction block silences parts of a chemical synapse in the leech central nervous system. *J. Physiol.* **387**, 649–664 (1987).
96. Scuri, R., Lombardo, P., Cataldo, E., Ristori, C. & Brunelli, M. Inhibition of Na+/K+ ATPase potentiates synaptic transmission in tactile sensory neurons of the leech. *Eur. J. Neurosci.* **25**, 159–167 (2007).
97. Van Essen, D. C. The contribution of membrane hyperpolarization to adaptation and conduction block in sensory neurones of the leech. *J. Physiol.* **230**, 509–534 (1973).
98. Baden, T. & Hedwig, B. Primary afferent depolarization and frequency processing in auditory afferents. *J. Neurosci.* **30**, 14862–14869 (2010).
99. Debanne, D., Guérineau, N. C., Gähwiler, B. H. & Thompson, S. M. Action-potential propagation gated by an axonal I(A)-like K+ conductance in hippocampus. *Nature* **389**, 286–289 (1997).
100. Kopysova, I. L. & Debanne, D. Critical role of axonal A-type K+ channels and axonal geometry in the gating of action potential propagation along CA3 pyramidal cell axons: a simulation study. *J. Neurosci.* **18**, 7436–7451 (1998).
101. Debanne, D., Kopysova, I. L., Bras, H. & Ferrand, N. Gating of action potential propagation by an axonal A-like potassium conductance in the hippocampus: a new type of non-synaptic plasticity. *J.*

Physiol. Paris **93**, 285–296 (1999).

102. Westberg, K. G., Kolta, A., Clavelou, P., Sandström, G. & Lund, J. P. Evidence for functional compartmentalization of trigeminal muscle spindle afferents during fictive mastication in the rabbit. *Eur. J. Neurosci.* **12**, 1145–1154 (2000).
103. Verdier, D., Lund, J. P. & Kolta, A. GABAergic control of action potential propagation along axonal branches of mammalian sensory neurons. *J. Neurosci.* **23**, 2002–2007 (2003).
104. Wall, P. D. Do nerve impulses penetrate terminal arborizations? A pre-presynaptic control mechanism. *Trends Neurosci.* **18**, 99–103 (1995).
105. Grimes, W. N., Zhang, J., Graydon, C. W., Kachar, B. & Diamond, J. S. Retinal parallel processors: more than 100 independent microcircuits operate within a single interneuron. *Neuron* **65**, 873–885 (2010).
106. Hsiang, J.-C., Johnson, K. P., Madisen, L., Zeng, H. & Kerschensteiner, D. Local processing in neurites of VGluT3-expressing amacrine cells differentially organizes visual information. *Elife* **6**, (2017).
107. Pottackal, J., Singer, J. H. & Demb, J. B. Computational and Molecular Properties of Starburst Amacrine Cell Synapses Differ With Postsynaptic Cell Type. *Front. Cell. Neurosci.* **15**, 660773 (2021).
108. Baden, T. *et al.* A Synaptic Mechanism for Temporal Filtering of Visual Signals. *PLoS Biology* vol. 12 e1001972 Preprint at https://doi.org/10.1371/journal.pbio.1001972 (2014).
109. Jarsky, T., Tian, M. & Singer, J. H. Nanodomain control of exocytosis is responsible for the signaling capability of a retinal ribbon synapse. *J. Neurosci.* **30**, 11885–11895 (2010).
110. Yan, W. *et al.* Mouse retinal cell atlas: molecular identification of over sixty amacrine cell types. *Journal of Neuroscience* **40**, 5177–5195 (2020).
111. Hellmer, C. B. *et al.* Cholinergic feedback to bipolar cells contributes to motion detection in the mouse retina. *Cell Rep.* **37**, 110106 (2021).
112. Farshi, P., Fyk-Kolodziej, B., Krolewski, D. M., Walker, P. D. & Ichinose, T. Dopamine D1 receptor expression is bipolar cell type-specific in the mouse retina. *J. Comp. Neurol.* **524**, 2059–2079 (2016).
113. Veruki, M. L. & Wässle, H. Immunohistochemical Localization of Dopamine D Receptors in Rat

Retina. *Eur. J. Neurosci.* **8**, 2286–2297 (1996).

114. Lezcano, N. & Bergson, C. D1/D5 dopamine receptors stimulate intracellular calcium release in primary cultures of neocortical and hippocampal neurons. *J. Neurophysiol.* **87**, 2167–2175 (2002).
115. Tooker, R. E. *et al.* Nitric oxide mediates activity-dependent plasticity of retinal bipolar cell output via S-nitrosylation. *J. Neurosci.* **33**, 19176–19193 (2013).
116. Hedden, W. L., Jr & Dowling, J. E. The interplexiform cell system. II. Effects of dopamine on goldfish retinal neurones. *Proc. R. Soc. Lond. B Biol. Sci.* **201**, 27–55 (1978).
117. Middleton, T. P., Huang, J. Y. & Protti, D. A. Cannabinoids Modulate Light Signaling in ON-Sustained Retinal Ganglion Cells of the Mouse. *Front. Neural Circuits* **13**, 37 (2019).
118. Poleg-Polsky, A., Ding, H. & Diamond, J. S. Functional Compartmentalization within Starburst Amacrine Cell Dendrites in the Retina. *Cell Rep.* **22**, 2898–2908 (2018).
119. Vlasits, A. L. *et al.* A Role for Synaptic Input Distribution in a Dendritic Computation of Motion Direction in the Retina. *Neuron* **89**, 1317–1330 (2016).
120. Jain, V. *et al.* The functional organization of excitation and inhibition in the dendrites of mouse direction-selective ganglion cells. *Elife* **9**, (2020).
121. Murphy-Baum, B. L. & Awatramani, G. B. Parallel processing in active dendrites during periods of intense spiking activity. *Cell Rep.* **38**, 110412 (2022).
122. Ran, Y. *et al.* Type-specific dendritic integration in mouse retinal ganglion cells. *Nat. Commun.* **11**, 2101 (2020).
123. Euler, T., Franke, K. & Baden, T. Studying a Light Sensor with Light: Multiphoton Imaging in the Retina. in *Multiphoton Microscopy* (ed. Hartveit, E.) 225–250 (Springer New York, 2019).
124. Asari, H. & Meister, M. Divergence of visual channels in the inner retina. *Nat. Neurosci.* **15**, 1581–1589 (2012).
125. Taylor, W. R. & Smith, R. G. Trigger features and excitation in the retina. *Curr. Opin. Neurobiol.* **21**, 672–678 (2011).
126. Rogerson, L. E., Zhao, Z., Franke, K., Euler, T. & Berens, P. Bayesian hypothesis testing and experimental design for two-photon imaging data. *PLoS Comput. Biol.* **15**, e1007205 (2019).
127. Ding, H., Smith, R. G., Poleg-Polsky, A., Diamond, J. S. & Briggman, K. L. Species-specific wiring for

direction selectivity in the mammalian retina. *Nature* **535**, 105–110 (2016).

128. Kim, J. S. *et al.* Space–time wiring specificity supports direction selectivity in the retina. *Nature* **509**, 331–336 (2014).
129. Desai, N. S., Gray, R. & Johnston, D. A Dynamic Clamp on Every Rig. *eNeuro* **4**, (2017).
130. Stabio, M. E. *et al.* The M5 Cell: A Color-Opponent Intrinsically Photosensitive Retinal Ganglion Cell. *Neuron* **97**, 251 (2018).
131. Arshadi, C., Günther, U., Eddison, M., Harrington, K. I. S. & Ferreira, T. A. SNT: a unifying toolbox for quantification of neuronal anatomy. *Nat. Methods* **18**, 374–377 (2021).
132. Sümbül, U. *et al.* A genetic and computational approach to structurally classify neuronal types. *Nat. Commun.* **5**, 3512 (2014).
133. Bishop, D. *et al.* Near-infrared branding efficiently correlates light and electron microscopy. *Nat. Methods* **8**, 568–570 (2011).
134. Della Santina, L. *et al.* Glutamatergic Monopolar Interneurons Provide a Novel Pathway of Excitation in the Mouse Retina. *Curr. Biol.* **26**, 2070–2077 (2016).
135. Cardona, A. *et al.* TrakEM2 software for neural circuit reconstruction. *PLoS One* **7**, e38011 (2012).
136. Behrens, C., Schubert, T., Haverkamp, S., Euler, T. & Berens, P. Connectivity map of bipolar cells and photoreceptors in the mouse retina. *Elife* **5**, (2016).
137. Helmstaedter, M. *et al.* Connectomic reconstruction of the inner plexiform layer in the mouse retina. *Nature* **500**, 168–174 (2013).
138. Tsukamoto, Y. & Omi, N. Classification of Mouse Retinal Bipolar Cells: Type-Specific Connectivity with Special Reference to Rod-Driven AII Amacrine Pathways. *Front. Neuroanat.* **11**, 92 (2017).
139. Jakobs, T. C., Koizumi, A. & Masland, R. H. The spatial distribution of glutamatergic inputs to dendrites of retinal ganglion cells. *J. Comp. Neurol.* **510**, 221–236 (2008).
140. Schwartz, G. W. *et al.* The spatial structure of a nonlinear receptive field. *Nature Neuroscience* vol. 15 1572–1580 Preprint at https://doi.org/10.1038/nn.3225 (2012).
141. Rodieck, R. W. Quantitative analysis of cat retinal ganglion cell response to visual stimuli. *Vision Res.* **5**, 583–601 (1965).
142. Kuo, S. P., Schwartz, G. W. & Rieke, F. Nonlinear Spatiotemporal Integration by Electrical and

Chemical Synapses in the Retina. *Neuron* vol. 90 320–332 Preprint at https://doi.org/10.1016/j.neuron.2016.03.012 (2016).

143. Narahashi, T., Moore, J. W. & Scott, W. R. Tetrodotoxin Blockage of Sodium Conductance Increase in Lobster Giant Axons. *Journal of General Physiology* vol. 47 965–974 Preprint at https://doi.org/10.1085/jgp.47.5.965 (1964).
144. Ueno, S., Bracamontes, J., Zorumski, C., Weiss, D. S. & Steinbach, J. H. Bicuculline and Gabazine Are Allosteric Inhibitors of Channel Opening of the $GABA_A$Receptor. *The Journal of Neuroscience* vol. 17 625–634 Preprint at https://doi.org/10.1523/jneurosci.17-02-00625.1997 (1997).
145. Li, S., Zhang, Y., Liu, H., Yan, Y. & Li, Y. Identification and expression of $GABA_C$receptor in rat testis and spermatozoa. *Acta Biochimica et Biophysica Sinica* vol. 40 761–767 Preprint at https://doi.org/10.1111/j.1745-7270.2008.00453.x (2008).
146. Kerr, D. I. B. *et al.* GABAB receptor antagonism by resolved (R)-saclofen in the guinea-pig ileum. *European Journal of Pharmacology* vol. 308 R1–R2 Preprint at https://doi.org/10.1016/0014-2999(96)00334-2 (1996).
147. O'connor, V. INTERACTIONS OF GLYCINE AND STRYCHNINE WITH THEIR RECEPTOR RECOGNITION SITES IN MOUSE SPINAL CORD. *Neurochemistry International* vol. 29 423–434 Preprint at https://doi.org/10.1016/0197-0186(95)00160-3 (1996).
148. Weber, M. *et al.* 6-Hydroxykynurenic acid and kynurenic acid differently antagonise AMPA and NMDA receptors in hippocampal neurones. *J. Neurochem.* **77**, 1108–1115 (2001).
149. Kovács, I. *et al.* Cyclothiazide binding to functionally active AMPA receptor reveals genuine allosteric interaction with agonist binding sites. *Neurochem. Int.* **44**, 271–280 (2004).
150. Bushell, T. J. *et al.* Antagonism of the synaptic depressant actions of L-AP4 in the lateral perforant path by MAP4. *Neuropharmacology* **34**, 239–241 (1995).
151. Honoré, T. *et al.* Quinoxalinediones: potent competitive non-NMDA glutamate receptor antagonists. *Science* **241**, 701–703 (1988).
152. Davies, J. & Watkins, J. C. Actions of D and L forms of 2-amino-5-phosphonovalerate and 2-amino-4-phosphonobutyrate in the cat spinal cord. *Brain Res.* **235**, 378–386 (1982).
153. Nawy, S. Regulation of the on bipolar cell mGluR6 pathway by Ca2+. *Journal of Neuroscience*

(2000).

154. Ichinose, T., Fyk-Kolodziej, B. & Cohn, J. Roles of ON cone bipolar cell subtypes in temporal coding in the mouse retina. *J. Neurosci.* **34**, 8761–8771 (2014).
155. Billups, D. & Attwell, D. Control of intracellular chloride concentration and GABA response polarity in rat retinal ON bipolar cells. *J. Physiol.* (2002).
156. Eggers, E. D. & Lukasiewicz, P. D. Multiple pathways of inhibition shape bipolar cell responses in the retina. *Vis. Neurosci.* **28**, 95–108 (2011).
157. ModelDB: Firing neocortical layer V pyramidal neuron (Reetz et al. 2014; Stadler et al. 2014). https://senselab.med.yale.edu/ModelDB/showmodel?model=168148&file=/stadler2014_layerV/HCN2r.mod.
158. Byczkowicz, N. *et al.* HCN channel-mediated neuromodulation can control action potential velocity and fidelity in central axons. *Elife* **8**, (2019).
159. Moosmang, S. *et al.* Cellular expression and functional characterization of four hyperpolarization-activated pacemaker channels in cardiac and neuronal tissues. *Eur. J. Biochem.* **268**, 1646–1652 (2001).
160. Kv1.2. https://channelpedia.epfl.ch/wiki/ionchannels/2.
161. Sprunger, L. K., Stewig, N. J. & O'Grady, S. M. Effects of charybdotoxin on K+ channel (KV1.2) deactivation and inactivation kinetics. *Eur. J. Pharmacol.* **314**, 357–364 (1996).
162. ModelDB: Simulated light response in rod photoreceptors (Liu and Kourennyi 2004). https://senselab.med.yale.edu/ModelDB/showmodel?model=64228&file=/Liu-Kourennyi_2004/Ca.mod.